

EXPERIMENTAL STUDY OF ELECTRONS FROM HEAVY FLAVOR
HADRONS DECAYS IN AU+AU COLLISIONS AT 200, 62.4 AND 39 GEV IN
THE STAR EXPERIMENT AT RHIC

A Dissertation

Submitted to the Faculty

of

Purdue University

by

Mustafa Mustafa

In Partial Fulfillment of the

Requirements for the Degree

of

Doctor of Philosophy

August 2013

Purdue University

West Lafayette, Indiana

To my father.

ACKNOWLEDGMENTS

In every journey towards a goal there are those who guide and support you along the way. I was fortunate to have many of those people during my journey towards my doctorate. For those people I will be eternally indebted. Therefore, the brief mention that I make of those mentors and supporters will never commensurate the debt that I owe to them.

I would like to thank my dissertation advisor Prof. Wei Xie for believing in me and for introducing me to this field. Prof. Xie's guidance and close supervision of my day-to-day technical work was vital for the timely completion of my dissertation work. I would also like to express my sincere appreciation to Dr. Daniel Kikoła for the countless hours he spent in long discussions with me. Dr. Kikoła's guidance and support during the difficult times was essential, this work would not have been possible without it. I am truly indebted to Prof. Denes Molnar to whom I owe my knowledge and curiosity about the underlying theory and interpretation of heavy-ion collisions. Our countless exchanges have made me a better physicist.

It is not possible to overstate the significant role STAR collaboration has played in forming me as a scientist. STAR collaboration has provided me with the environment and intellectual exchanges that matured my knowledge and appreciation of my field. In particular, I would like to thank Dr. Jerome Lauret and Dr. Xin Dong for their guidance in making me an effective member of this collaboration.

TABLE OF CONTENTS

	Page
LIST OF TABLES	vi
LIST OF FIGURES	vii
ABSTRACT	xv
1 INTRODUCTION	1
1.1 Quantum Chromodynamics	1
1.1.1 Quark Model	1
1.1.2 QCD Lagrangian	2
1.1.3 Asymptotic Freedom	3
1.1.4 Non-perturbative QCD	4
1.1.5 Perturbative QCD	6
1.2 Quark-Gluon Plasma	8
1.2.1 Phase diagram	8
1.2.2 Lattice QCD	10
1.3 Heavy-Ion collisions	11
1.3.1 Heavy-Ion collision stages	12
1.3.2 Particle production	14
1.3.3 Centrality	14
1.3.4 Signals of QGP I - Energy density	15
1.3.5 Signals of QGP II - Statistical hadronization	16
1.3.6 Signals of QGP III - Collective motion	17
1.3.7 Signals of QGP IV - Jet quenching	21
1.4 Open heavy flavor measurements	25
1.4.1 Heavy quarks as probes of sQGP	25
1.4.2 Open heavy flavor reconstruction	28
1.4.3 Experimental observables - What have we learned thus far?	29
2 EXPERIMENTAL SETUP	33
2.1 Relativistic Heavy Ion Collider	33
2.2 STAR detector	35
2.2.1 Time Projection Chamber	36
2.2.2 Barrel Electromagnetic Calorimeter	37
2.2.3 Time of Flight detector	38
3 NON-PHOTONIC ELECTRON ANALYSIS	41
3.1 Analysis Principle	41

	Page
3.2 Datasets and quality assurance	45
3.3 Trigger combination	49
3.4 Electron identification and efficiencies	53
3.4.1 Electron identification cuts	53
3.4.2 Electron identification cuts efficiencies	70
3.5 Detector acceptance and efficiencies corrections	76
3.5.1 Single electrons reconstruction efficiency	76
3.5.2 Photonic electrons reconstruction efficiency	78
3.6 Electron purity	82
3.7 Photonic electron cocktail	84
3.8 Spectra and systematic uncertainties	89
3.9 J/ψ contribution to non-photonic electrons	89
4 RESULTS AND DISCUSSION	93
4.1 Non-photonic electron spectra and azimuthal anisotropy at $\sqrt{s_{NN}} = \mathbf{200}$ GeV	93
4.1.1 Non-photonic electron spectra and nuclear modification factor	93
4.1.2 Non-photonic electron azimuthal anisotropy	97
4.1.3 Azimuthal anisotropy and nuclear modification factor compar- ison to models	98
4.2 Non-photonic electron spectra and azimuthal anisotropy at $\sqrt{s_{NN}} = \mathbf{39}$ and $\mathbf{62.4}$ GeV	102
4.2.1 Non-photonic electron spectra	102
4.3 Non-photonic electron azimuthal anisotropy	105
5 SUMMARY	107
LIST OF REFERENCES	109
VITA	113

LIST OF TABLES

Table	Page
3.1 Datasets and event selection cuts for $Au+Au$ at $\sqrt{s_{NN}} = 39$ and 62.4 GeV.	46
3.2 N_{bin} , N_{part} and impact parameter for different centralities in $Au+Au$ at $\sqrt{s_{NN}} = 62.4$ GeV from Monte-Carlo Glauber simulations.	50
3.3 Track quality cuts	54
3.4 Pairs cuts	56
3.5 Electrons Identification cuts	58
3.6 Cuts used for TOF-matching efficiency.	74

LIST OF FIGURES

Figure	Page
1.1 First order Feynman diagrams showing a) screening and b) anti-screening.	3
1.2 (Color online) A compilation of the world measurements of the running coupling constant α_s as a function of energy scale Q demonstrating asymptotic freedom, figure from [11].	5
1.3 (Color online) A compilation of experimental measurements of inclusive jet production in different collision systems and at different energies compared to NLO pQCD as a function of jet transverse momentum (p_T). Figure extracted from [11].	8
1.4 Conjectured QCD phase diagram. Figure extracted from [18]. Only QGP phase is discussed here, for a wider overview of the QCD phase diagram see [19].	9
1.5 (Left) Energy density and EoS from lattice QCD calculations showing a transition to partonic degrees of freedom at $T_c \approx 175$ MeV, the arrow indicates the relativistic gas limit. (Right) Lattice QCD entropy density divided by the relativistic gas value. Figures extracted from [20]	10
1.6 A schematic diagram showing the conventional stages of heavy-ion collisions. Figure extracted from [18].	13
1.7 (Color online) Centrality selection from charged particle multiplicity distribution in $Au+Au$ at $\sqrt{s_{NN}} = 130$ GeV. Plot from [29].	15
1.8 (Left) Ratios of p_T -integrated yields of hadrons in central $Au+Au$ collisions at $\sqrt{s_{NN}} = 200$ GeV from STAR experiment. Thermal model fit parameters yield $T = 163 \pm 4$ MeV, $\mu_B = 24 \pm 4$ MeV and $\gamma_s = 0.99 \pm 0.07$. Inset shows the evolution of the strangeness suppression factor from peripheral to central collision events. Plot extracted from [1]. (Right) Thermal model fits to central $Pb+Pb$ data from ALICE, fit parameters are indicated in the figure (protons and anti-protons are excluded from the fits see reference). Plot extracted from [33].	17
1.9 (Left) Near-elliptic shape collisions region in non-central collisions. Figure from [18]. (Right) Interaction maps space anisotropy into momentum anisotropy. Figure from [39].	20

Figure	Page
1.10 Charged hadrons v_2 vs. p_T for 10–20% centrality class in $Au+Au$ collisions at $\sqrt{s_{NN}} = 200$ GeV. Also shown are simulations from 3 + 1D viscous hydro (MUSIC), and MUSIC coupled to a kinetic theory model (UrQMD). Figure extracted from [35].	21
1.11 (Left) Results for p_T -dependent charged hadrons R_{dAu} at $\sqrt{s_{NN}} = 200$ GeV in centrality bins from PHOBOS [41]. (Right) MinBias R_{dAu} and central R_{AA} for charged hadrons in $Au+Au$ at $\sqrt{s_{NN}} = 200$ GeV from STAR [42].	22
1.12 (Color online) (Left) Charged hadrons and neutral pions R_{AA} vs. p_T from several measurements at SPS, RHIC and the LHC (see legend for energies) compared to several energy loss models. Plot extracted from [44]. (Right) Charged hadrons R_{cp} vs. p_T from RHIC Beam-Energy-Scan program the suppression is clearly lessening as energy decreases indicating a possible turn-off of the energy loss at lower energies [45].	23
1.13 High- p_T di-hadron azimuthal correlations in $p+p$, $d+Au$, and central $Au+Au$ collisions from STAR experiment [42].	25
1.14 (Left) Leading Order diagrams of heavy quark production cross-section. (Right) Charm differential cross-section measured by STAR [47] clearly demonstrates the power-law high p_T tail. Measurement is consistent with FONLL upper bound [46].	26
1.15 (Left) Charm total cross-section at mid-rapidity in different collision systems normalized to one binary collision. (Right) Contribution of mass generated by electroweak symmetry breaking (current quark mass) is shown in blue, additional contribution of mass generated by spontaneous chiral symmetry breaking in QCD (constituent quark mass) is shown in yellow, figure from [34].	27
1.16 Previous results (Left) PHENIX [50]. (Right) STAR [51]	29
2.1 RHIC accelerator complex. Interaction points shown at 2,4,6, 8 and 10 o'clock. BRAHMS and PHOBOS have been decommissioned. PHENIX and STAR are still operating	34
2.2 3D view of the STAR detector.	35
2.3 A reconstructed $Au+Au$ high multiplicity event demonstrating STAR high multiplicity operation environment. Tiles in green represent the energy deposited in the BEMC (see text below).	36
2.4 Cross-sectional view of the Time Projection Chamber (TPC).	37

Figure	Page
2.5 STAR Barrel-Electromagnetic-Calorimeter (BEMC) sitting inside the magnet. The BEMC towers are annotated and their projectivity to the interaction diamond is illustrated by the tilting of the towers. Shown in green are energy deposited by tracks coming from the vertex.	38
2.6 (Left) Side view of BEMC module showing the 20 lead layers and 21 layers of scintillators. Also shown are the two layers of Shower Maximum Detector (BSMD) sitting at a depth of $\sim 5X_0$ from the front face at $\eta = 0$. (Right) A schematic illustration of an electromagnetic shower at the BSMD wire layers which provide a two-dimensional image of the shower. Figures taken from [63].	39
2.7 (Color online) Pure electrons sample at very low-momentum can be extracted by applying dE/dx and TOF cuts.	39
2.8 (Color online) Particles dE/dx in TPC vs. momentum from $Au+Au$ events, Bichsel dE/dx functions [66] of the different particles species are also shown. (Left) dE/dx without TOF hadron rejection cut. (Right) Highly electrons-enriched sample after applying TOF hadron rejection cuts.	40
3.1 Topology of the photonic electrons origin from $Au+Au$ $\sqrt{s_{NN}} = 62.4$ GeV real data.	42
3.2 (Color online) Upper panels are electrons pairs invariant mass distributions for electrons at $2.5 \text{ GeV}/c < p_T < 3.0 \text{ GeV}/c$ (a) and at $8.0 \text{ GeV}/c < p_T < 10.0 \text{ GeV}/c$ (b). Solid and dashed lines are unlike-sign and like-sign pairs, respectively. Closed circles are the difference of unlike and like. Lower panels show simulated invariant mass distributions with electrons at $2.5 \text{ GeV}/c < p_T < 3.0 \text{ GeV}/c$ (c) and at $8.0 \text{ GeV}/c < p_T < 10.0 \text{ GeV}/c$ (d). Solid and dashed lines are results from γ conversions and π^0 Dalitz decay.	44
3.3 (Color online) Event vertex distributions in $Au+Au$ at $\sqrt{s_{NN}} = 62.4$ GeV. (Top left) Distribution of events vertex Z-coordinate with respect to STAR center, this vertex is from the TPC tracking and vertex finding algorithms. (Top right) Z-vertex from tracking (V_z) versus Z-vertex from VPD clearly peaking at the center of the TPC, distribution is used to place a sensible $ V_z - V_{vpz} $ cut for events selection. (Bottom) Distribution of events vertices in the xy-plane.	47
3.4 (Color online) $\sqrt{s_{NN}} = 62.4$ GeV data. (Left) Number of events which pass the vertex cuts divided by the total number of collected events in one run versus the runID, approximately $3\text{-}\sigma$ cut is shown in red, blue points pass the cut red points are rejected runs. (Right) projection of the left plot on the y-axis.	48

Figure	Page
3.5 (Color online) $\sqrt{s_{NN}} = 62.4$ GeV data. Left panel is average number of tracks (see definition of refMult) per event versus runID. Left panel is the y-axis projection of the left plot.	48
3.6 (Color online) $\sqrt{s_{NN}} = 62.4$ GeV data. Left panel is average number of electrons identified using TOF (see text for details) per event versus runID. Left panel is the y-axis projection of the left plot.	49
3.7 (Color online) $\sqrt{s_{NN}} = 62.4$ GeV data. Left panel is average number of electrons identified using BEMC (see text for details) per event versus runID. Left panel is the y-axis projection of the left plot.	49
3.8 (Color online) $\sqrt{s_{NN}} = 62.4$ GeV data. Hot towers during this run. Plotted is the average number of electrons in BTOW towers. Hot towers are shown in red.	50
3.9 Venn diagram of triggered data in different streams.	51
3.10 An example of the trigger combination algorithm with one HT trigger.	52
3.11 Ratios of trigger combined inc. and pho. spectra to spectra obtained from MinBias data.	53
3.12 (Color online) ϕ vs. η distribution from $Au+Au$ at $\sqrt{s_{NN}} = 62.4$ GeV showing the masked TPC sector in RHIC run year 2010.	55
3.13 (Color online) Low- p_T photonic-electrons inv. mass dist. in p_T -bins. Also shown for every p_T bin the distribution of the partner track $n\sigma_e$; since no eID cuts are placed on the partner the $n\sigma_e$ distribution serves as another photonic electrons purity check.	61
3.14 (Color online) Low- p_T photonic-electrons inv. mass dist. in centrality-bins. Also shown for every centrality bin the distribution of the partner track $n\sigma_e$; since no eID cuts are placed on the partner the $n\sigma_e$ distribution serves as another photonic electrons purity check.	62
3.15 (Color online) High- p_T photonic-electrons inv. mass dist. in centrality-bins. Also shown for every centrality bin the distribution of the partner track $n\sigma_e$; since no eID cuts are placed on the partner the $n\sigma_e$ distribution serves as another photonic electrons purity check.	63
3.16 (Color online) (Top two rows) BTOW($\Delta\phi$) distributions after applying all eID cuts except cut on BTOW($\Delta\phi$), the eID cut chosen is $ \text{btow}\Delta\phi < 0.05$. (Bottom two rows) BTOW(Δz) distributions after applying all eID cuts except cut on BTOW(Δz) itself, the eID chosen is $ \text{btow}\Delta z < 10$ cm. Two p_T -bins are shown for 0 – 80% centrality and one p_T -bin for all other centralities.	64

Figure	Page
3.17 (Color online) (Top two rows) $\text{BSMD}\eta(\Delta\phi)$ distributions after applying all eID cuts except cut on $\text{BSMD}\eta(\Delta\phi)$ itself, the chosen eID cut is $ \text{bsmd}(\eta)\Delta\phi < 0.06$. (Bottom two rows) $\text{BSMD}\eta(\Delta z)$ distributions after applying all eID cuts except cut on $\text{BSMD}\eta(\Delta z)$ itself, the chosen eID cut is $ \text{bsmd}\eta\Delta z < 3.0$ cm. Two p_T -bins are shown for 0 – 80% centrality and one p_T -bin for all other centralities.	65
3.18 (Color online) (Top two rows) $\text{BSMD}\phi(\Delta\phi)$ distributions after applying all eID cuts except cut on $\text{BSMD}\phi(\Delta\phi)$ itself, the chosen eID cut is $ \text{bsmd}(\phi)\Delta\phi < 0.0015$. (Bottom two rows) $\text{BSMD}\phi(\Delta z)$ distributions after applying all eID cuts except cut on $\text{BSMD}\phi(\Delta z)$ itself, the chosen eID cut is $ \text{bsmd}\phi\Delta z < 16.0$ cm. Two p_T -bins are shown for 0 – 80% centrality and one p_T -bin for all other centralities.	66
3.19 (Color online) p/E_0 distributions after applying all eID cuts except cut on p/E_0 itself, the cut is chosen to be $0.3 < p/E_0 < 2.0$. The distributions clearly peak ~ 1.0 as expected from electrons, the slight shift to higher than 1.0 is because the energy of the highest tower E_0 is used instead of the cluster energy E . Two p_T -bins are shown for 0 – 80% centrality and one p_T -bin for all other centralities.	67
3.20 (Color online) Low- p_T $n\sigma_e$ distribution in p_T -bins, the eID cut chosen is $0 < n\sigma_e < 2.0$, due to the approximate symmetry of the $n\sigma_e$ distribution such a cut has a $\sim 50\%$ efficiency, however it ensures a pure photonic electrons sample. The artificial cut which appears on the left shoulder of the distributions is applied in the original data structure production used in this analysis to suppress the size of the files.	68
3.21 (Color online) High- p_T $n\sigma_e$ distributions in centrality-bins, the eID cut chosen is $0 < n\sigma_e < 3.0$, due to the approximate symmetry of the $n\sigma_e$ distribution such a cut has a $\sim 50\%$ efficiency, however it ensures a pure photonic electrons sample. The artificial cut which appears on the left shoulder of the distributions is applied in the original data structure production used in this analysis to suppress the size of the files.	69
3.22 (Color online) Inv. mass distr. w/o BEMC cuts with TOC cuts on partner. The plots clearly show a pure electron sample without BEMC cuts which is necessary to calculate the BEMC efficiency from data.	70
3.23 (Color online) BEMC electrons ident. eff. in centrality bins.	71
3.24 (Color online) Inv. mass dist. w/o TOF cuts with TOF cuts on partner in p_T -bins.	72
3.25 (Color online) Inv. mass dist. w/o TOF cuts with tight partner cuts in centrality bins.	73

Figure	Page
3.26 (Color online) (Left) TOF matching and elec. ident. eff. (Right) Total TOF eff.	73
3.27 (Color online) $n\sigma_e$ electrons ident. eff. in centrality bins.	74
3.28 (Color online) Overall electrons ident. eff. in centrality bins.	75
3.29 (Color online) Comparison of reconstructed from embedding (red) to photonic electrons from data (blue).	76
3.30 Single track reconstruction efficiency in centrality bins.	77
3.31 (Color online) A comparison of the mass shape of electron-positron pairs from π^0 and η Dalitz decays from PYTHIA and modified STAR GEANT routines. (Left) PYTHIA and GEANT are in perfect agreement for the π^0 Dalitz decay. (Right) A mismatch is observed between the PYTHIA and the modified GEANT in the case of η Dalitz decay.	78
3.32 (Color online) Fits to $Au+Au$ pions yields. Data is combined from STAR charged pions measurement [79] and PHENIX neutral pions measurement [80].	80
3.33 (Color online) Photonic electrons from γ conversion, π^0 and η Dalitz decays reconstruction efficiency.	81
3.34 Final photonic electrons reconstruction efficiency shown with the relative systematic uncertainty band.	83
3.35 (Color online) Example of purity fits.	84
3.36 Examples of electron purity. Shaded region is excluded because of proton dE/dx band crossing, see text.	85
3.37 (Color online) (Left) PYTHIA spectra. (Right) Cocktail relative contributions.	86
3.38 (Color online) Comparison of measured photonic electrons to cocktail yields.	88
3.39 (Left) J/ψ from CEM and electrons from $J/\psi \rightarrow e^+e^-$ PYTHIA decay. (Right) Rapidity distributions.	90
3.40 CEM band scaled by N_{bin} and $R_{AA} = 0.75 \pm 0.25$ compared to STAR measurement of J/ψ in $Au+Au$ at $\sqrt{s_{NN}} = 62.4$ GeV [84].	91
3.41 Top two panels, uncertainty band of $J/\psi \rightarrow e^+e^-$ contribution to non-photonic electron shown as ratio to $p+p$ theory prediction from FONLL (right) and from k_t factorization (left). Lower plot shows the break down of the uncertainty.	92

Figure	Page
4.1 Non-photonic electrons to photonic electrons ratio in $Au+Au$ collisions at $\sqrt{s_{NN}} = 200$ GeV. Error bars are statistical errors, and square brackets are point-by-point systematic uncertainties.	93
4.2 (Color Online) Differential invariant yields vs. p_T of non-photonic electrons in $Au+Au$ at $\sqrt{s_{NN}} = 200$ GeV, and scaled STAR published $p+p$ [68]. Error bars and boxes are statistical and systematic errors, respectively. FONLL predictions are scaled by N_{coll} and shown as curves.	94
4.3 (Color Online) Data over FONLL [46]. Bars and brackets are statistical and systematic errs, respectively.	95
4.4 (Color Online) Non-photonic electrons nuclear modification factor in $Au+Au$ collisions at $\sqrt{s_{NN}} = 200$ GeV in different centralities. Bars and brackets are statistical and systematic errors, respectively. Error boxes are the uncertainties from the $p+p$ baseline measurement.	96
4.5 (Color Online) (Left) Non-photonic electrons azimuthal anisotropy, $v_2\{2\}$, $v_2\{4\}$ and $v\{EP\}$ at $\sqrt{s_{NN}} = 200$ GeV. Bars and brackets are statistical and systematic errors, respectively.	97
4.6 (Color Online) (Top) Non-photonic electrons nuclear modification factor, R_{AA} , at $\sqrt{s_{NN}} = 200$ GeV compared to models [85–88]. Grey band is light hadrons R_{AA} . Error bars and brackets are Au+Au statistical and systematic errors, respectively. Error boxes are the uncertainties from our baseline $p + p$ measurement. (Bottom) Non-photonic electrons azimuthal anisotropy compared to models.	99
4.7 Non-photonic electrons to photonic electrons ratio in 0 – 80% centrality $Au+Au$ collisions at $\sqrt{s_{NN}} = 62.4$ GeV.	102
4.8 (Color Online) Differential invariant yields vs. p_T of non-photonic electrons in $Au+Au$ collisions at $\sqrt{s_{NN}} = 62.4$ GeV. Bars and brackets are statistical and systematics errors, respectively. Measurement at ISR in $p+p$ collisions at $\sqrt{s_{NN}} = 62.2$ GeV scaled by N_{coll} is also plotted [100]. FONLL predictions are scaled by N_{coll} and shown as curves.	103
4.9 (Color Online) (Left) Differential invariant yields vs. p_T of non-photonic electrons in $Au+Au$ collisions at $\sqrt{s_{NN}} = 62.4$ GeV. Bars and brackets are statistical and systematics errors, respectively. k_t -fact. spectra is scaled by N_{coll} and shown as curves. (Right) Comparison of ISR measurement, FONLL and k_t -fact. predictions for non-photonic electrons invariant cross-section in $p+p$ collisions at $\sqrt{s_{NN}} = 62.4$ GeV.	104

Figure	Page
4.10 Non-photonic electrons spectra over N_{bin} scaled FONLL prediction compared to FONLL uncertainty band (Left), N_{bin} scaled k_t -factorization prediction (Right).	105
4.11 (Color Online) Uncorrected inclusive and photonic electron distributions measured in minimum-bias $Au+Au$ collisions at $\sqrt{s_{NN}} = 39$ GeV.	106
4.12 (Color Online) v_2 from two-particle correlations at $\sqrt{s_{NN}} = 39$ and 62.4 GeV compared to $\sqrt{s_{NN}} = 200$ GeV. Bars and brackets are statistical and systematic errors, respectively.	106

ABSTRACT

Mustafa, Mustafa Ph.D., Purdue University, August 2013. Experimental Study of Electrons from Heavy Flavor Hadrons Decays in Au+Au Collisions at 200, 62.4 and 39 GeV in the STAR Experiment at RHIC. Major Professor: Wei Xie.

Zero baryon density Lattice QCD calculations confirm the existence of a deconfined state of partonic matter at very high temperatures and energy densities, such a state, called the Quark Gluon Plasma (QGP), is argued to feature a major phase of the expanding matter created in Heavy Ion Collisions (HIC) at RHIC [1–4] and the LHC experiments. Many developments on the quantitative description of QGP have been worked out by the different experimental groups, however the picture is far from complete.

Unlike light quarks, heavy quarks are created at the very early stages of the collision, their numbers are almost conserved throughout the expansion and their interactions with the medium is amenable to perturbative QCD calculations. Therefore, comparing their kinematics in heavy-ion collisions to theoretical calculations offers a unique opportunity to extract medium properties and constrain the dynamics of the high transverse momentum (high- p_T) partons interaction with the medium. So far, experiments studied two observables of heavy quarks. Firstly, the modification of heavy quarks production in presence of the QGP compared to the baseline production in $p+p$ and $d+Au$ collisions. Secondly, to understand the involvement of heavy quarks in the collective motion of the bulk medium expansion, azimuthal anisotropy measurements are invoked.

Our research focuses on simultaneous measurements of azimuthal anisotropy and production of electrons from heavy flavor semi-leptonic decay channels. The strong modification of the production of these electrons in $Au+Au$ collisions compared to $p+p$ at $\sqrt{s_{NN}} = 200$ GeV surprised the community; early calculation of medium-

induced gluon radiation , which describes the energy loss of light quarks, predicted much less suppression for heavy flavor quarks. This led to a variety theoretical proposals for energy loss mechanisms to account for this strong suppression. Understanding which theoretical model(s) provide the most accurate description of experimental measurements has many physical implications on the flavor dependence of energy loss, heavy quarks-medium interaction strength and their degree of thermalization, constraining the decoupling temperature of heavy quarks from the bulk matter, in addition to delineating the importance of the different hadronization mechanisms to the different heavy quarks kinematical domains. At this stage it is evident that experiments at RHIC and the LHC need to provide higher precision differential measurements to better distinguish between the plethora of energy loss models currently available.

To this end, in this work, we present a simultaneous measurement of mid-rapidity heavy flavor electron differential invariant yields and azimuthal anisotropy in $Au+Au$ collisions at $\sqrt{s_{NN}} = 200$ GeV. The novelty of the new invariant yield measurement lies in the highly improved statistical precision it provides. This new measurement allows us to recalculate the heavy flavor electron nuclear modification factor using published STAR $p+p$ results as a baseline. We also extend heavy quarks production studies to lower center-of-mass collision energies. In this quest, we seek to see if the energy loss of heavy quarks is lessened or turned off at lower energies or constrain the onset collision energy of heavy quarks suppression and flow. Therefore, we also present measurements of mid-rapidity differential invariant yield at $\sqrt{s_{NN}} = 62.4$ and azimuthal anisotropy at $\sqrt{s_{NN}} = 39$ and 62.4 GeV.

1. INTRODUCTION

1.1 Quantum Chromodynamics

1.1.1 Quark Model

The *Quark Model* emerged amidst the atmosphere of frustration which prevailed the 1950s and 1960s particle physics community over the eruption of the "seemingly" chaotic hundreds of particles from experiments and the failure of many attempts to find satisfying scheme to categorize them (some went to even propose to consider all of them as being equally elementary, see *David Gross's* 2004 Nobel Lecture for an interesting account of the history leading to QCD [5]).

It was in year 1964 that *Murray Gell-Mann* [6] and *George Zweig* [7, 8], independently, proposed to use $SU(3)$ symmetry and "assume" three spin-1/2 fermions carrying fractional charge and symmetry breaking mass (this $SU(3)$ flavor symmetry is broken by the mass) to explain how the mesons and baryons can be assembled from more elementary particles. The term "quarks" was coined by *Gell-Mann* in his 1964 Physics Letter [6] where he, in two short paragraphs, laid out the essential rules to construct mesons from a quark and an anti-quark ($q\bar{q}$) or baryons from three quarks (qqq). In their papers both *Gell-Mann* and *Zweig* urged for a search for fractionally charged particles in high energy experiments. *Gell-Mann* suggested that these quarks are a mathematical convenience and his invitation was conservative in that sense, "A search for stable quarks of charge $-\frac{1}{3}$ or $+\frac{2}{3}$ and/or stable di-quarks of charge $-\frac{2}{3}$ or $+\frac{1}{3}$ or $+\frac{4}{3}$ at the highest energy accelerators would help to reassure us of the non-existence of real quarks" [6].

Four years later, in 1968 *Deep-Inelastic-Scattering* (DIS) experiments, the evidence for the existence of quarks and the substructure of hadrons was experimentally revealed. The impinging electrons on protons and neutrons at Stanford Linear Ac-

celerator Center (SLAC) showed that they indeed have point like “deflection” centers (named “partons” by Feynman) and that they carry fractional charges as outlined by the *Quark Model*. In those years, to resolve the apparent violation of Pauli exclusion principle caused by discovering spin-3/2 baryons like Δ^{++} which had 3 up quarks with aligned spins with the same quantum numbers, the concept of color came into existence [9]. By carrying a color degree-of-freedom the three fermions form a spin-3/2 ground state. The additional color degree-of-freedom was formalized in the proposal that color charge defines a local $SU(3)$ symmetry which was used to define and formulate a quantum field theory of the strong interaction, *Quantum Chromodynamics* (QCD).

1.1.2 QCD Lagrangian

Quantum Chromodynamics, is a non-abelian (Yang-Mills) quantum field theory which is invariant under color $SU(3)$ local transformations and it describes the strong interaction between colored fractionally charged spin-1/2 quarks in addition to 8 spin-1 gluons as the theory gauge bosons from the adjoint representation of $SU(3)$. The QCD Lagrangian is deceptively similar to that of *Quantum Electrodynamics* (QED)

$$\mathcal{L}_{\text{QCD}} = \sum_{i=\text{flavor}} \bar{\psi}_i (i\gamma^\mu D_\mu - m_i) \psi_i - \frac{1}{4} \sum_{a=\text{gluons}}^8 G_{\mu\nu}^a G_a^{\mu\nu} \quad (1.1)$$

where ψ_i are the quarks Dirac spinor fields, $G_{\mu\nu}^a$ are the gluon fields strength tensor, $D_\mu = \partial_\mu - igA_\mu(x)$ is the gauge covariant derivative written in terms of $A_\mu(x)$ gluons (gauge fields) and g is the dimensionless coupling constant of the strong force. To satisfy gauge invariance under the $SU(3)$ non-abelian group transformations the field strengths tensor is constructed as

$$G_{\mu\nu}^a = \partial_\mu A_\nu^a(x) - \partial_\nu A_\mu^a(x) + gf_{abc} A_\mu^b(x) A_\nu^c(x) \quad (1.2)$$

where f_{abc} are the anti-symmetric structure constants of $SU(3)$ [10]. Apart from the non-linear term in the field strength tensor the QCD Lagrangian resembles the QED

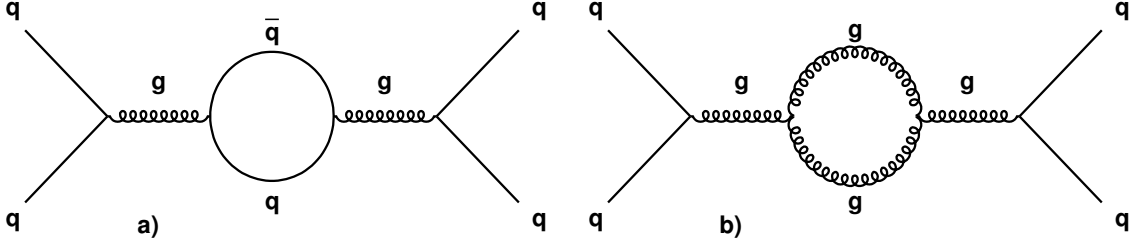


Figure 1.1.: First order Feynman diagrams showing a) screening and b) anti-screening.

Lagrangian. It is this very term which arises in non-abelian theories that makes QCD a much richer theory. In QCD gluons are colored and they interact through the strong force, in fact the gluon vertex (absent in QED) exists.

1.1.3 Asymptotic Freedom

The first order Feynman diagrams showing the polarization of vacuum as a response to the presence of charge are shown in Fig.1.1. In QED only the left diagram exists and it gives rise to screening of the electric charge by the virtual electron-positron pairs which work to partially screen electric charge in QED. The result is that the QED coupling constant (effective electron charge) is scale dependent. Specifically, it increases as one gets closer to the charge source (technically known as Landau pole behavior). The screening diagram also exists in QCD; quark-antiquark pairs pop out of vacuum due to the presence of color charge. However, anti-screening diagram (Fig.1.1 right) also exists in QCD. It was proven that whether screening or anti-screening prevails at shorter distances in non-abelian gauge theories depends on the number of flavors of particles in the theory. In fact, the scale dependence of the coupling constant at leading order is expressed through α_s (the theory equivalent to the fine structure constant $\alpha_s \stackrel{\text{def}}{=} \frac{g^2}{4\pi}$) [10] is

$$\alpha_s(Q) = \frac{\alpha_s}{1 + (11n - 2n_f)(\alpha_s/6\pi) \ln(Q/\mu)} \quad (1.3)$$

where n is the number of colors and n_f is the number of quarks flavors, μ is the scaling parameter. So for QCD with 3 colors of $SU(3)$ and six quarks ($2n_f < 33$) anti-screening prevails at short distances and the theory is *asymptotically free*.

Asymptotic freedom of QCD was discovered by *Frank Wilczek*, *David Gross* and *David Politzer* in 1973 and awarded the 2004 Nobel Prize in physics. It is an expression of the fact that at very large transferred momenta Q or equivalently at very short distances the coupling constant of QCD becomes asymptotically weak (technically it states that in non-abelian theories the beta-function can be negative [10]). μ is the scale at which the above relation is derived in context of the underlying renormalization group. It sets the limit between two regimes of QCD, the weak coupling regime where perturbative techniques can be applied, and the non-perturbative regime where the theory remains largely unsolved, more on the latter regime later. In the perturbative regime ($\alpha_s \ll 1$)

$$\alpha_s(Q) = \frac{2\pi}{(11 - \frac{2}{3}n_f) \ln(Q/\Lambda_{QCD})} \quad (1.4)$$

it is customary to quote the value of α_s at a fixed scale, $Q \sim M_z$, the Z boson mass, the world average is $\alpha_s(M_z) = 0.1184 \pm 0.0007$ [11]. Which sets $\Lambda_{QCD} \sim 200$ MeV and it sets the limit where pQCD is valid for roughly $Q \geq 1$ GeV, and the interaction becomes non-perturbative at distances larger than $\sim 1/\Lambda_{QCD} \sim m_n$, m_n is the size of nucleons, the fact that the QCD scale is comparable to the size of the nucleons puts them in the non-perturbative regime, to be discussed below. Fig.1.2 shows a compilation of the world measurements of the coupling constant at different perturbative scales and stands to attest the precision of the verification of this property of QCD (for an illuminating discussion of QCD symmetries, asymptotic freedom and tests of QCD see Frank Wilczek's article [12]).

1.1.4 Non-perturbative QCD

The other side of asymptotic freedom is *confinement*, to this day no colored particle has been observed and the conventional wisdom is that at long distances where QCD

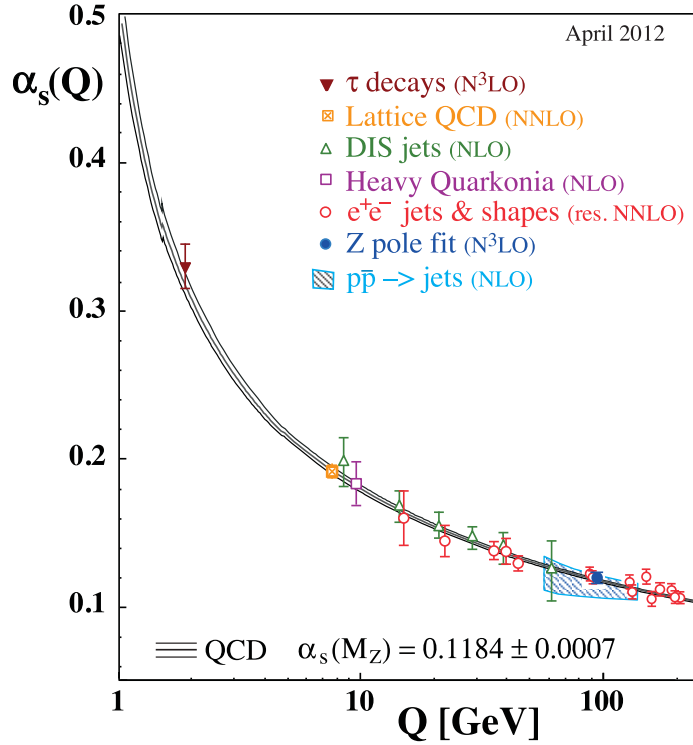


Figure 1.2.: (Color online) A compilation of the world measurements of the running coupling constant α_s as a function of energy scale Q demonstrating asymptotic freedom, figure from [11].

becomes non-perturbative the coupling constant becomes large and the color field lines between, for example, a quark and an antiquark form color flux tubes which confine the color fields and as the distance between the quark and antiquark reaches $r \sim 1 fm \sim 1/\Lambda_{QCD}$ it becomes energetically more favorable for the tubes to fragment into hadrons. Confinement is thought to be a consequence of the gluons carrying charge. Although confinement is supported experimentally by the lack of observation of free quarks or gluons, QCD is still not analytically solved in this regime so confinement is not proven (see *Millennium Prize Problems* by the *Clay Mathematics Institute* [13]).

The study of QCD in the non-perturbative regime remains a daunting task, *Lattice QCD* stands out as the most well-established non-perturbative approach to QCD [11, 14]. In this approach spacetime is discretized and defined on lattice points,

quark fields are defined on these points while the gluon fields are defined on the links which connect neighboring sites. As the lattice spacing is reduced to zero and the lattice size is taken to the infinite limit lattice QCD approaches the continuum limit of QCD. Lattice calculations become more accurate as the spacing is reduced. These calculations are computational resource intensive and many supercomputer facilities have been built around the world to carry these calculations. Lattice QCD remains the most reliable and promising tool to illuminate the non-perturbative regime of QCD, it provided a direct test of confinement of the QCD Lagrangian and accounts very accurately for the hadron masses. As we will see later lattice QCD calculations at finite temperature is a very important tool to study QCD matter, which is the research topic of this PhD. dissertation and the rest of this chapter.

1.1.5 Perturbative QCD

The behavior of QCD coupling at high energies allows to calculate scattering cross-sections using perturbative techniques in the weak coupling regime for high transverse momentum hadrons and jets (high- p_T). Scattering in hadron-hadron collisions involves several stages which are well in the long range regime of QCD. Firstly, the hadrons themselves are QCD bound states and their size is in the order of $r \sim 1\text{fm} \sim 1/\Lambda_{QCD}$. Hadronic wavefunctions in terms of the partonic degrees are not exactly solved. Secondly, once the partonic scattering process happens the conversion of scattered partons into jets of hadrons, as discussed in the previous section, also involves long range interactions and thus is non-perturbative. It is only the partonic scattering process for large transfer momenta that can be calculated using perturbative techniques. Resummation techniques are devised to include contributions from more complicated higher order diagrams, which help improve the calculation accuracy. To deal with this the pQCD scattering cross-sections are done using the factorization scheme where it has been proven [15, 16] that for leading power ($1/Q$) of the partonic processes one can factorize the cross-section into a calculable weak cou-

pling perturbative part and isolate the non-perturbative long range dynamics of the initial hadrons and final state jets in universal matrix elements which are independent of the partonic process. The matrix elements once measured in one experiment they can applied to calculate pQCD cross-sections of other processes. Schematically, the cross-section calculation for $H_1 + H_2 \rightarrow H_3 + X$ (H are hadrons)

$$d\sigma_{H_1+H_2 \rightarrow H_3+X} = \sum_{a,b,c} f_{a/H_1} \otimes f_{b/H_2} \otimes d\sigma_{a+b \rightarrow c+x} \otimes D_{c/H_3} + \text{higher order terms} \quad (1.5)$$

where the perturbative partonic scattering $a + b \rightarrow c + x$ cross-section is encoded in $d\sigma_{a+b \rightarrow c+x}$, $f_{a/H}$ are the *Parton Distribution Functions* (PDFs) which, in simplified terms, encode the probability to find parton a with a specific flavor and momentum fraction x in hadron H . The last part in the process is the fragmentation of parton c into a hadron H_3 [11, 16]. This factorization assumes that the scattering process is hard enough for the partons momenta to be regarded as collinear with their parent hadrons with no partons transverse momenta (k_T) smearing. See [16] for a discussion of the assumptions and caveats of this scheme.

Perturbative QCD provides the most reliable tests of QCD and comparison to experiments that we have so far. Event generators which calculate pQCD cross-sections to Leading-Order and Next-to-Leading-Order have been available for a couple of decades now and they are continuously being used to compare to experiments and reliable enough to calculate QCD background for other processes. Fig.1.3 shows comparison of experimental measurements to NLO pQCD calculations demonstrating the precision level of QCD predictions in the perturbative regime.

It is left to mention here that despite the “Extensive empirical evidence [which] validates QCD; nevertheless, numerous phenomena observed in experiments appear to conflict our QCD-based intuition about hadron and nuclear physics” [17].

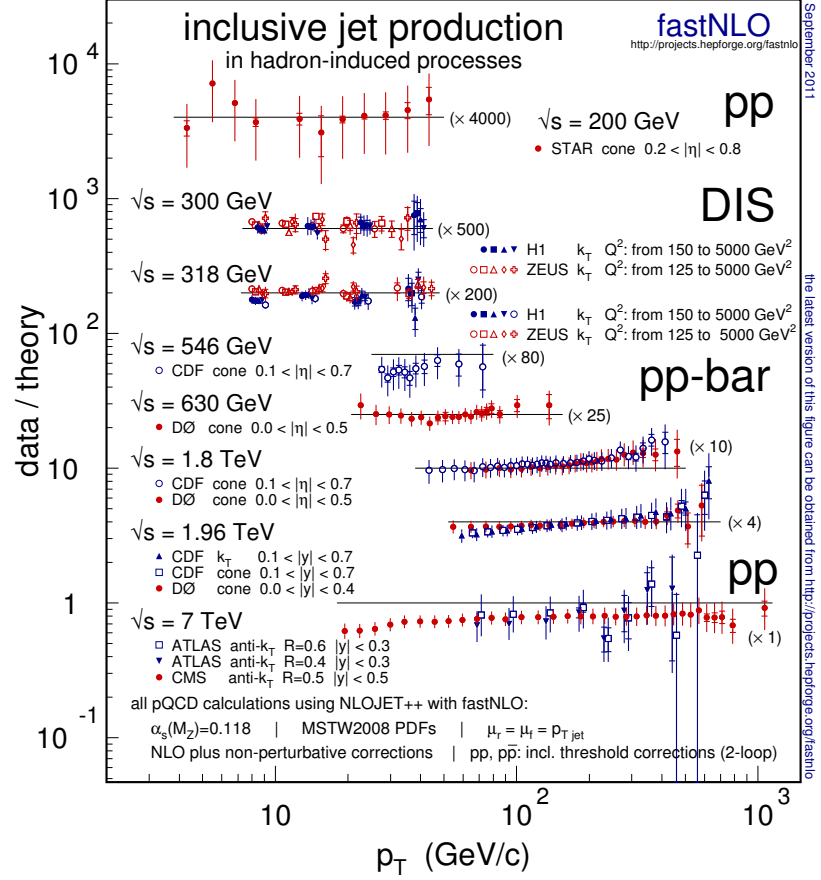


Figure 1.3.: (Color online) A compilation of experimental measurements of inclusive jet production in different collision systems and at different energies compared to NLO pQCD as a function of jet transverse momentum (p_T). Figure extracted from [11].

1.2 Quark-Gluon Plasma

1.2.1 Phase diagram

Fig.1.4 shows the conjectured phase diagram of QCD as typically shown with temperature on the y-axis and baryon density or baryo-chemical potential (μ_B) on the x-axis. At sufficiently high temperature or baryon density nuclear matter is expected to go into a *Quark-Gluon Plasma* phase where, as a result of the extremely high

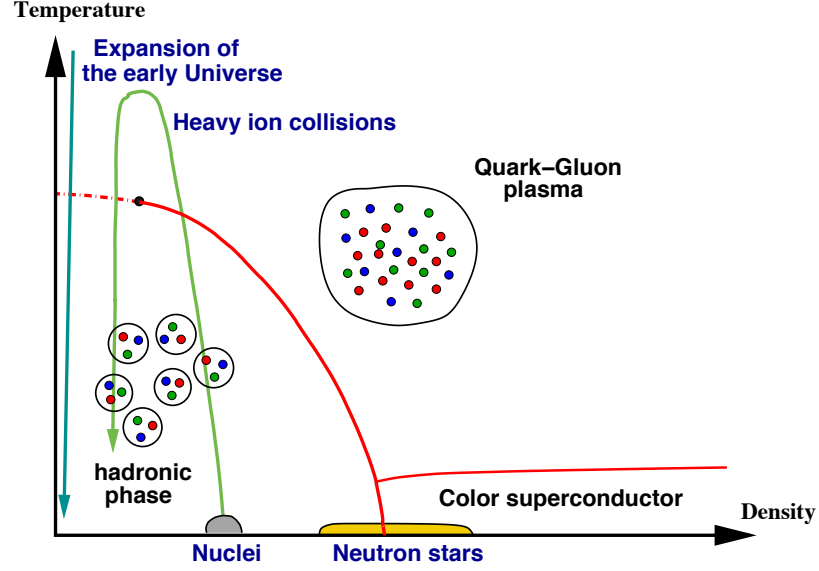


Figure 1.4.: Conjectured QCD phase diagram. Figure extracted from [18]. Only QGP phase is discussed here, for a wider overview of the QCD phase diagram see [19].

densities, partons are no longer confined in the $r \sim 1\text{fm}$ hadrons. Quarks and gluons become the degrees of freedom in this phase and the interactions are dominated by the strong force. Because of asymptotic freedom, at very high densities and short inter-partonic distances matter become weakly coupled and can be thought of as a relativistic gas, using Fermi-Dirac and Bose-Einstein distributions the energy density in such a gas is

$$\varepsilon = (g_b + \frac{7}{8}g_f) \frac{\pi^2}{30} T^4 \quad (1.6)$$

here g_b and g_f are the bosonic and fermionic degrees of freedom respectively. So pressure $P = \varepsilon/3$ and entropy $s = (4/3)(\varepsilon/T)$. Quarks have color, charge, and spin degrees of freedom, and there are 8 massless gauge gluons with two polarization states for each. If we try to estimate the equilibrium temperature between a gas of pions and a QGP relativistic gas, we get for two quark flavors

$$P_{QGP} = \frac{\varepsilon_{QGP}}{3} = (8 \times 2 + \frac{7}{8}(2 \times 3 \times 2 \times 2)) \frac{\pi^2}{90} T^4 = \frac{37\pi^2}{90} T^4$$

A gas of pions has three degrees of freedom, but it also receives another term for an inward confining bag pressure B (MIT bag model), so

$$P_\pi = \frac{3\pi^2}{90}T^4 + B$$

By equating P_π and P_{QGP} and solving for temperature we find $T_c \approx 0.72B^{1/4}$. So for the MIT bag constant $B^{1/4} = 200$ MeV, $T_c \approx 144$ MeV. So an equilibrium pressure exists between the two phases at this T_c . All of these estimates are reasonable except that they are not with the correct equation of state (EoS) for the QGP which can be done in lattice QCD.

1.2.2 Lattice QCD

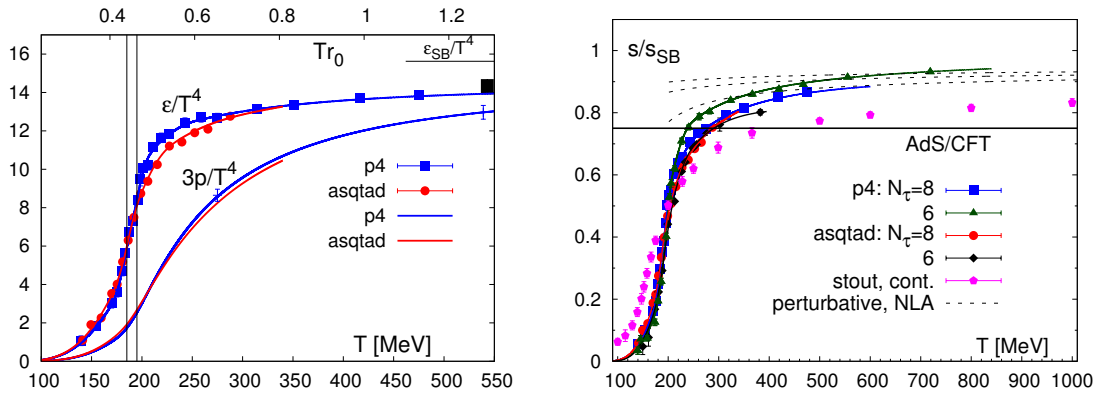


Figure 1.5.: (Left) Energy density and EoS from lattice QCD calculations showing a transition to partonic degrees of freedom at $T_c \approx 175$ MeV, the arrow indicates the relativistic gas limit. (Right) Lattice QCD entropy density divided by the relativistic gas value. Figures extracted from [20]

Lattice QCD calculations at finite temperature are the most reliable non-perturbative approach to study QCD phase transition(s) at zero-baryon density [20–22]. Fig.1.5 left shows lattice QCD calculation for the energy density and EoS as a function of the temperature. A rapid change in the energy density near a critical temperature $T_c \approx 175$ MeV is evident (confer to the crude estimate in the previous section). The

critical energy density is $\varepsilon_c = 0.7 \text{ GeV}/fm^3$ which is ~ 5 times the cold nuclear matter energy density $\sim 0.15 \text{ GeV}/fm^3$. Fig.1.5 right shows the entropy density divided by the relativistic gas value as a function of temperature. As can be seen in the plots, the thermodynamic values seem to reach saturation at $\sim 2T_c$ and stay below the relativistic gas limits, a clear indication that even at these high temperatures the partonic gas is still interacting, this is also supported by the less dramatic change in the EoS in the right plot.

Lattice calculations have also shown that the nature of the transition depends on the mass values of the light and strange quarks, at the physical quark values the transition is a rapid cross-over [20]. So from lattice the transition at zero-baryon density in the phase diagram (Fig.1.4) is a cross-over which happens near $T_c \approx 175 \text{ MeV}$. Lattice QCD calculations at finite baryon density are still not reliably possible, so the rest of the phase diagram including the possible 2nd order phase transition at the critical point and first-order transition at higher baryon densities are all conjectures from model calculations [19]. Lattice QCD calculations also show the expected restoration of chiral symmetry at high temperatures; the symmetry breaking QCD vacuum condensate $\langle \bar{\psi}\psi \rangle$ melts at high temperatures. Both, deconfinement and chiral transition order parameters, have been studied in lattice QCD [20].

QGP is believed to have existed in the early universe, a few tens of microseconds, after the big bang. The state, probably, also exists in the core of neutron stars. Both possibilities are separated from us by either time or space. There is evidence that QGP features a major phase in heavy-ion collisions, these are being studied in labs around the world. Next section entails a discussion of the major features and signals of QGP in heavy-ion collisions.

1.3 Heavy-Ion collisions

Heavy-Ion collisions have been a vigorous active field of research for more than two decades. Heavy-ions have been previously studied at AGS (BNL, USA) and SPS

(CERN, Switzerland). Since year 2000, the Relativistic Heavy Ion Collider (RHIC) (BNL, USA), the world's first dedicated heavy-ion collider, have been providing collision to its two large experiments PHENIX and STAR, and its two smaller experiments BRAHMS (completed its operation in 2006) and PHOBOS (completed its operation in 2005). In 2005, the four RHIC experiments presented their results from the first four years runs of RHIC in white papers [1–4], the white papers argued that a Quark-Gluon Plasma phase features a major stage in the evolution of the fireball created in head-on $Au+Au$ collisions at its highest center-of-mass collision energy, $\sqrt{s_{NN}} = 200$ GeV. The major features of heavy-ion collisions and signals of the QGP will be presented in this section. The Large Hadron Collider (LHC) (CERN, Switzerland) started colliding $Pb+Pb$ collisions since late 2010 at center-of-mass energies 14 times larger than at RHIC, which provides higher energy densities, fireball size and longer lifetime. Heavy-ion results from LHC, experiments, ALICE, ATLAS and CMS have confirmed many of the RHIC findings of the properties of the QGP phase and extended them in many ways, e.g. higher transverse momenta, event-by-event analysis, and jet reconstruction capabilities. Reviews of the LHC results are available in publications, for example see [23, 24] and references therein. The LHC has also collided $p+Pb$ in late 2012 and early 2013 for studies of Cold Nuclear Matter effects (physics which is background to the study of QGP) and initial energy densities and dynamics which already yielded many exciting results [25, 26].

1.3.1 Heavy-Ion collision stages

Fig.1.6 shows a schematic of the stages of a heavy-ion collision event. Initially the two ions are Lorentz contracted longitudinally so they have a pancake shape. At high energies the ions wavefunctions are dominated by soft gluons which carry very small fraction of the longitudinal momentum ($\langle x \rangle \approx 10^{-2}$ at RHIC top energy ¹). It is proposed that the description of these universal gluon clouds is best done in an effective

¹The average transverse momentum of produced hadrons at RHIC is below 1 GeV and for central rapidities using $x = (p_{T_a} e^{y_a} + p_{T_b} e^{y_b}) / \sqrt{s}$ gives $\langle x \rangle \approx 10^{-2}$.

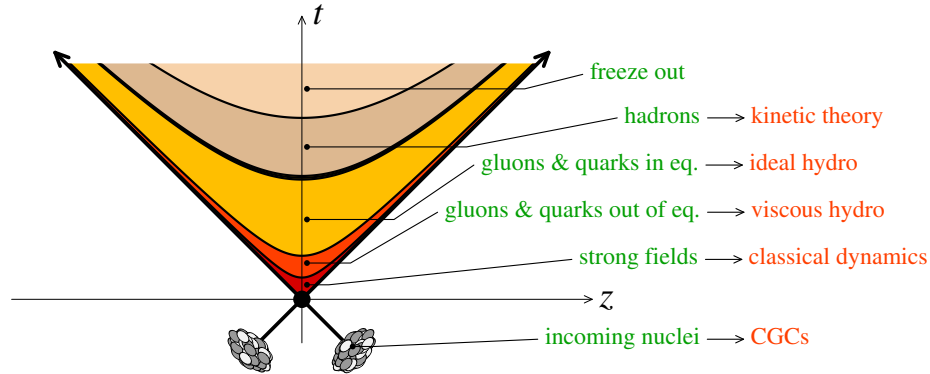


Figure 1.6.: A schematic diagram showing the conventional stages of heavy-ion collisions. Figure extracted from [18].

theory that is a classical limit of QCD called the Color-Glass Condensate (CGC) [27]. The collision event itself is conventionally thought to have three stages, the initial state of gluonic balls first interaction (CGC and glasma) where all the Cold Nuclear Matter effects originate (modification of the nuclear partons distributions functions, Cronin), and two re-scattering stages: a near-zero viscosity partonic scattering phase (strongly interacting Quark-Gluon Plasma) and a hadronic re-scattering stage.

At the very early stage of the partonic phase, for a short time, the interaction in the medium is likely to be weak due to asymptotic freedom, so partons have a relatively longer mean free path resulting in higher viscosity. As we will see later, the medium in this case can be described by viscous relativistic hydrodynamics. As the partonic medium cools down the interactions in the medium become stronger and partons have a short mean free path resulting in a near conjectured theoretical minimum viscosity over entropy ratio [28], such a phase is possible to describe using hydrodynamics in the vanishing mean free path limit, ideal hydrodynamics. The best hydro description of the experimental data implement viscous corrections.

As the fireballs expands more, the energy density drops down and the medium hadronizes, the hadrons chemistry is likely to be fixed at this stage, and thus it is called the *chemical freeze-out*. Hadrons continue to interact elastically as expansion

continues, once the mean free path of hadrons become larger than the system size the interaction cease to happen, this stage is known as the *kinetic freeze-out*.

In the following, we will discuss a few concepts related to the study of heavy-ion collisions, and the different signals used to argue for the existence of a QGP phase.

1.3.2 Particle production

There are several models to describe the total cross-section in heavy-ion collisions [29], the conventionally simple model is to break the total cross-section into hard spectra and soft spectra. The hard processes require a large momenta transfer and by the uncertainty principle they happen very early in the collision. Such processes have a short coherence length so the number of hard particles scale with the number of nucleon nucleon binary collisions (N_{bin}). The soft process on the other hand are produced in small momentum transfer scattering and have a coherence length that is larger than the mean free path, so multiple collisions happen before a gluon is radiated, this makes the number of soft particles scale with number of nucleons participating in the collisions (N_{part}). The *Two-component model* relies on this categorization of particle production to account for the particle production in heavy-ion collisions, according to this model the total cross-section in heavy-ion collisions is written as

$$\frac{dN_{ch}}{d\eta} = n_{pp} \left[(1-x) \frac{\langle N_{part} \rangle}{2} + x \langle N_{bin} \rangle \right] \quad (1.7)$$

where η is psuedo-rapidity, n_{pp} is the multiplicity in $p+p$ collisions and x is the fraction of process scaling as hard collisions [30].

1.3.3 Centrality

It is not possible to experimentally measure the real impact parameter in collisions, so we resort to use a proxy parameter whose average varies monotonically with the real impact parameter. One such parameter is the number of charged particles (N_{ch}) produced in certain region of phase space. Fig.1.7 shows mid-rapidity charged

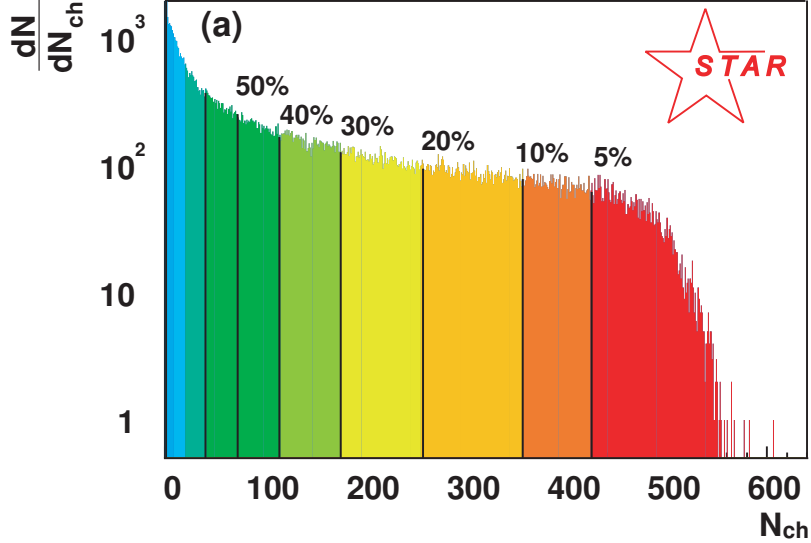


Figure 1.7.: (Color online) Centrality selection from charged particle multiplicity distribution in $Au+Au$ at $\sqrt{s_{NN}} = 130$ GeV. Plot from [29].

particle multiplicity distribution in $Au+Au$ collisions at $\sqrt{s_{NN}} = 130$. The distribution is biased towards low multiplicity (notice the log-scale), most of the events have a large impact parameter with a low number of participants (peripheral collisions). Zero impact parameter (most central collisions) have a large number of participants and large multiplicities. The multiplicity distribution is divided into *centrality* classes, in a sense that the $0 - n\%$ centrality are the events which produce the highest $n\%$ of the multiplicity distribution. Fig.1.7 illustrates this categorization. Monte-Carlo simulations of a geometric model of collisions known as Glauber model is traditionally used to relate the centrality classes to impact parameter, N_{bin} and N_{part} , via a procedure outlined in [31].

1.3.4 Signals of QGP I - Energy density

Quoting an energy density of heavy-ion collision is somewhat a subjective matter; one needs to be careful to which phase of the fireball his estimates are valid. For example, BRAHMS has measured the mean energy loss per participant in $Au+Au$

collisions at $\sqrt{s_{NN}} = 200$ GeV to be $\Delta E = 73 \pm 6$ GeV [32], so in the 0 – 5% central events where ~ 325 nucleons participate in the collision ~ 24 TeV are deposited in the initial fireball, which yields an energy density $\varepsilon \sim 10^3$ GeV/fm³. Such energy densities are ephemeral for any particle interactions to happen and they do not represent the energy density of the QGP phase. Another estimate uses classical Bjorken argument

$$\varepsilon = \frac{dE_T}{dy} \frac{1}{\tau_0 \pi R^2}$$

where E_T is the observed transverse energy or produced particles, the radius $R \approx 1.2A^{1/3}$. Such estimates are completely dependent on the “arbitrary” choice of a formation time τ_0 value. A value of 5.4 GeV/fm³ at RHIC top energy assumes $\tau_0 \sim 1$ fm/c. Same arguments are made in PHENIX white paper [2], their more careful treatment yields a “conservative lower limit” of $\langle \varepsilon \rangle = 15$ GeV/fm³ which is well above the critical energy density of QGP from Lattice QCD as we have seen in the previous section.

1.3.5 Signals of QGP II - Statistical hadronization

If hadrons are produced in thermal equilibrium at the chemical freeze-out of the fireball their yields are expected to follow the statistical distributions

$$n_i = \frac{g_i}{2\pi^2} \int_0^\infty \frac{p^2 dp}{\exp[(E_i - \mu_i)/T] \pm 1} \quad (1.8)$$

where n_i is the density of species i , g_i is the degeneracy factor, $E_i = \sqrt{m_i^2 + p_i^2}$, μ_i is the chemical potential and T is the temperature at freeze-out. Strangeness conservation requires $\mu_s = 0$ for the whole system. So the particle yields can be fitted with two parameters, T and μ_B (and a strangeness suppression factor discussed below). Fig.1.8 shows fits to particles ratios at RHIC top energy (Left) [1], and at the LHC in $Pb+Pb$ collisions at $\sqrt{s_{NN}} = 2.76$ TeV (Right) [33]. RHIC and LHC freeze-out temperatures from fits are consistent with each other.

While it is true that particle yields are also statistically distributed in $e^+ + e^-$ and $\bar{p} + p$ collisions, those require a strangeness suppression factor (γ_s) to account

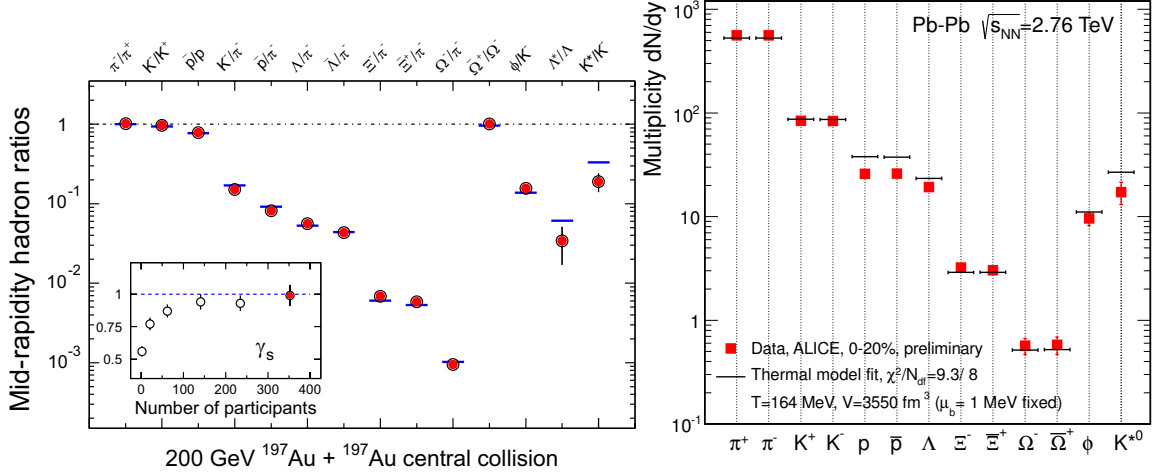


Figure 1.8.: (Left) Ratios of p_T -integrated yields of hadrons in central $Au+Au$ collisions at $\sqrt{s_{NN}} = 200$ GeV from STAR experiment. Thermal model fit parameters yield $T = 163 \pm 4$ MeV, $\mu_B = 24 \pm 4$ MeV and $\gamma_s = 0.99 \pm 0.07$. Inset shows the evolution of the strangeness suppression factor from peripheral to central collision events. Plot extracted from [1]. (Right) Thermal model fits to central $Pb+Pb$ data from ALICE, fit parameters are indicated in the figure (protons and anti-protons are excluded from the fits see reference). Plot extracted from [33].

for the mass suppression of strangeness production. However, if the QCD vacuum condensate evaporates in QGP the threshold energy for strangeness production will be lower [34]. The inset in Fig.1.8(Left) shows the evolution of the suppression factor γ_s used in the fits to particle yields ratios from $\gamma_s \approx 0.7$ in peripheral collisions to $\gamma_s = 0.99 \pm 0.07$ in most central collisions.

1.3.6 Signals of QGP III - Collective motion

In principle, the evolution of the fireball from initial state to final hadrons streaming to the detector can be fully simulated in full transport models. Such an ideal model should be able to take initial energy densities, simulate the full 3 + 1D expansion, account for all the partonic scatterings, correctly hadronize the partons (chemical

freeze-out) depending on densities and partonic mean free path, carry the hadronic re-scattering and then automatically cease the hadronic interactions when the mean free path is larger than the system size. To this date, this mission proved to be tricky to achieve. Instead, the best description of the fireball evolution comes from relativistic hydrodynamics calculations with and without a hadronic re-scattering phase. Below, I will briefly go over the “ingredients” and framework of hydrodynamic models and then present two of the important bulk observables demonstrating collective motion.

Hydrodynamics is an expression of the conservation of energy, momentum and currents of conserved charges throughout the medium evolution, written as

$$\partial_\mu T^{\mu\nu} = 0, \quad \partial_\mu J_i^\mu = 0, \quad (1.9)$$

where $T^{\mu\nu}$ is the energy-momentum tensor and J_i^μ is any conserved current, usually the net-baryon current J_B^μ . Which can be written in terms of the four-velocity vector u^μ as

$$T^{\mu\nu} = (\varepsilon + \mathcal{P})u^\mu u^\nu - \mathcal{P}g^{\mu\nu} + S^{\mu\nu}, \quad J_B^\mu = \rho_B u^\mu, \quad (1.10)$$

where ε is the energy density, \mathcal{P} is the pressure, ρ_B is the baryon density and $g^{\mu\nu}$ is the metric tensor. The first two terms of $T^{\mu\nu}$ represent the non-dissipative, ideal, hydrodynamics limit. $S^{\mu\nu}$ is the viscous correction part, a term that is proportional to the shear viscosity η [35, 36]. The above system of 5 differential equations (considering net-baryon current only) of 6 fields (3 velocity components, energy, pressure and net-baryon densities) is closed by an equation of state (EoS) $\mathcal{P} = \mathcal{P}(\varepsilon, \rho_B)$. The state of the art hydrodynamic models use Lattice QCD parametrized EoS which entails the correct cross-over transition [16, 35].

Historically, before RHIC, it was expected that the partonic matter created in heavy-ion collisions will be weakly coupled, but the success of ideal hydrodynamics at describing the bulk observables from RHIC measurements was indicative of low (near-zero) viscosity QGP phase [1–4]. This was one of the strong evidences from

RHIC to claim the discovery for a strongly-interacting quark-gluon plasma (sQGP), the (near)-perfect fluid [37]. Later as more differential higher precision experimental measurements were made models with viscous corrections, careful treatments of initial energy density fluctuations, hydrodynamic fluctuations and hadronic cascades are more successful at describing data at RHIC and the LHC [35, 36].

For viscosity, hydro-models use empirical values (fit to data) close to the conjectured theoretical-limit viscosity to entropy ratio $\eta/s = 1/(4\pi)$, this value has been obtained in AdS/CFT calculations in the strong coupling limit [18, 35, 36], most models use values $\eta/s \approx 0.16$ at RHIC and ≈ 0.2 at the LHC. Calculations of transport coefficients, η/s and bulk viscosity ζ/s , is not possible from first principles of QCD. Also, it is not straightforward to calculate dynamic quantities in Lattice QCD because of the imaginary-time formalism it uses.

Although hydrodynamic models are doing a very good job at describing many if not most of the bulk observables measured at RHIC and the LHC, hydro has to start at a very early time in the collisions $\tau \approx 0.2 - 0.3 \text{ fm}$ to describe the data, it is not clear what initial state dynamics can drive the system into local thermalization in such a short time. Other than the success of hydrodynamics models in explaining heavy-ion collisions data, no proof exists of such a thermalization. This is still an open problem in the field [36].

The most prominent collective motion observables measured in heavy-ion collisions are azimuthal anisotropy measurements which were proposed very early as a signature of a QGP formation [38]. The overlapping region in non-central heavy-ion collisions ($b > 0$) is anisotropic. If the nucleus-nucleus collisions are a mere superposition of independent nucleon-nucleon collisions, this space anisotropy would not be propagated to the momentum space of emerging particles. However, since this is a strongly interacting medium, the space anisotropy creates pressure gradients which wash out the space anisotropy and maps it into momentum anisotropy. This idea is illustrated in a cartoon in Fig.1.9 (Right).

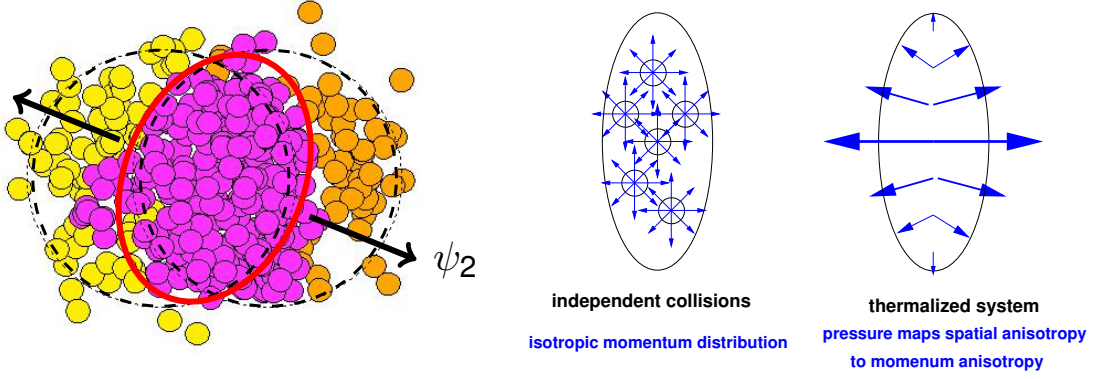


Figure 1.9.: (Left) Near-elliptic shape collisions region in non-central collisions. Figure from [18]. (Right) Interaction maps space anisotropy into momentum anisotropy. Figure from [39].

Azimuthal anisotropy can be studied by expanding the particles yields in Fourier series around the reaction plane azimuth Ψ_{rp}

$$E \frac{d^3 N}{dp^3} = \frac{d^2 N}{2\pi p_T dp_T dy} \left(1 + \sum_{n=1}^{\infty} 2v_n \cos[n(\phi - \Psi_{rp})] \right) \quad (1.11a)$$

$$v_n = \langle \cos[n(\phi - \Psi_{rp})] \rangle \quad (1.11b)$$

the coefficients v_1 and v_2 are called directed and elliptic flow, respectively. Mandated by the initial space near-elliptic almond shape, the elliptic flow v_2 is the largest harmonic coefficient. The correlation between the initial geometry position-space eccentricities ϵ_n and final momentum-space eccentricities v_n is not a trivial issue in real collisions, as shown in Fig.1.9(Left) the initial space geometry is highly irregular due to fluctuations in the energy densities. The correlations between ϵ_n and corresponding v_n in event-by-event viscous hydrodynamics are currently being pursued [40].

Fig.1.10 shows comparison of state of the art event-by-event 3 + 1D viscous hydrodynamic model (MUSIC) to v_2 vs. p_T STAR 10 – 20% centrality from $Au+Au$ collisions at $\sqrt{s_{NN}} = 200$ GeV. The figure also shows another simulation with MUSIC coupled to a hadronic cascade framework (UrQMD). A noticeable improvement

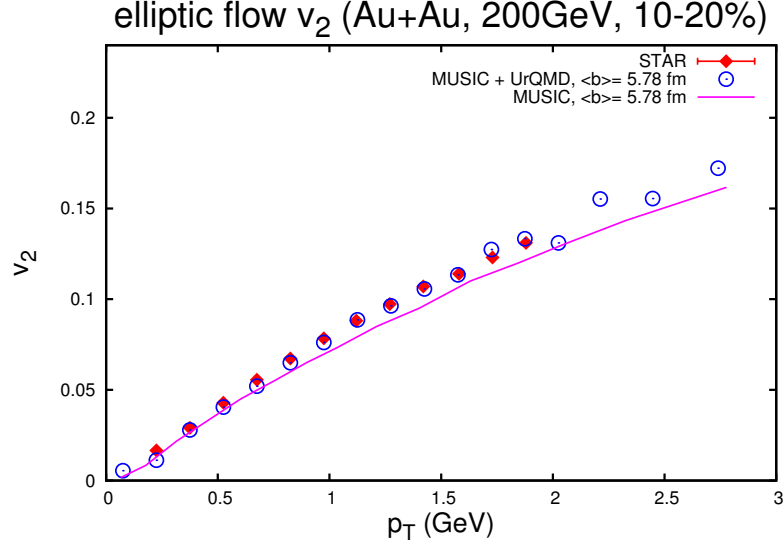


Figure 1.10.: Charged hadrons v_2 vs. p_T for 10 – 20% centrality class in $Au+Au$ collisions at $\sqrt{s_{NN}} = 200$ GeV. Also shown are simulations from 3 + 1D viscous hydro (MUSIC), and MUSIC coupled to a kinetic theory model (UrQMD). Figure extracted from [35].

is achieved by coupling to UrQMD, which, if taken at face value, suggests that 1) most of the v_2 collective flow is developed in the partonic phase, 2) the hadronic re-scattering phase also contributes to building up flow.

1.3.7 Signals of QGP IV - Jet quenching

Another important expected signal of QGP formation is suppression of high transverse momentum partons in central heavy-ion collisions compared to production in vacuum. Basically, high transverse momentum partons lose their virtuality by means of bremsstrahlung through multiple collisions with the much softer bulk matter. Radiation is proportional to the transport coefficient $\hat{q} = \mu^2/\lambda$, where μ^2 is the average momentum transferred in a collision squared and λ is the mean free path. Such radiation is subject to interference effects known in QED as Landau-Pomeranchuk-Migdal (LPM) which is a function of the formation time of gluons; in a dense medium like

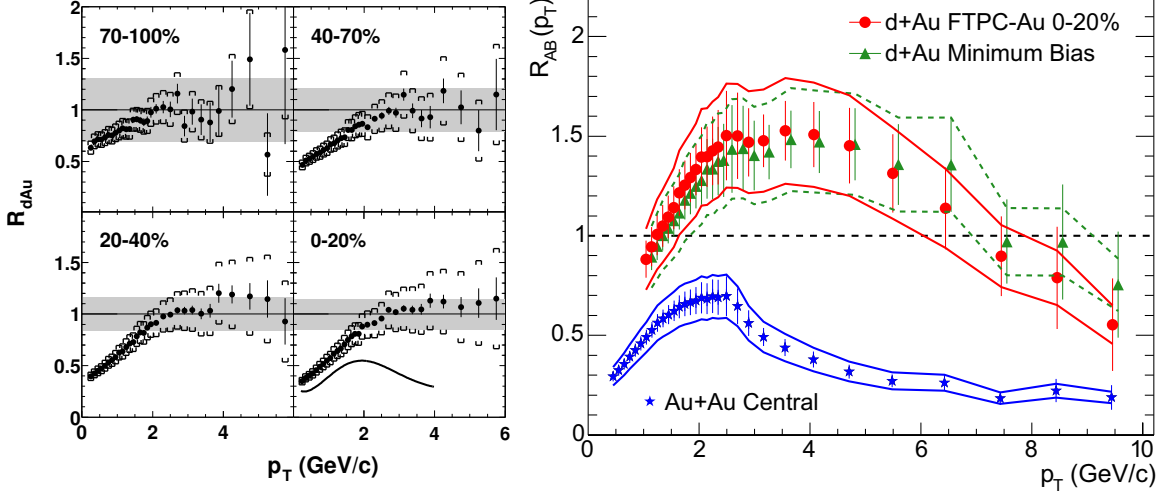


Figure 1.11.: (Left) Results for p_T -dependent charged hadrons R_{dAu} at $\sqrt{s_{NN}} = 200$ GeV in centrality bins from PHOBOS [41]. (Right) MinBias R_{dAu} and central R_{AA} for charged hadrons in $Au+Au$ at $\sqrt{s_{NN}} = 200$ GeV from STAR [42].

the QGP, the typical mean free path ($\sim 0.05\text{fm}$) is very short and multiple collisions happen before the gluon decoheres [16, 39]. Radiative energy loss with the LPM effect taken into account is typically proportional to the traversed path in the medium squared (L^2), this fact will be of importance in the later discussion of path length dependence of energy loss. Partons also lose energy through elastic collisions, but these have been found to be of second order to radiative energy loss [16, 29].

Phenomenologically, this energy loss means a modification of the characteristic pQCD power-law tail of the particles spectra compared to production in vacuum. We can experimentally measure this by comparing the spectra in A-B collisions to that of a baseline in vacuum, $p+p$ collisions, quantified by the nuclear modification factor, R_{AB} , defined as

$$R_{AB}(p_T) = \frac{d^2\sigma^{AB}/dp_T d\eta}{N_{coll}d^2\sigma^{NN}/dp_T d\eta} \quad (1.12)$$

The dependence on impact parameter b is implicit in N_{coll} . Hard processes are expected to scale with number of binary collisions as we discussed earlier. R_{AB}

deviations from unity can be either due to interaction with the final state strongly interacting partonic medium, or due to initial state effects, dubbed cold nuclear matter (CNM) effects, which are not present in the $p+p$ baseline [16, 43]. These CNM effects can be studied in $p+A$ or $d+Au$ collisions where a final state QGP is not formed, by measuring R_{dA} and R_{pA} .

In the absence of a baseline measurement one can also take peripheral events where a QGP is not expected as a baseline. In this case the central-to-peripheral nuclear modification factor is defined as

$$R_{CP}(p_T) = \frac{\langle N_{bin}^{peri} \rangle d^2 N^{central} / dp_T d\eta}{\langle N_{bin}^{central} \rangle d^2 N^{peri} / dp_T d\eta} \quad (1.13)$$

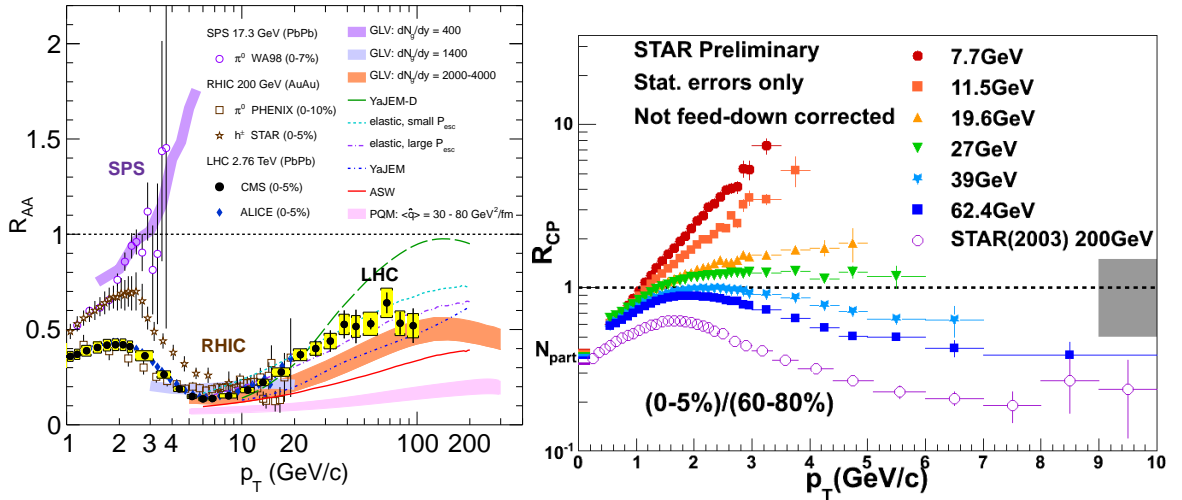


Figure 1.12.: (Color online) (Left) Charged hadrons and neutral pions R_{AA} vs. p_T from several measurements at SPS, RHIC and the LHC (see legend for energies) compared to several energy loss models. Plot extracted from [44]. (Right) Charged hadrons R_{cp} vs. p_T from RHIC Beam-Energy-Scan program the suppression is clearly lessening as energy decreases indicating a possible turn-off of the energy loss at lower energies [45].

Fig.1.11 shows R_{dAu} and R_{AA} of charged hadrons from PHOBOS and STAR experiments in $Au+Au$ collisions at $\sqrt{s_{NN}} = 200$ GeV. The left plot shows R_{dAu} from

peripheral to central events, it is clear that there is no sign of suppression of high- p_T particles. The right plot shows R_{dAu} and R_{AA} in 0 – 20% centrality class. A factor of 5 suppression is observed at high- p_T in $Au+Au$ collisions while an enhancement is observed in $d+Au$ collisions. This enhancement has been attributed to Cronin effect which is a result of initial multiple scattering of the partons prior to hard collision taking place [16, 29]. As we will show in a moment, radiative energy loss describes the shape of R_{AA} .

Fig.1.12 (Left) shows R_{AA} of charged hadrons and neutral pions from data at different energies: SPS at $\sqrt{s_{NN}} = 17.3$ GeV, RHIC at $\sqrt{s_{NN}} = 200$ GeV and the LHC at $\sqrt{s_{NN}} = 2.73$ TeV. The data also spans two orders of magnitude of transverse momentum. While no suppression is observed at SPS energy [43], the suppression at RHIC and the LHC is of the same order and have the same trend at high- p_T the R_{AA} is slowly rising as expected. Also shown are several energy loss calculations from different models. The predicted slope of the R_{AA} varies between the models, this is expected to offer more constraints on the theoretical models, and hopefully improve our understanding of the correct energy loss mechanism at the different ranges of the p_T spectra. See [44] for a discussion of the different models parameters.

Fig.1.12 (Right) shows R_{cp} vs. p_T for charged hadrons calculated for (0–5%)/(60–80%) centralities from the RHIC Beam-Energy-Scan program. The data indicates a possible turn of the QGP energy loss as the center-of-mass collision energy is lowered [45]. This new measurement is expected to serve as another differential measurement which is yet to be confronted by theory calculations.

One can also study energy loss in the medium using di-hadron correlations. Hard particles form jets of particles separated in phase space, the most abundant being back-to-back di-jet events. Correlations between particles in the two jets can reveal a great deal of information on the redistribution of the jets energies in the medium. Fig.1.13 shows measurements of such correlation in $p+p$ and central $d+Au$ and $Au+Au$ data. The typical jets hadronization in vacuum is clear in the $p+p$ measurement where two jets are formed. The same thing is observed in central $d+Au$

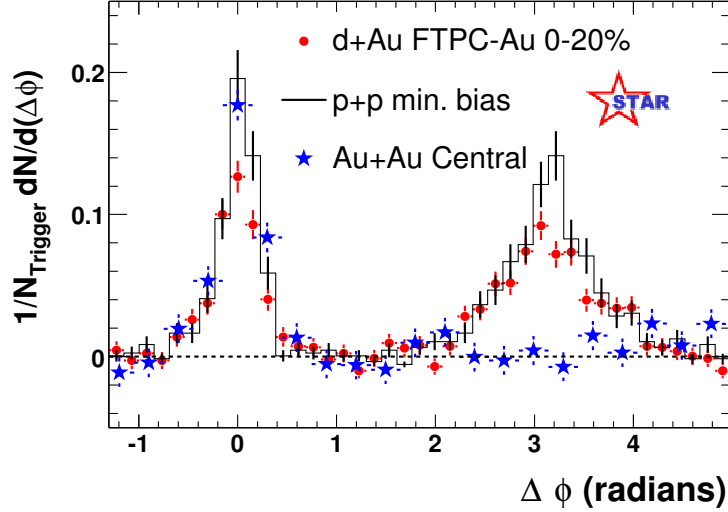


Figure 1.13.: High- p_T di-hadron azimuthal correlations in $p+p$, $d+Au$, and central $Au+Au$ collisions from STAR experiment [42].

collisions where no QGP is expected to form. On the other hand, the $Au+Au$ data clearly shows the complete disappearance of the back jet, the jet energy was transferred to the medium and the correlations were diluted. This is a manifestation of the fact that in such studies one triggers on a high energy jet events, such jets are expected to emanate from the surface of the fireball while the back-jet traverses the full QGP medium.

1.4 Open heavy flavor measurements

1.4.1 Heavy quarks as probes of sQGP

Throughout this work, “heavy quarks” is used in a restricted sense to mean the heavy quarks which freeze-out in open heavy flavor mesons, not the quarkonia states.

To study the structure of any system one needs a probe whose properties (production, interaction) are under experimental and theoretical control. This idea is well known in X-ray tomography; irradiating a material we want to study with a beam of known production source and properties then studying the modification of the ra-

diation to explore the properties of the material. Unfortunately, it is not possible to have an external probe, in the ordinary sense of the word, to study the sQGP. Heavy quarks are used as probes from within the medium and utilized as controlled probes of the bulk matter in HIC. In this section we will discuss what makes heavy quarks such ideal probes to study sQGP.

The large masses of charm and bottom quarks, $m_c \approx 1.3 \text{ GeV}/c^2$ and $m_b \approx 4.2 \text{ GeV}/c^2$ [11], mandate large momenta transfers to produce them and makes their production rates, total and differential cross-sections, amenable to perturbative QCD (pQCD) calculations [46] at sufficiently high p_T ($p_T > m_c$). Fig.1.14 left shows the leading order diagrams of HQ production. Heavy quarks differential cross-sections have been measured by many experiments and have been shown to follow a high p_T power-law distribution characteristic of a pQCD hard-scattering cross-section. Fig.1.14 right demonstrates the agreement between fixed-order next-to-leading logarithm (FONLL) pQCD calculation and measurement of charm differential cross-section by STAR in a wide p_T range [47].

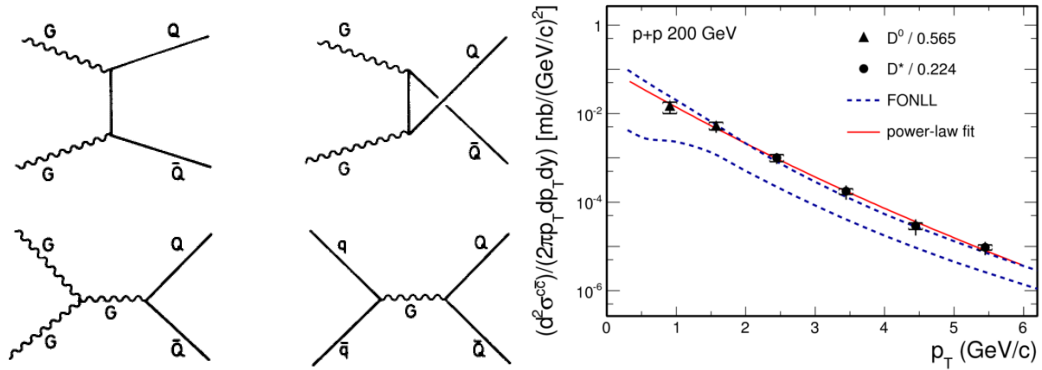


Figure 1.14.: (Left) Leading Order diagrams of heavy quark production cross-section. (Right) Charm differential cross-section measured by STAR [47] clearly demonstrates the power-law high p_T tail. Measurement is consistent with FONLL upper bound [46].

Hard-scattering production of heavy quarks occurs at the very early stages of the heavy-ion collisions, thus, the number of heavy quarks is approximately conserved

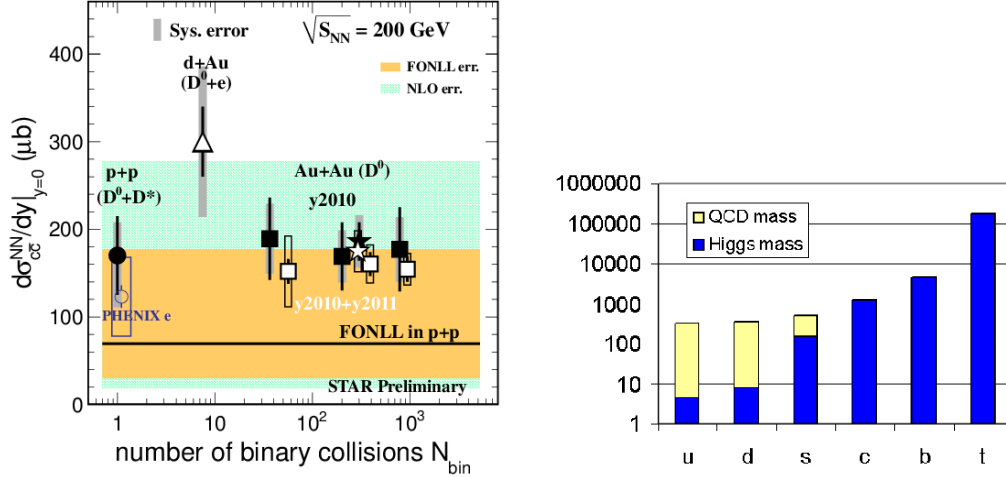


Figure 1.15.: (Left) Charm total cross-section at mid-rapidity in different collision systems normalized to one binary collision. (Right) Contribution of mass generated by electroweak symmetry breaking (current quark mass) is shown in blue, additional contribution of mass generated by spontaneous chiral symmetry breaking in QCD (constituent quark mass) is shown in yellow, figure from [34].

during the sQGP evolution, and the total cross-section in nucleus-nucleus collisions scales with the number of binary collisions (N_{coll}). Fig.1.15 left shows total charm cross-section at mid-rapidity measured in different collision systems and centralities scaled by $1/N_{\text{coll}}$. Possibility of production of charm during the QGP phase (known as thermal charm) has been theoretically investigated and turned out to be insignificant at RHIC energies [48, 49]. One merit of heavy quarks which is important to make this binary scaling possible is that the heavy quark masses are external to QCD, which implies that their masses are, to a good approximation, not modified by their presence in the medium created at RHIC and the LHC. Fig.1.15 shows the contribution of current and constituent quark masses to the total mass of light and heavy flavor quarks [34].

For these merits of heavy quarks they are regarded as clean probes to study the otherwise “thermal” bulk matter. The degree of thermalization of charm quarks

is still under experimental and theoretical study, nevertheless heavy quarks are in general non-thermal probes. Hence, once heavy quarks emerge from the fireball their kinematics carry information about their interaction with the partonic medium during all its stages of the fireball evolution. We seek to extract this information by means of the experimental observables discussed below.

1.4.2 Open heavy flavor reconstruction

Open heavy flavor hadrons have a very short decay length, so in experiments, we identify the decay products of the heavy flavor hadrons and reconstruct them. Ideally, one would want to reconstruct the full kinematics of the parent heavy hadrons, but this is not easy to do; the golden decay channels are hadronic and hadrons make up the absolute majority of the particles in the event debris, which makes it difficult to identify hadrons from heavy flavor. This is, nevertheless, possible to do using topological cuts; with high tracking resolution down to ($\sim 40\mu\text{m}$) one can identify secondary vertices where heavy flavor decay (a typical decay length of $\sim 100\mu\text{m}$) and by this reject most of the background hadrons which emanate from the event vertex itself. This will be possible to do after the installation of STAR secondary vertex tracker, Heavy Flavor Tracker (HFT).

Another way to study heavy flavor is by using their semi-leptonic decay channels. Semi-leptonic decay channels have larger inclusive branching ratios and it is very easy to trigger on high transverse momentum electrons using calorimetry or muons in muon detectors. This gives an advantage to extend the transverse momentum reach of the experimental measurement. However, the disadvantages of using leptons is two folds 1) one cannot fully reconstruct the parent hadron kinematics 2) such measurements are inclusive to electrons or muons from charmed and bottomed hadrons which have a factor of 5 difference in mass and are expected to interact differently with the partonic medium according to most models.

1.4.3 Experimental observables - What have we learned thus far?

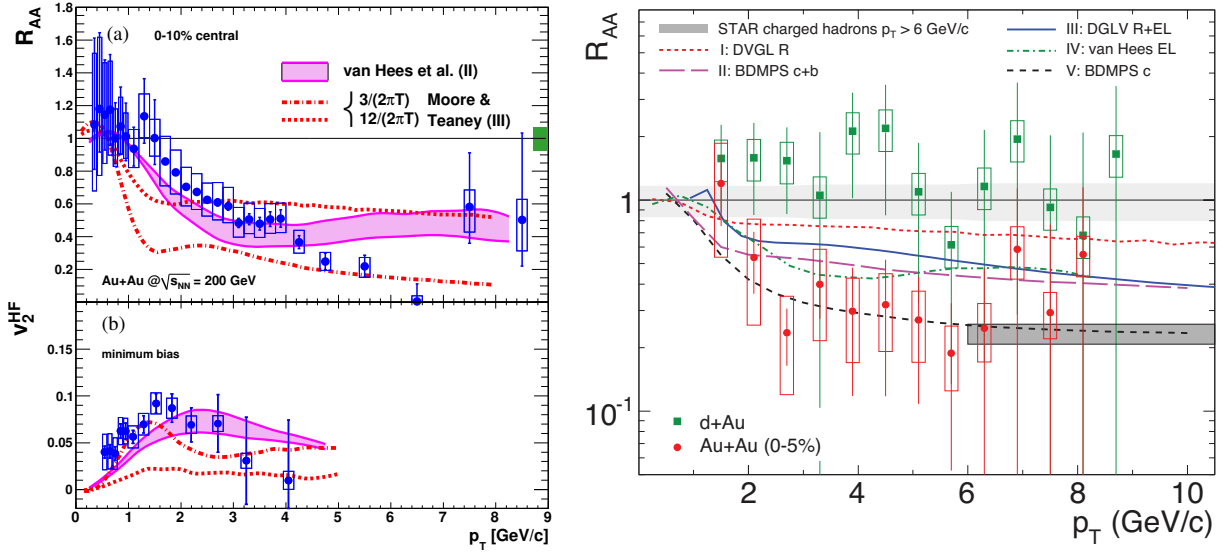


Figure 1.16.: Previous results (Left) PHENIX [50]. (Right) STAR [51]

Heavy quarks nuclear modification factor (R_{AA}) has been proposed as an important measurement to study the flavor dependence of partons energy loss in the medium, and eventually to help in extracting the medium transport, drag and diffusion coefficients, and likely to help in controlling the medium gluon density [52, 53]. Earlier before the first experimental measurement was made, it was expected that heavy quarks lose less energy through soft gluon radiation due to the, by know, well-known dead cone effect; gluon radiation is mass suppressed in a cone below $\theta_o < M/E$ in the gluon phase space with a factor of $(1 + \theta_o^2/\theta^2)^{-1}$ [54]. Which means that there is a mass hierarchy for radiative energy loss ($R_{AA}^b \geq R_{AA}^c \geq R_{AA}^{light}$, bottom, charm and light hadrons, respectively).

Fig.1.16 shows the first heavy quarks measurement at RHIC. Both plots have an R_{AA} measurement of electrons from heavy flavor decay in Au+Au collisions at $\sqrt{s_{NN}} = 200$ GeV, in 0 – 10% and 0 – 5% in PHENIX and STAR experiments, respectively. The R_{AA} shows a factor of 5 suppression, virtually, no different than charged hadrons suppression. It is very different from radiative energy loss calcula-

tions expecting a dead cone effect. DLGV radiative energy loss predictions are shown on top of STAR data in the right plot. It is clear that they miss the measurement by a 2σ effect. This invoked a long series of theoretical investigations and incited many novel ideas to explain the similarity of heavy quarks suppression to light quarks. The different models will be discussed in the discussion chapter at the end of this dissertation.

Measurements of heavy quarks v_2 at low transverse momentum promise to quantify the degree of thermalization of the bulk matter. The inclusive heavy quarks cross-section at low p_T ($p_T < 1.0$ GeV/ c) is dominated by charm production, also, the bottom quark is too heavy to flow with the medium created at RHIC, so if heavy quarks v_2 is finite at low p_T it means that charm has interacted strongly and frequently enough with the medium to significantly thermalize and could cast a verdict on the bulk medium full thermalization. How thermal are charm spectra at low p_T , is a question we still need to answer quantitatively. Furthermore, it will be interesting to find out if charm hadrons follow number-of-constituent-quarks-scaling which was observed for light hadrons [1], which is important to better understand charm hadronization mechanisms at low p_T . Charm flow at this low transverse momenta is also important to understand the origin of charm in charmonium. If charmonium states at low p_T are created by coalescence of flowing charm and anti-charm from the medium, they will carry some of the original flow of these charm quarks. On the other hand, if charmonium is prompt, they are less likely to flow [55].

The origin of light hadrons elliptic flow at high p_T ($p_T > 5.0$ GeV/ c) is believed to be due to path length dependence of partons energy loss in the medium. This is strongly related to the modification of the pQCD power-law spectra at this high transverse momenta. Measuring heavy quarks v_2 at high p_T is an important differential measurement for better discrimination between the different theoretical energy loss models.

2. EXPERIMENTAL SETUP

2.1 Relativistic Heavy Ion Collider

The Relativistic Heavy Ion Collider (RHIC) located at Brookhaven National Laboratory (BNL) in Upton, New York, is a multi-ion species and the world's only polarized-proton high energy collider [56, 57]. Fig.2.1 shows a schematics layout of the RHIC facility, also shown are the accessorial accelerators used to accelerate particles up to RHIC-ring injection energy.

RHIC is a 3.8-km intersection storage ring particle accelerator with six interaction points, two of which are currently instrumented with PHENIX and STAR detectors. RHIC is capable of colliding a variety of ions and beams of different species and beam energies. A demonstration of RHIC capability to collide ions of different species at the same energy per nucleon [57], since its commission in year 2000, RHIC has successfully collided $p+p$, $d+Au$, $Cu+Cu$, $Cu+Au$, $Au+Au$ and $U+U$ at different energies [58]. Particularly important for heavy-ion studies is RHIC's ability to run at different energies, RHIC beam energy scan carried $Au+Au$ collisions at energies ranging from 7.7 GeV to 200 GeV per nucleon-pair, which allowed systematic studies mainly related to the search for a possible QCD critical point. Advancement in accelerator technologies has allowed RHIC to achieve luminosities much larger than its original design, for example the average luminosity achieved during Run year 2011 for $Au+Au$ collisions at $\sqrt{s_{NN}} = 200$ GeV was $30 \times 10^{26} \text{ cm}^{-2}\text{s}^{-1}$ [58] which is 15 times the design value of $2 \times 10^{30} \text{ cm}^{-2}\text{s}^{-1}$ [56].

In addition to heavy-ion studies, RHIC stands as the world only high energy polarized-proton collider allowing experimental studies of the nucleon's structure. See Ref.[59] for a review of the recent results from RHIC spin program and future measurements.

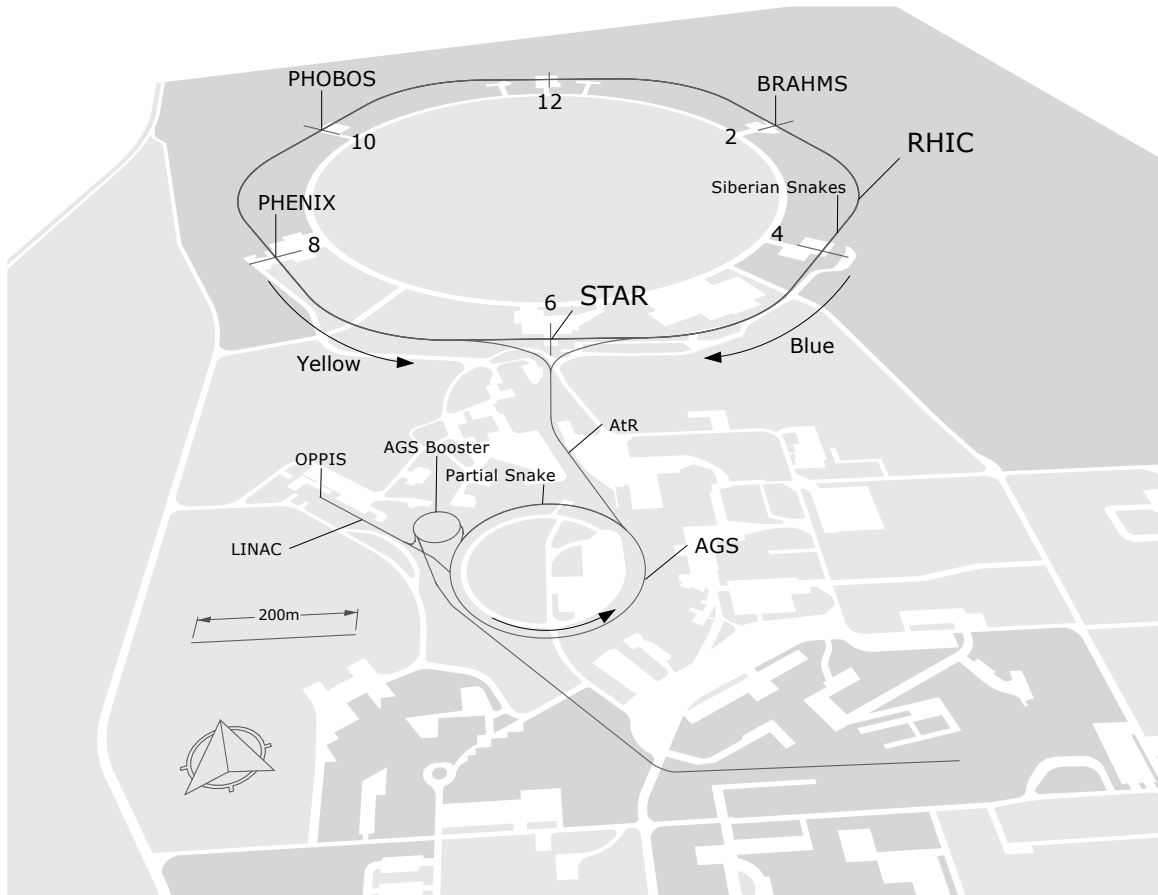


Figure 2.1.: RHIC accelerator complex. Interaction points shown at 2,4,6, 8 and 10 o'clock. BRAHMS and PHOBOS have been decommissioned. PHENIX and STAR are still operating

Construction of a high intensity e^-/e^+ beam facility for electron-ion collisions is being planned, an upgrade known as eRHIC. This will allow to collide 5 – 30 GeV electrons on 50 – 325 GeV polarized protons or up to 130 GeV/u Au ions paving way for experimental studies “focused on the structure and interactions of gluon-dominated matter” [60].

2.2 STAR detector

STAR (Solenoidal Tracker At RHIC) is a multi-species particle detector located at 6 o'clock of RHIC ring [61]. Fig.2.2 shows a 3D cartoon of STAR detector and its different subsystems. STAR detector is mainly designed for event-by-event characterization of the high occupancy environment of heavy-ion collisions. Heavy-ion events can have more than 1000 particles per unit of psuedo-rapidity, Fig.2.3, STAR excellent particle identification capabilities is used to identify these particles over a large solid angle, covering two units of psuedo-rapidity around mid-rapidity and full azimuth.

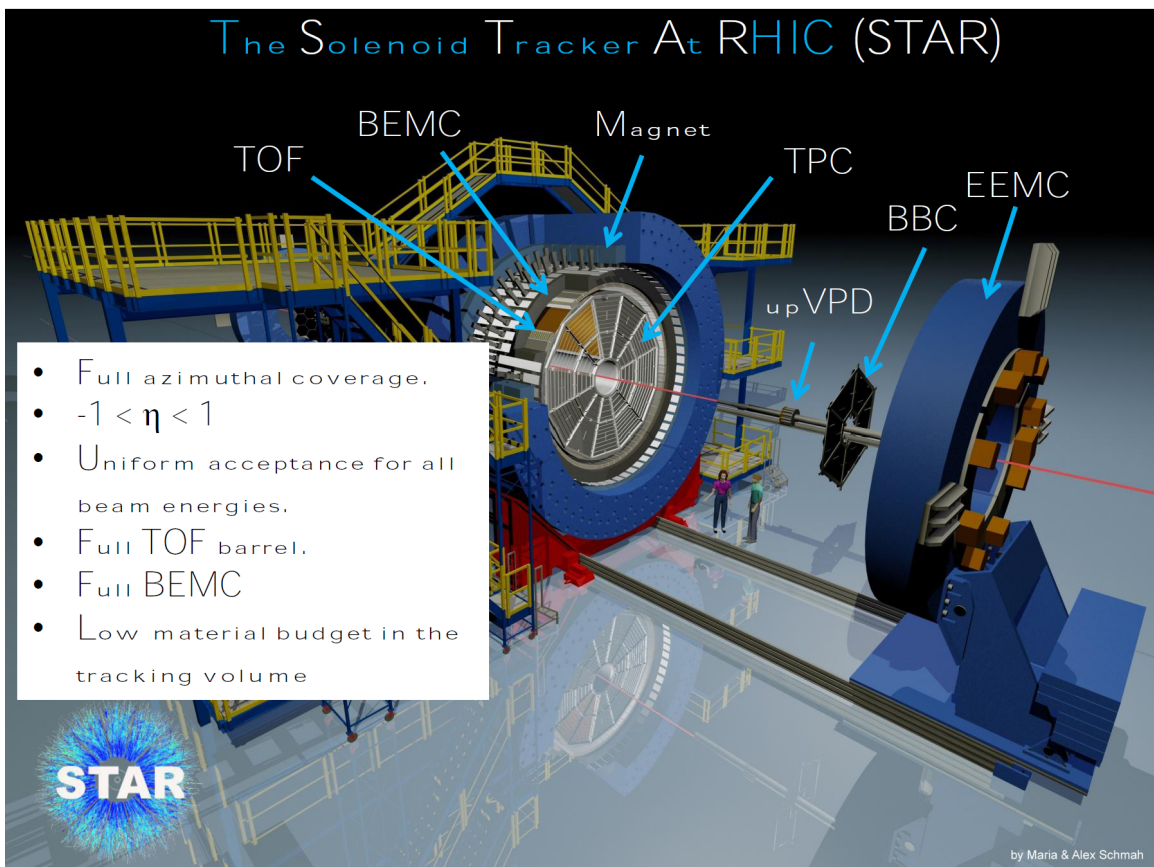


Figure 2.2.: 3D view of the STAR detector.

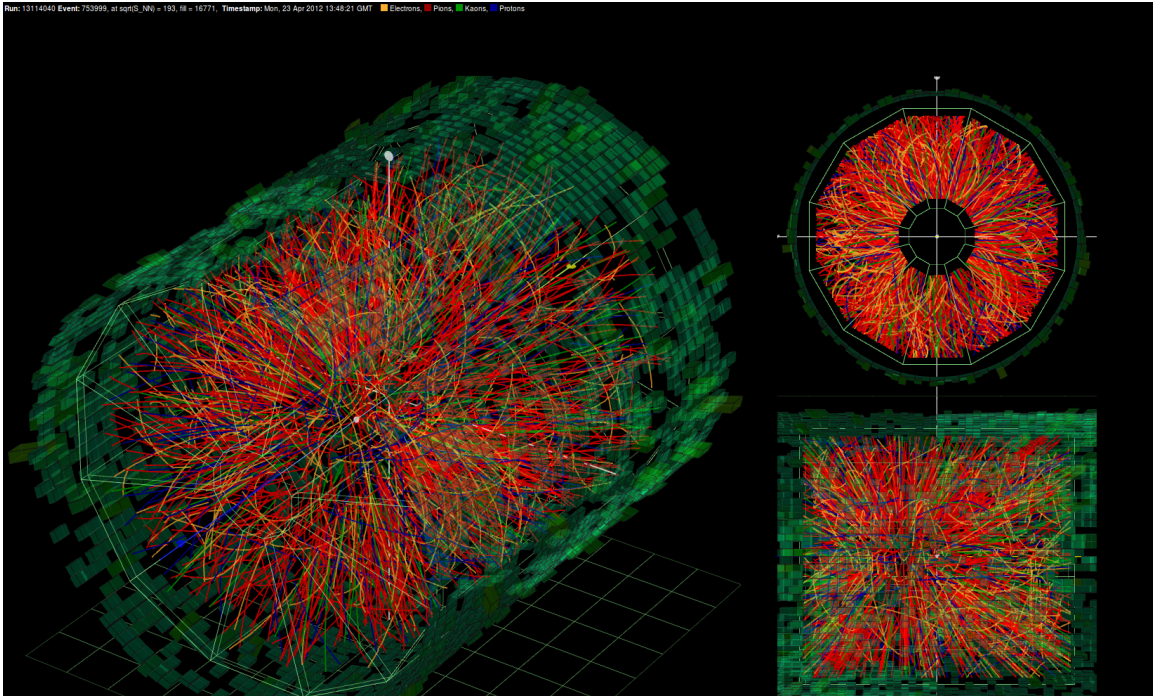


Figure 2.3.: A reconstructed $Au+Au$ high multiplicity event demonstrating STAR high multiplicity operation environment. Tiles in green represent the energy deposited in the BEMC (see text below).

2.2.1 Time Projection Chamber

The Time Projection Chamber (TPC) is the heart of STAR [62]. Fig.2.4 shows a cross-sectional cartoon of the TPC. The TPC barrel is 4 m in diameter and 4.2 m long whose volume is filled with gas. Charged tracks traversing the volume ionize the gas along their paths, released secondary electrons drift in a 135 V/cm electric field to the TPC endcaps to be collected by readout pads. The charge signal measured in the pads together with timing information are used to reconstruct the tracks of the particles.

The TPC Outer Field Cage (OFC) covers two units of pseudo-rapidity in the center-of-mass frame and the full azimuth and it is immersed in a 0.5 Tesla uniform magnetic field along the beam axis. The curvature of the tracks in the magnetic field

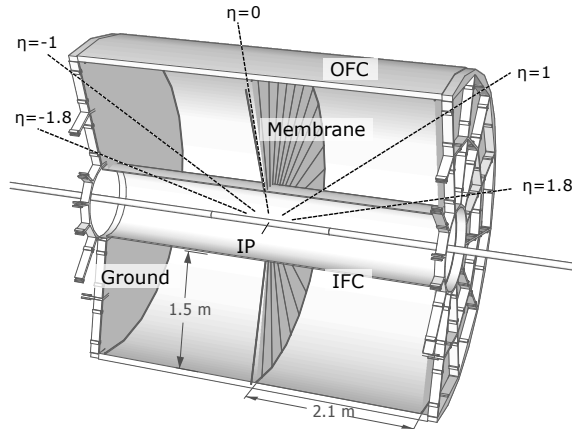


Figure 2.4.: Cross-sectional view of the Time Projection Chamber (TPC).

is used to measure tracks momenta ranging from $150 \text{ MeV}/c$ to $30 \text{ GeV}/c$. In addition to tracking and momenta measurements the TPC is used to identify particle species using their ionization energy loss dE/dx allowing to separate pions and protons up to momentum $p \sim 1.1 \text{ GeV}/c$, and kaons and pions up to $p \sim 0.6 \text{ GeV}/c$.

2.2.2 Barrel Electromagnetic Calorimeter

This analysis relies heavily on STAR Barrel Electromagnetic Calorimeter (BEMC) for $1 - 10 \text{ GeV}$ electrons identification and also for triggering on high- p_T electrons to get an electrons enriched data on top of the MinBias trigger. BEMC sits inside the solenoidal magnet Fig.2.2 and covers the 60m^2 area (just outside the TOF detector, see below), it thus has an acceptance congruent to that of TPC barrel, $|\eta| < 1.0$ and 2π in azimuth [63]. BEMC is a lead-scintillator sampling electromagnetic calorimeter with a total depth of 20 radiation lengths ($20X_0$) at $\eta = 0$. The BEMC is composed of 120 modules which subtends 6° in $\Delta\phi$ and 1.0 unit in $\Delta\eta$, each module is made of 2 rows of 20 $\Delta\Phi \times \Delta\eta = 0.05 \times 0.05$ towers for a total of 4800 towers covering the full BEMC, the towers are projective to the center of the interaction diamond Fig.2.5.

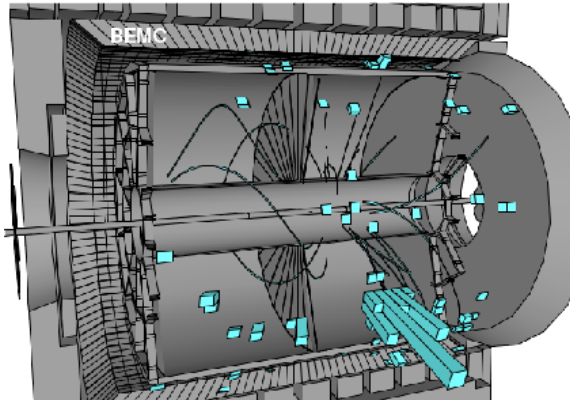


Figure 2.5.: STAR Barrel-Electromagnetic-Calorimeter (BEMC) sitting inside the magnet. The BEMC towers are annotated and their projectivity to the interaction diamond is illustrated by the tilting of the towers. Shown in green are energy deposited by tracks coming from the vertex.

Each module consists of a stack of 20 layers of lead and 21 layers of scintillators with an active depth of 23.5cm (Fig.2.6 left). To provide a finer spatial resolution in the towers a Shower Maximum Detector (BSMD) is implanted at a depth of $\sim 5X_0$, see Fig.2.6. “A two sided aluminum extrusion provides ground channels for two independent planes of proportional wires” [63], each of these layers contain 18000 wires orthogonal to each other to cover the η and ϕ and it thus provides a two-dimensional image of the showers, the SMD is located near the depth of the maximum electromagnetic showers with energies $1-2\text{ GeV}$ as opposed to hadronic showers which peak at one interaction length [63].

2.2.3 Time of Flight detector

The Time-of-Flight detector is made of 120 trays utilizing Multigap Resistive Plate Chambers (MRPCs) technology and covers 2π in azimuth at $|\eta| < 0.9$ surrounding the TPC OFC [64, 65]. The TOF uses event timing information from the forward Vertex-Position-Detector (VPD), see Fig.2.2, together with track hit timing in the

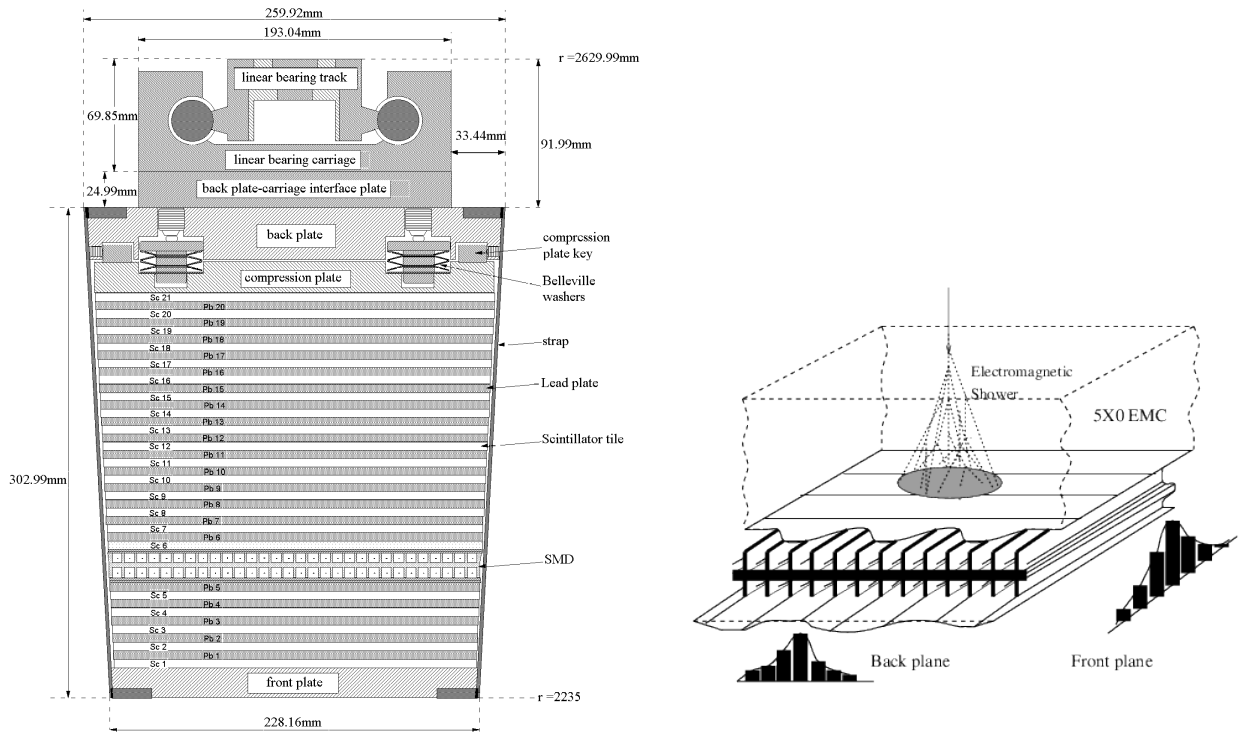


Figure 2.6.: (Left) Side view of BEMC module showing the 20 lead layers and 21 layers of scintillators. Also shown are the two layers of Shower Maximum Detector (BSMD) sitting at a depth of $\sim 5X_0$ from the front face at $\eta = 0$. (Right) A schematic illustration of an electromagnetic shower at the BSMD wire layers which provide a two-dimensional image of the shower. Figures taken from [63].

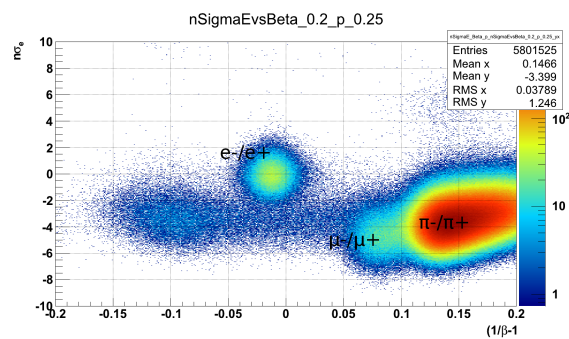


Figure 2.7.: (Color online) Pure electrons sample at very low-momentum can be extracted by applying dE/dx and TOF cuts.

MRPCs to calculate the flight time of the different particles. TOF has a total timing resolution of $\sim 100\text{ps}$. The time of flight information together with the particles momentum from TPC tracking significantly improves STAR particle-identification-capabilities (PID) allowing π :K:p direct PID up to $p \sim 1.7 - 1.9\text{GeV}/c$ and $(\pi+K)$:p up to $p \sim 2.9 - 3.1\text{GeV}/c$ [65]. TOF acceptance for electrons and charged hadrons varies with psuedo-rapidity with an average of $\sim 70\%$ and particle identification $\sim 98\%$ in the relevant kinematical regions. TOF also improves electrons identification at $p_T = 0 - 1.0\text{GeV}/c$ by increasing hadron rejection power achieving $\sim 95\%$ pure electron sample as demonstrated in Fig.2.8.

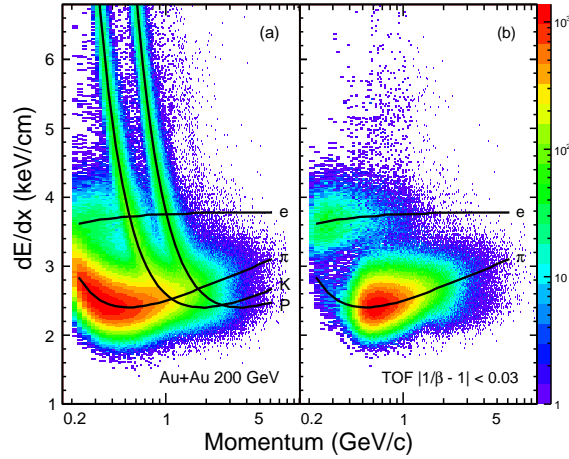


Figure 2.8.: (Color online) Particles dE/dx in TPC vs. momentum from $Au+Au$ events, Bichsel dE/dx functions [66] of the different particles species are also shown. (Left) dE/dx without TOF hadron rejection cut. (Right) Highly electrons-enriched sample after applying TOF hadron rejection cuts.

3. NON-PHOTONIC ELECTRON ANALYSIS

The details of non-photonic electrons (NPE) analysis techniques are discussed in this chapter. Examples from $Au+Au$ at $\sqrt{s_{NN}} = 62.4$ GeV analysis are used for demonstration of analysis techniques. Results from the $Au+Au$ at $\sqrt{s_{NN}} = 62.4$ GeV spectra analysis are presented at the end of the chapter. The analysis of the 62.4 and 39 GeV was divided into spectra analysis and azimuthal anisotropy correlation analysis, the work in this chapter was used for both parts of the analyses. However, the azimuthal anisotropy calculation was done in a collaborative effort with Daniel Kikoła so the details will not be discussed in this dissertation. The results from spectra and azimuthal anisotropy at $\sqrt{s_{NN}} = 200, 62.4$ and 39 GeV will be discussed in chapter 4.

3.1 Analysis Principle

All identified electrons in one event are called *inclusive electrons*, and they are categorized according to their respective sources as following:

I. Photonic electrons

These are electrons from gamma conversion (beam pipe $X/X_0 \sim 0.43\%$, inner field cage $X/X_0 \sim 0.45\%$ and air $X/X_0 \sim 0.17\%$, see Fig.3.1) and Dalitz decays (at event vertex). Mainly:

$$\pi^0 \rightarrow \gamma\gamma \text{ (B.R. 98.8\%).}$$

$$\pi^0 \rightarrow e^+e^-\gamma \text{ (B.R. 1.17\%).}$$

$$\eta \rightarrow \gamma\gamma \text{ (B.R. 39.3\%).}$$

$$\eta \rightarrow e^+e^-\gamma \text{ (B.R. 0.7\%).}$$

Direct gamma.

II. Non-photonic electrons

Electrons from all other sources, which include:

- Heavy-flavor decays. Mainly:
 - $D \rightarrow eX$ (B.R. 16%).
 - $D^0 \rightarrow eX$ (B.R. 6.5%).
 - $B \rightarrow eX$ (B.R. 10%).
 - $\Lambda_c \rightarrow eX$ (B.R. 4.5%).
- Drell-Yan and heavy quarkonia contributions (J/ψ). These contributions can be estimated and may be subtracted later.
- Vector mesons dielectron decays ($\rho, \omega, \phi, \dots$), relevant to low p_T .
- Single electrons background sources, Ke3 ($K^+ \rightarrow \pi^0 e^+ \nu_e$).

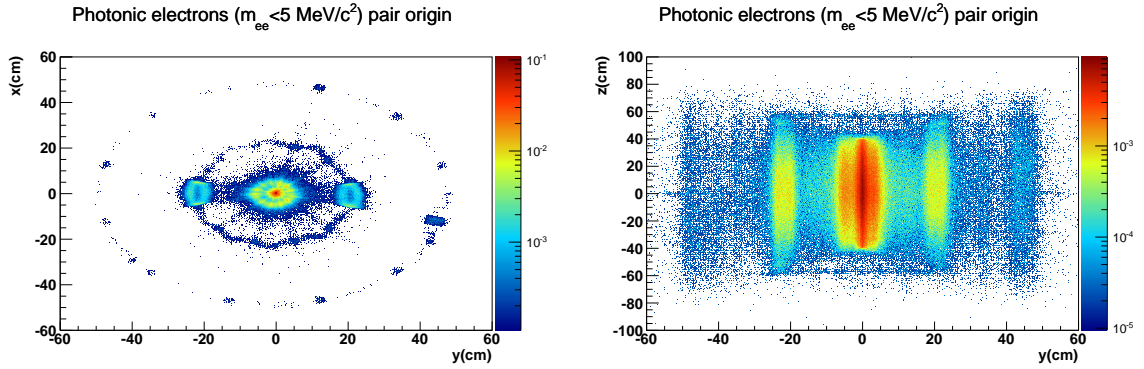


Figure 3.1.: Topology of the photonic electrons origin from $Au+Au$ $\sqrt{s_{NN}} = 62.4$ GeV real data.

In this analysis, we are particularly interested in non-photonic electrons (NPE) which are our signal from heavy hadrons decay. The overwhelming majority of the electrons are background to our analysis and they are dominated by electrons from photonic sources.

In the literature, different methods have been devised to subtract the photonic electrons extract the NPE signals. The conversion method utilized by PHENIX for

years[67] relies on collecting data with and without a material of exactly known radiation length around the interaction region, by studying the increase of the photonic background in events with the material inside they can compare to the data without material and extract the photonic electrons yields in their data. Another subtraction method known as cocktail subtraction method [50] in which invariant yields or cross-sections of photonic electrons sources are measured/estimated and then simulation is utilized to calculate the photonic electrons yields from these sources which are subsequently subtracted from the inclusive electrons yields to extract NPE[67]. For years STAR has relied on directly reconstructing photonic electrons and using simulation to correct their yields [68].

This analysis used the photonic electrons reconstruction method as the main background subtraction method, and also a cocktail simulation study has been carried out and is presented in this chapter. The agreement between the two methods is stunning, demonstrating a very accurate knowledge of STAR material budget in STAR GEANT simulations.

To reconstruct the photonic electrons one reconstructs the invariant mass of the electron-positron pairs in each event and exploits the fact that electron-positron pairs from γ -conversion and Dalitz decays have a very small invariant mass. Fig.3.2 shows examples of invariant-mass plots from our STAR year 2009 analysis [68]. Of course, many of the pairs cannot be reconstructed by this method for many reasons, for example, if one of the pair's tracks has not been reconstructed due to tracking inefficiency or if the partner falls outside of our detector acceptance, the pair will not be reconstructed. Simulations are used to estimate these inefficiencies.

To reconstruct these electron-positron pairs one combines electron tracks with all other opposite-charge electrons (unlike-sign) or with all other same-charge electrons (like-sign) in the same event, invariant mass distributions are plotted in p_T -bins (Fig.3.2). The unlike-sign pairs contain pairs from photonic background (γ -conversion and Dalitz decays), in addition to a combinatorial background. Simulations have shown that the combinatorial background is well reconstructed by the like-sign dis-

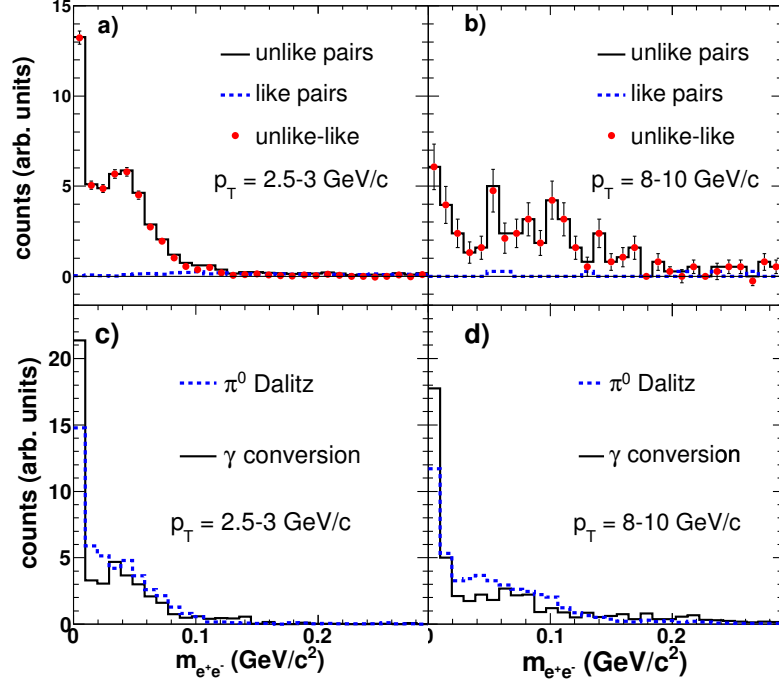


Figure 3.2.: (Color online) Upper panels are electrons pairs invariant mass distributions for electrons at $2.5 \text{ GeV}/c < p_T < 3.0 \text{ GeV}/c$ (a) and at $8.0 \text{ GeV}/c < p_T < 10.0 \text{ GeV}/c$ (b). Solid and dashed lines are unlike-sign and like-sign pairs, respectively. Closed circles are the difference of unlike and like. Lower panels show simulated invariant mass distributions with electrons at $2.5 \text{ GeV}/c < p_T < 3.0 \text{ GeV}/c$ (c) and at $8.0 \text{ GeV}/c < p_T < 10.0 \text{ GeV}/c$ (d). Solid and dashed lines are results from γ conversions and π^0 Dalitz decay.

tribution, so subtracting like-sign from unlike-sign (unlike-minus-like) leaves us with the photonic electrons contribution. Fig.3.2 shows two features in the invariant mass distributions, the peak at $m_{ee} \sim 0 \text{ GeV}/c^2$ and a broad shoulder structure peaking around $m_{ee} \sim 0.5 \text{ GeV}/c^2$ with a tail. The shoulder is due to the finite tracking resolution causing some pairs to have a larger reconstructed opening angle in the transverse-plane. Almost all reconstructible photonic pairs are contained within $m_{ee} \leq 0.24 \text{ GeV}/c^2$.

To obtain the invariant yield of non-photonic electrons we statistically subtracts the contribution of photonic electrons from the inclusive electrons according to the master equation:

$$N_{npe} = N_{inc} * \epsilon_{purity} - \frac{N_{pho}}{\epsilon_{pho}} \quad (3.1)$$

where ϵ_{purity} is the purity of the inclusive electrons calculated from real data, ϵ_{pho} is the acceptance of photonic electrons pairs calculated from simulation. N_{npe} , N_{inc} and N_{pho} are non-photonic, inclusive and photonic electrons yields, respectively. Details of electrons identification, purity and efficiencies are discussed later in this chapter.

3.2 Datasets and quality assurance

During RHIC 2010 run, STAR has collected a large amount of minimum-bias, central and high p_T trigger data in Au+Au collisions at $\sqrt{s_{NN}} = 39, 62.4$ and 200 GeV with detector configuration for minimum photonic conversion background. In this dissertation we report on non-photonic electrons measurements results from all of these dataset. However, in this chapter we only discuss the techniques and use examples from $Au+Au \sqrt{s_{NN}} = 62.4$ GeV. Datasets selection and event cuts are summarized in Table 3.1.

In addition to these cuts, Time-of-Flight detector information and a correct magnetic field are required for every event. Fig.3.3 shows the vertex distributions of minimum-bias $Au+Au$ events at $\sqrt{s_{NN}} = 62.4$ GeV. These distributions are utilized to determine the event vertex selection cuts. Running at high luminosities comes with the disadvantage of having a high number of pile-up events, pile-up events are those which happen while the TPC gating grid is open but they did not fire the event trigger themselves. The TPC is a very slow detector (electrons drift velocity in the TPC gas is $5.5 \text{ cm}/\mu\text{s}$) so it is the normal to find many vertices in the same event. To reject these pile-up events and discern the true vertex of the event which fired the trigger the Vertex-Position-Detector (VPD) with a timing resolution of $\sim 100\text{ps}$ is utilized. Fig.3.3 top right shows the distribution of V_z versus V_{vpd} .

Table 3.1: Datasets and event selection cuts for $Au+Au$ at $\sqrt{s_{NN}} = 39$ and 62.4 GeV.

	62.4 GeV	39 GeV
production	P10ik	P10ik
trgsetupname	AuAu62_production	AuAu39_production
streams	st_physics, st_ht	st_physics, st_ht
offline trigger IDs	MB 270011	MB 280001
	MB 270021	HT11 280501
	HT11 270511	
	HT11 270521	
	HT15 270503	
nEvents		
$ V_z \leq$	40 cm	40 cm
$ V_z - V_{vpd} \leq$	4 cm	no cut
$V_r = \sqrt{V_x^2 + V_y^2} \leq$	1 cm	1 cm
refMult \geq	8	8

Once the dataset is determined one needs to perform her/his own quality assurance to reject events or runs which are not of the desired quality. In addition to relying on the official STAR QA done by Alex Schmah and Hiroshi Masui, details in STAR protected slides [69], a few extra QA studies specific to electrons studies are done here.

The aim of the QA study is to select events with uniform performance throughout the run, especially those which can dramatically affect electrons yields and detector efficiencies over time.

Fig.3.4 shows the distribution of the average number of events collected in every run versus runID. After projection to the y-axis a cut of a 2σ is placed to reject bad runs which are shown in red.

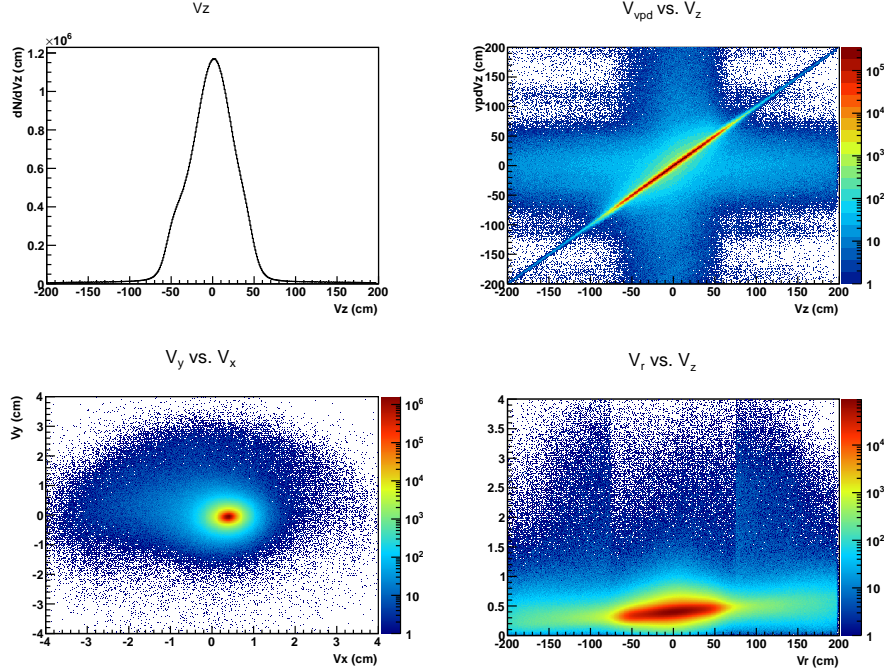


Figure 3.3.: (Color online) Event vertex distributions in $Au+Au$ at $\sqrt{s_{NN}} = 62.4$ GeV. (Top left) Distribution of events vertex Z-coordinate with respect to STAR center, this vertex is from the TPC tracking and vertex finding algorithms. (Top right) Z-vertex from tracking (V_z) versus Z-vertex from VPD clearly peaking at the center of the TPC, distribution is used to place a sensible $|V_z - V_{vpz}|$ cut for events selection. (Bottom) Distribution of events vertices in the xy-plane.

Figure 3.5 shows the average number of tracks per event versus runID after rejecting bad runs from the previous QA. The distribution is rather good for this data.

One also needs to see if the inclusive electron yield fluctuates during the run. Firstly, one needs to study the electrons identification cuts which we leave to Section 3.4.1. It is enough mention that to identify electrons at low p_T (≤ 1.0 GeV/ c) we use TOF information for hadron rejection, and BEMC information for high p_T . Fig.3.6 shows the event-average number of electrons at low- p_T , the circle in red shows the rejected runs. Figure 3.7 shows the event-average number of electrons at high p_T .

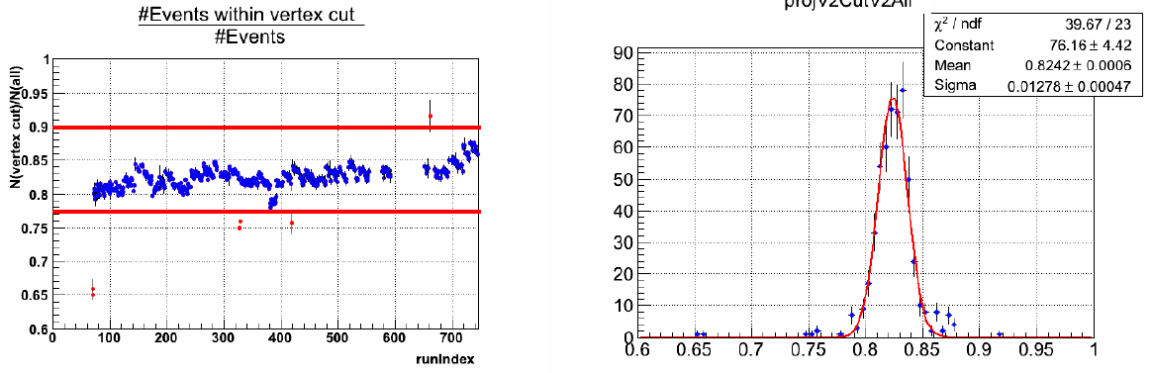


Figure 3.4.: (Color online) $\sqrt{s_{NN}} = 62.4$ GeV data. (Left) Number of events which pass the vertex cuts divided by the total number of collected events in one run versus the runID, approximately $3\text{-}\sigma$ cut is shown in red, blue points pass the cut red points are rejected runs. (Right) projection of the left plot on the y-axis.

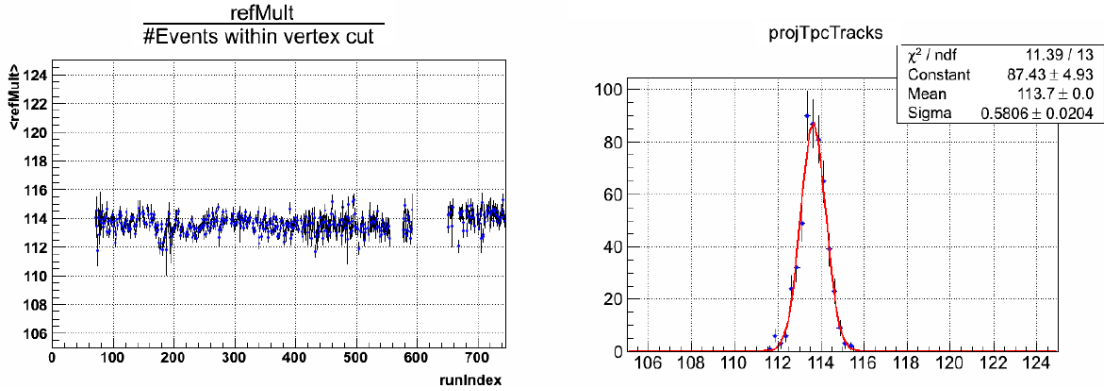


Figure 3.5.: (Color online) $\sqrt{s_{NN}} = 62.4$ GeV data. Left panel is average number of tracks (see definition of refMult) per event versus runID. Left panel is the y-axis projection of the left plot.

Centrality selection has been based on charged particle multiplicity at mid-rapidity $|\eta| < 0.5$. Table.3.2 shows N_{bin} , N_{part} and impact parameter from Monte-Carlo Glauber simulations [31].

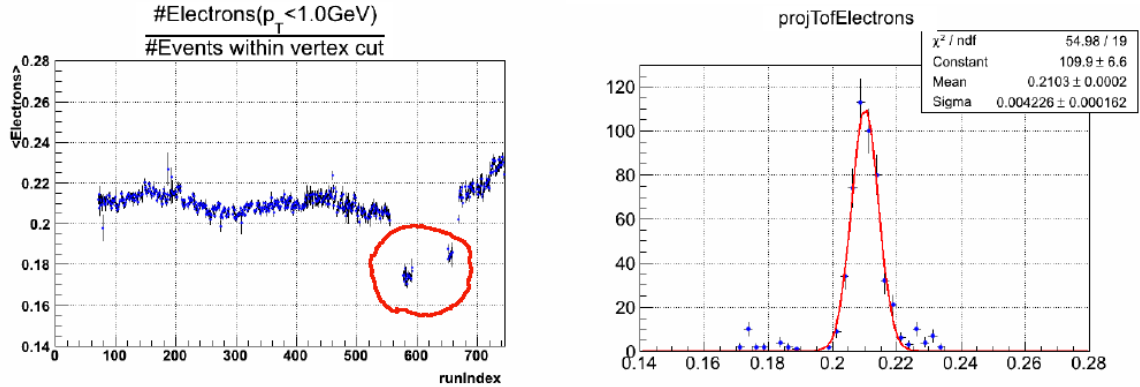


Figure 3.6.: (Color online) $\sqrt{s_{NN}} = 62.4$ GeV data. Left panel is average number of electrons identified using TOF (see text for details) per event versus runID. Left panel is the y-axis projection of the left plot.

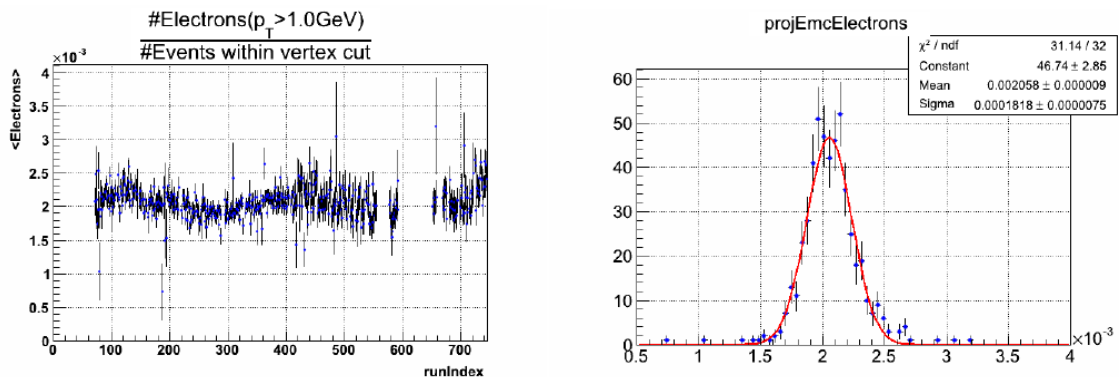


Figure 3.7.: (Color online) $\sqrt{s_{NN}} = 62.4$ GeV data. Left panel is average number of electrons identified using BEMC (see text for details) per event versus runID. Left panel is the y-axis projection of the left plot.

3.3 Trigger combination

In this analysis, Minimum Bias (MB) trigger data is used for low- p_T (≤ 1.0) electrons, while higher p_T electrons are extracted from high-tower (HT) triggered data; STAR BEMC is used to get a highly enriched high- p_T electrons sample. HT events are collected by requiring a certain threshold on the energy deposited in one

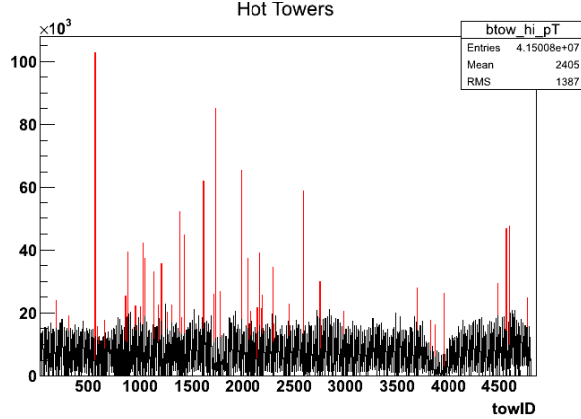


Figure 3.8.: (Color online) $\sqrt{s_{NN}} = 62.4$ GeV data. Hot towers during this run. Plotted is the average number of electrons in BTOW towers. Hot towers are shown in red.

Table 3.2: N_{bin} , N_{part} and impact parameter for different centralities in $Au+Au$ at $\sqrt{s_{NN}} = 62.4$ GeV from Monte-Carlo Glauber simulations.

Centrality	N_{bin}	N_{part}	b (fm)
0 – 80%	253 ± 20	123 ± 8	8.88 ± 0.34
0 – 60%	332 ± 23	157 ± 9	7.66 ± 0.27
0 – 10%	813 ± 26	320 ± 4	3.17 ± 0.13
10 – 20%	519 ± 25	232 ± 8	5.66 ± 0.22
20 – 40%	258 ± 27	139 ± 10	8.03 ± 0.29
40 – 60%	82 ± 18	60 ± 10	10.44 ± 0.38

BEMC tower. HT11, HT15, HT15, HT18 and HT25 are online triggers which require transverse energy (E_T) thresholds of ~ 2.6 GeV, ~ 3.5 GeV, ~ 4.2 GeV and ~ 5.9 GeV, respectively. HT11 and HT15 data are used for 62.4 analysis, while only HT11 data is available for 39 GeV. All HT triggers were used for the 200 GeV analysis.

Because of the finite bandwidth of the Data Acquisition (DAQ) system, the Min-Bias trigger(s) and the high cross-section HT triggers are pre-scaled, i.e. not all

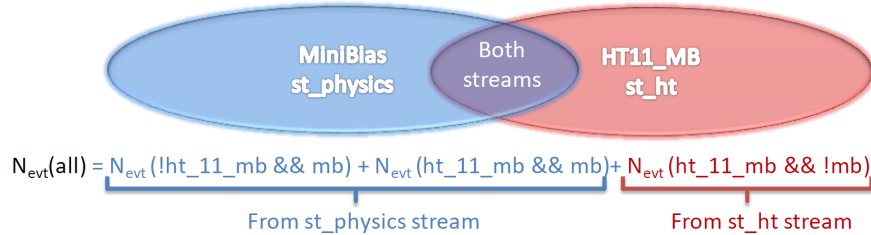


Figure 3.9.: Venn diagram of triggered data in different streams.

events which fire these triggers are collected and random sampling is implemented to select such triggers. While some of the pre-scaling factors are fixed, the others are dynamic, which means that they change according to available bandwidth. In the analysis, one needs to account for these pre-scaling factors to normalize the measured invariant-yield and/or cross-section to the correct number of events and luminosities. The technique of trigger combination is discussed below, but before that a minor technical detail should be noted. To ease the analysis and data allocation the data from MinBias and HT triggers typically go into different file streams (st_physics and st_ht streams), but because the HT triggers are built on-top of the MinBias triggers (HT trigger the event to fire the MinBias trigger) copies of many events end-up in both data streams, see Fig.3.9. One needs to be careful to select events which are tagged with MB&&HT from one stream only to avoid double counting, in this analysis we select these events from st_physics stream (Fig.3.9).

As mentioned above, for the spectra analysis it is crucial to correctly account for the pre-scaling of the different triggers and to ensure a correct normalization for the physics collected in both triggers. From HT triggered events we only use electrons which deposit energy in the BEMC greater equal to or greater than the HT trigger threshold. For example, from HT15 events we use only electrons which have an ADC value ≥ 15 (corresponding to $E_T \sim 3.5$ GeV). All electrons from MinBias triggers are used. Fig.3.10 shows an example of the implemented trigger algorithm for the simple case of only HT11 trigger, note that the algorithm correctly accounts for the events

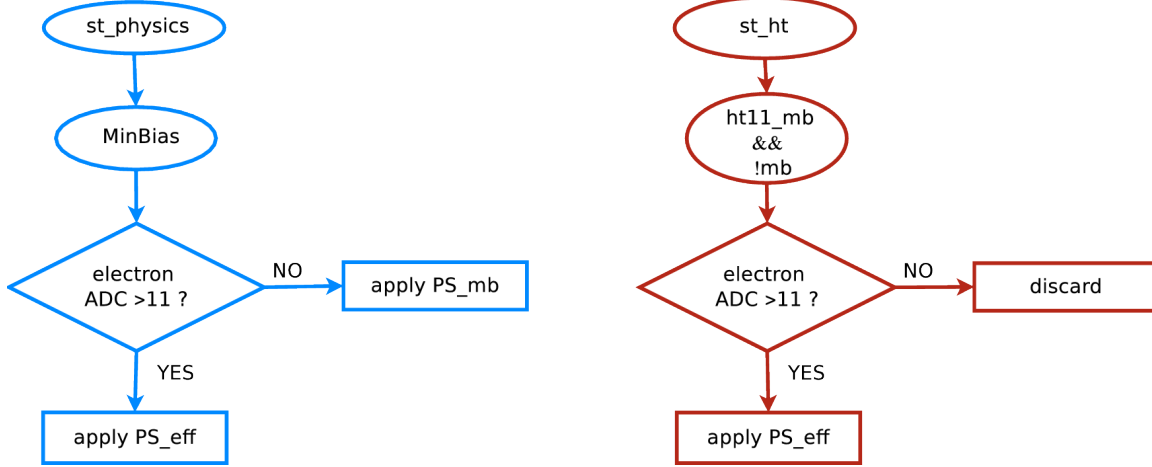


Figure 3.10.: An example of the trigger combination algorithm with one HT trigger.

selection from different data-streams. The effective pre-scaling factors PS_{eff} applied for the case of HT11 and HT15 triggers are:

$$PS_{eff}^{11} = \frac{PS_{mb} \times PS_{11}}{PS_{mb} + PS_{11} - 1} \quad (3.2)$$

$$PS_{eff}^{15} = \frac{PS_{mb} \times PS_{11} \times PS_{15}}{PS_{mb} \times PS_{11} + PS_{mb} \times PS_{15} + PS_{11} \times PS_{15} - PS_{mb} - PS_{11} - PS_{15} + 1} \quad (3.3)$$

where PS_{mb}, PS_{11} and PS_{15} are the prescale factors which vary by runID. So in the case of the 62.4 GeV data, where HT11 and HT15 data is used, for electrons from HT11 triggers which have $11 \leq \text{ADC} < 15$ the effective prescale PS_{eff}^{11} from Eqn.3.2 is applied, and Eqn.3.3 is applied for electrons with $\text{ADC} \geq 15$.

Finally, to check that the trigger combination algorithm works as expected one wants to check that the normalization is correct. To do this the inclusive and photonic electron spectra from the trigger combination algorithm are compared directly to the respective spectra from the MinBias trigger which received no pre-scaling corrections. Fig.3.11 shows this comparison for the 62.4 GeV data.

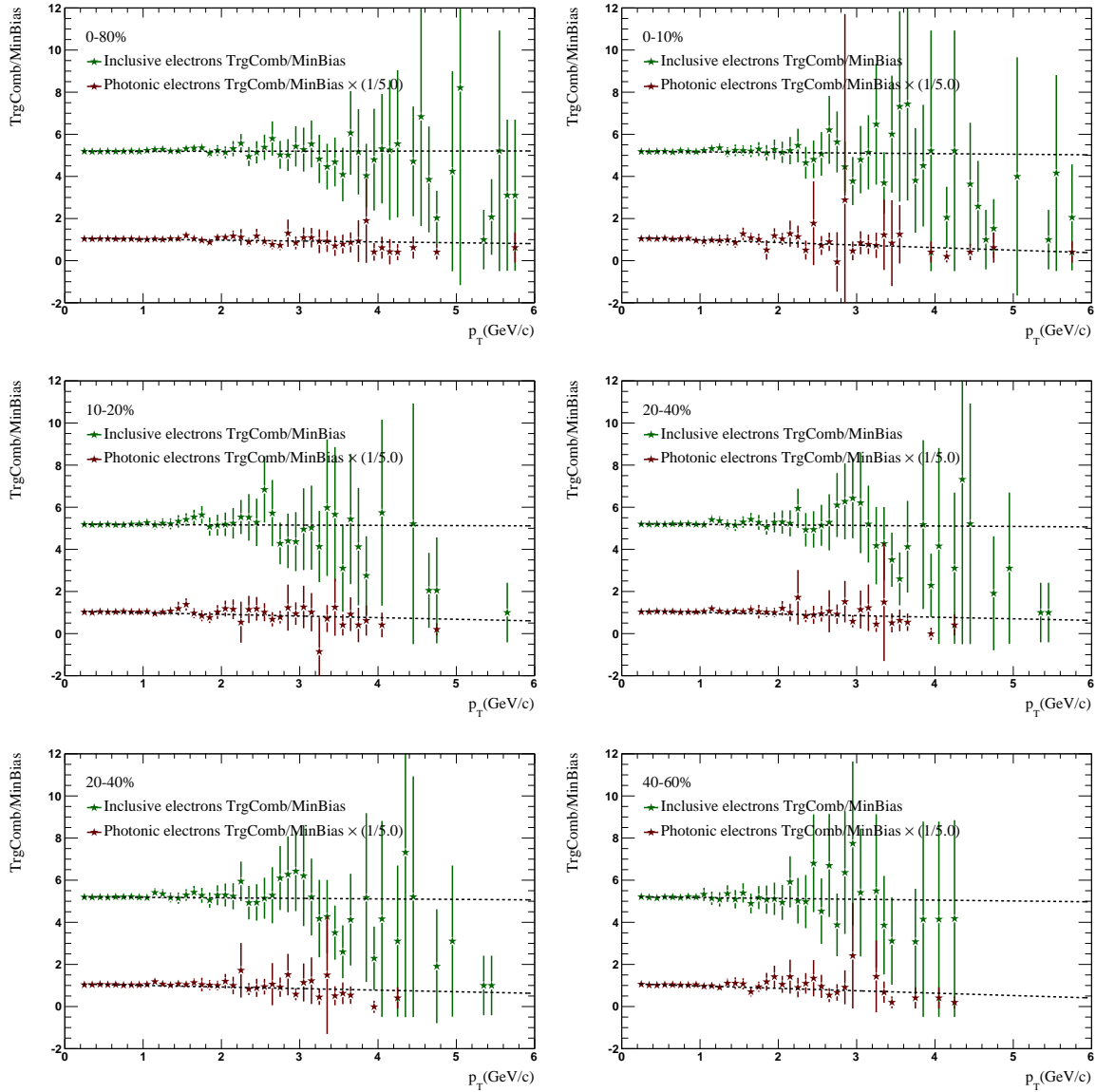


Figure 3.11.: Ratios of trigger combined inc. and pho. spectra to spectra obtained from MinBias data.

3.4 Electron identification and efficiencies

3.4.1 Electron identification cuts

For any study of electrons from semi-leptonic decays of heavy flavor hadrons, so called non-photonic electrons (NPE), one carry an electron identification study before

proceeding to calculate different quantities of interest such-as cross-sections, invariant yields, azimuthal anisotropy or hadron correlations.

Electron cross-section is very small compared to the hadronic cross-sections, thus finding pure electron tracks with high efficiency is a tricky task. The identification of electrons is done by combining information from different detectors depending on different electrons kinematical regions.

Table 3.3: Track quality cuts

nFit (number of TPC points used for tracking)	> 20
nFit/nMax (nMax is maximum number of points possible for a track)	> 0.52
ndEdx	> 15
gDCA (Distance-of-closest-approach of the global track to the event vertex)	< 1.5 cm
R(1st TPC point)	< 73 cm
$ \eta $ for $p_T > 0.5\text{GeV}/c$	< 0.5
η for $p_T < 0.5\text{GeV}/c$	> 0 && < 0.5

First one needs to select tracks with high reconstruction efficiency, Table3.3 shows the track quality cuts implemented in this analysis. Tracks within $|\eta| < 0.5$ are selected to assure uniform acceptance for all tracks and photonic electrons pairs. During RHIC run year 2010 one of the TPC sectors was masked off for $\eta < 0$ (see Fig.3.12) which is problematic for photonic electrons pair reconstruction for low- p_T because the opening angle for low- p_T electron-positron pairs is large and such low- p_T tracks have a large curvature in the 0.5 Tesla magnetic field and typically cross several TPC pads, the masked sector significantly affects the pair reconstruction efficiency. For this reason for $p_T < 0.5 \text{ GeV}/c$ only $\eta > 0$ tracks are used in this analysis.

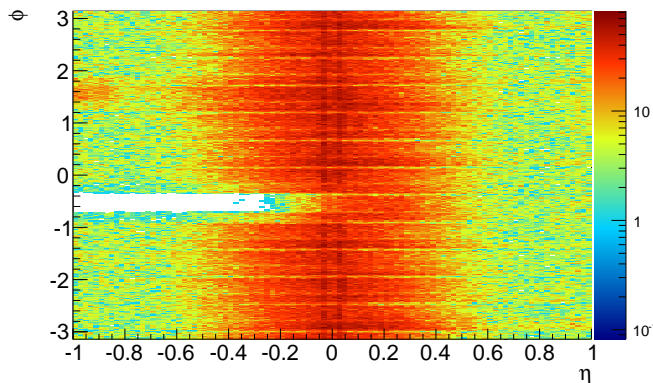


Figure 3.12.: (Color online) ϕ vs. η distribution from $Au+Au$ at $\sqrt{s_{NN}} = 62.4$ GeV showing the masked TPC sector in RHIC run year 2010.

nFit and nFit/nMax are required to ensure high tracking efficiency, tracks within $|\eta| < 0.5$ typically cross all TPC pad and should have a maximum of 45 TPC hit points. nFit is the number of these points which is used for fitting the track, nMax is the maximum number of points possible for that track. ndEdx is the number of points used for TPC ionization energy loss calculation.

gDCA is a cut on the distance-of-closest-approach of the track to the event vertex. The TPC pointing resolution is in the order of millimeters. By requiring the TPC tracks to be 1.5 cm away from the vertex ensures maximum efficiency for electrons from heavy flavor hadron decays which have a very short lifetime (typical $c\tau$ is a few hundred micrometers). These are called *global tracks*. Once a cut on the distance-of-closest-approach to vertex is placed fitting the track is re-done to include the vertex in the fit which increases the electron momentum resolution, such tracks are called *primary tracks*.

A cut is placed on the location of the first TPC point used in the fit. The purpose of such a cut is to suppress photonic electrons from the TPC inner field cage and gas contribution to the inclusive electrons.

Table 3.4: Pairs cuts

m_{ee} (< 0.15 for $p_T < 5.0$) or (< 0.2 for $5 < p_T < 7$) or (< 0.24 for $p_T > 7.0$)
Distance of Closest Approach of pair helices $DCA(\text{pair}) < 1.0\text{cm}$
partner dE/dx $3.0 \times 10^{-6} \text{ keV/cm} < dE/dx < 5.0 \times 10^{-6} \text{ keV/cm}$

The next step after the single tracks cuts are set is to do the pairing to extract the photonic electrons pairs. The pairing is done by matching every single global track which has a primary partner with all the global tracks in the same event. Pairing in this case means swimming the tracks helices and calculating their distance-of-closest-approach, then calculating the invariant mass formed by the momenta of these helices at their point of closest approach, assuming they have electron mass for their Lorentz vector. The only cuts applied on the partner global track are tracking cuts and a 100% electrons efficiency cut on the dE/dx , see Table 3.4. No further cuts are applied on the partner to increase the photonic electrons reconstruction efficiency.

For the electron identification cut (eID) different detectors are utilized for different electrons kinematical regions. Table 3.5 shows the eID cuts which were applied in this analysis. For $p_T < 1.0 \text{ GeV}/c$ TOF is used to reject hadrons and $\sim 50\%$ efficiency dE/dx cut is used to select electrons. TOF is also used to reject protons for tracks within $1.0 < p_T \leq 1.5$, this cut is 100% efficient for selecting electrons. At high- $p_T > 1.0 \text{ GeV}/c$, BEMC is used to reject hadrons. The BEMC association windows are listed in Table 3.5, other than the association window cuts a cut on the ratio of track momentum to the energy it deposits in one EMC tower is applied. Electrons typically deposit $\sim 95\%$ in a single EMC tower (more precisely the electromagnetic shower is contained in a cylinder of twice the Moliere radius [63]), and because of their negligible mass their p/E_0 peaks around 1.0. Hadrons on the other hand have a much larger transverse spread, and they are also less likely to fire the SMD which is placed at the peak of the electromagnetic shower.

A note is in order here, instead of using the dE/dx of the tracks directly to select electrons the normalized ionization energy loss [70] is used, defined as

$$n\sigma_e = \frac{\log((dE/dx)/B_e)}{\sigma_e}$$

where B_e is the expected mean dE/dx of electrons from electron Bichsel function [66], and σ_e is the measured TPC resolution of $\log((dE/dx)/B_e)$.

Table 3.5: Electrons Identification cuts

	$p_T \leq 1.0$	$1.0 < p_T \leq 1.5$	$p_T > 1.5$
TPC (dE/dx)	$0 < n\sigma_e < 2.0$	$0 < n\sigma_e < 3.0$	
TOF	$ y_{\text{Local}} < 1.8 \text{ cm}$ $-0.03 < (1 - 1/\beta) < 0.02$	$ y_{\text{Local}} < 1.8 \text{ cm}$ $-0.1 < (1 - 1/\beta) < 0.1$	no cut
BEMC	N/A	$0.3 < p/E_0 < 2.0$ $ \text{btow}\Delta\phi < 0.05 \ \&\& \ \text{btow}\Delta z < 10 \text{ cm}$ $ \text{bsmd}(\eta)\Delta\phi < 0.06 \ \&\& \ \text{btow}(\eta)\Delta z < 3 \text{ cm}$ $ \text{bsmd}(\phi)\Delta\phi < 0.015 \ \&\& \ \text{btow}(\phi)\Delta z < 16 \text{ cm}$ SMD Multiplicity cut: $n\text{SMD}(\eta) > 1 \ \&\& \ n\text{SMD}(\phi) > 1$	

It is clear from the NPE extraction method we use, equation 3.1, that the photonic electrons can not tolerate any hadron contamination. Purity of the photonic electrons sample is essential to this analysis. Hence, we use photonic electrons to tune our electron identification cuts (eID). The purity of the photonic electrons is ensured by tuning the eID cuts to make the like-sign pair invariant mass distribution exactly match the combinatorial background in the unlike-sign invariant mass distribution. This physically makes sense; the like sign background is purely combinatorial and there is no physical signal in there, and also simulations are used to confirm this otherwise intuitive technique. Fig.3.13-3.15. Another purity control measure is to look at the $n\sigma_e$ of the partner tracks. Since no eID cuts are placed on the partner tracks their $n\sigma_e$ serves as a good check on the pair purity quality; if the pairs are truly formed by electrons the partner $n\sigma_e$ should be that of electrons automatically. $n\sigma_e$ distributions are shown in the same plots.

To ensure the purity of photonic electrons pairs the invariant mass and partner $n\sigma_e$ distributions are studied in fine p_T bins, Fig.3.13, and also in centrality bins, Fig.3.14 and Fig.3.15. It is important to emphasize here the importance of this study in fine p_T bins especially at low- p_T because the photonic electrons statistics are dominated by low- p_T tracks who generally have higher purity even with loose eID cuts. So looking at the invariant mass plot in a large p_T bin can deceptively give the impression that the sample is pure while it is in fact dominated by high statistics low- p_T electrons.

To select BEMC association windows clusters are formed by combining the towers with highest energy with three other adjacent towers to form one cluster. In such clusters of four towers the showers are likely to be contained within a single cluster with $\sim 100\%$ efficiency [71, 72]. After clusters are formed, the selected TPC tracks are projected on the BEMC geometry and the tracks are associated with the nearest BEMC point, the cluster BEMC point is determined by taking energy-weighted mean of the towers in the cluster [72]. After associating tracks with BEMC points cuts on the distance between track projection to the BEMC and the associated BTOW and BSMD points are applied.

To choose appropriate BEMC association windows one starts with generic cuts for the eID including BEMC association windows cuts then starts looking at the BEMC-point-to-track distance distributions in all possible windows. The BTOW points have distance along the ϕ and z directions. Each of the BSMD layers has its own ϕ and z coordinates. By applying all eID cuts except the cut one is trying to tune, one can select the appropriate association window cuts. Fig.3.16-Fig.3.18 show the application of this technique to the $Au+Au \sqrt{s_{NN}} = 62.4$ GeV data. Note that the association window cuts are very loose to allow for maximum efficiency possible.

The last BEMC eID cut to apply is the track momentum to the energy of the highest tower (p/E_0) which we discussed above. Fig.3.19 shows the p/E_0 distributions. The clearly peak near 1.0 with a slight shift to higher values because the energy of the tower with highest energy in the cluster is used instead of the total energy in the cluster, this is due to the fact that some of the electromagnetic showers spread to more than one tower. However, the p/E_0 shown clearly shows that most of the shower energy is contained within one tower.

Finally for the eID cuts, Fig.3.20 and 3.21 show the $n\sigma_e$ distributions of photonic electrons in p_T - and centrality- bins, respectively.

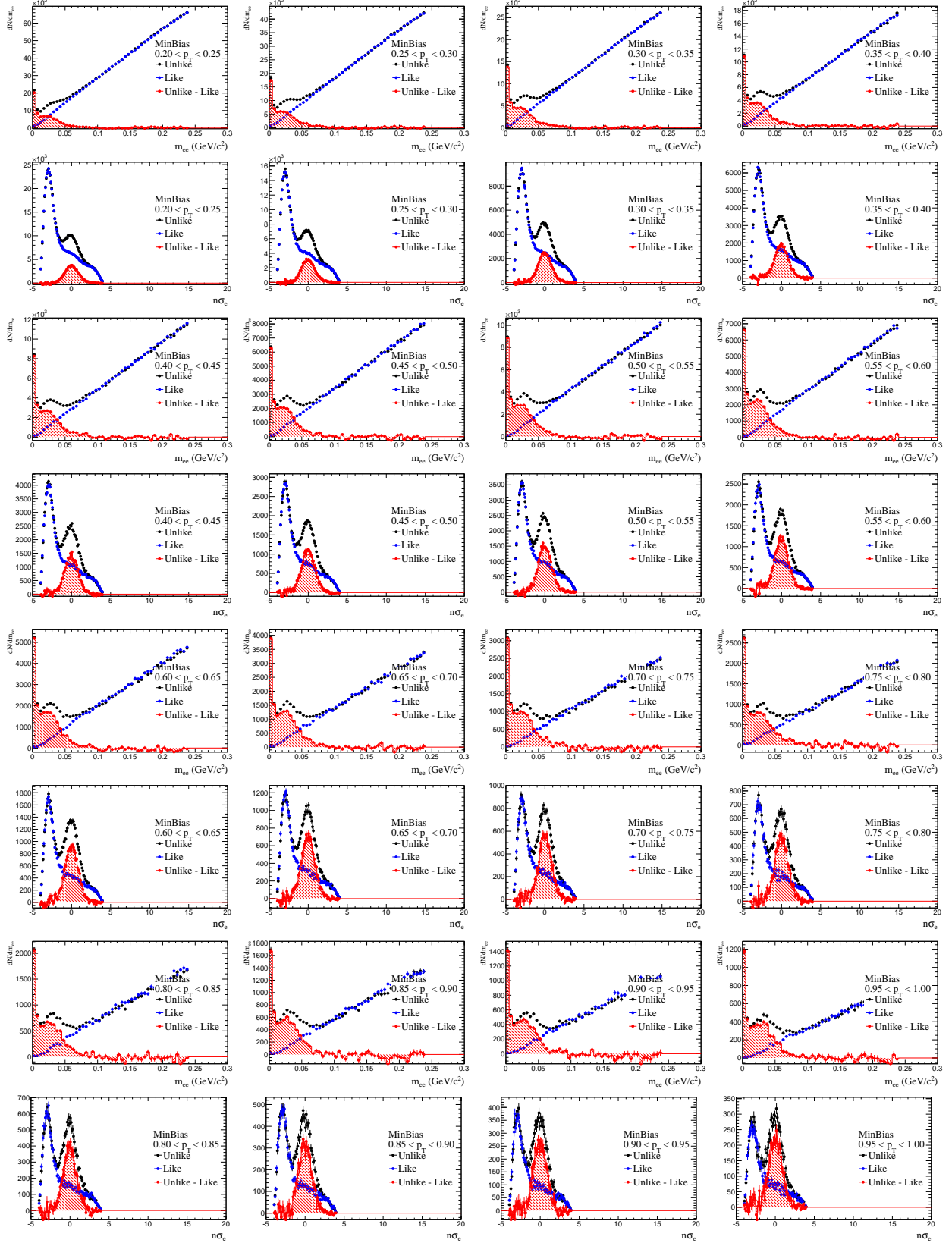


Figure 3.13.: (Color online) Low- p_T photonic-electrons inv. mass dist. in p_T -bins. Also shown for every p_T bin the distribution of the partner track $n\sigma_e$; since no eID cuts are placed on the partner the $n\sigma_e$ distribution serves as another photonic electrons purity check.

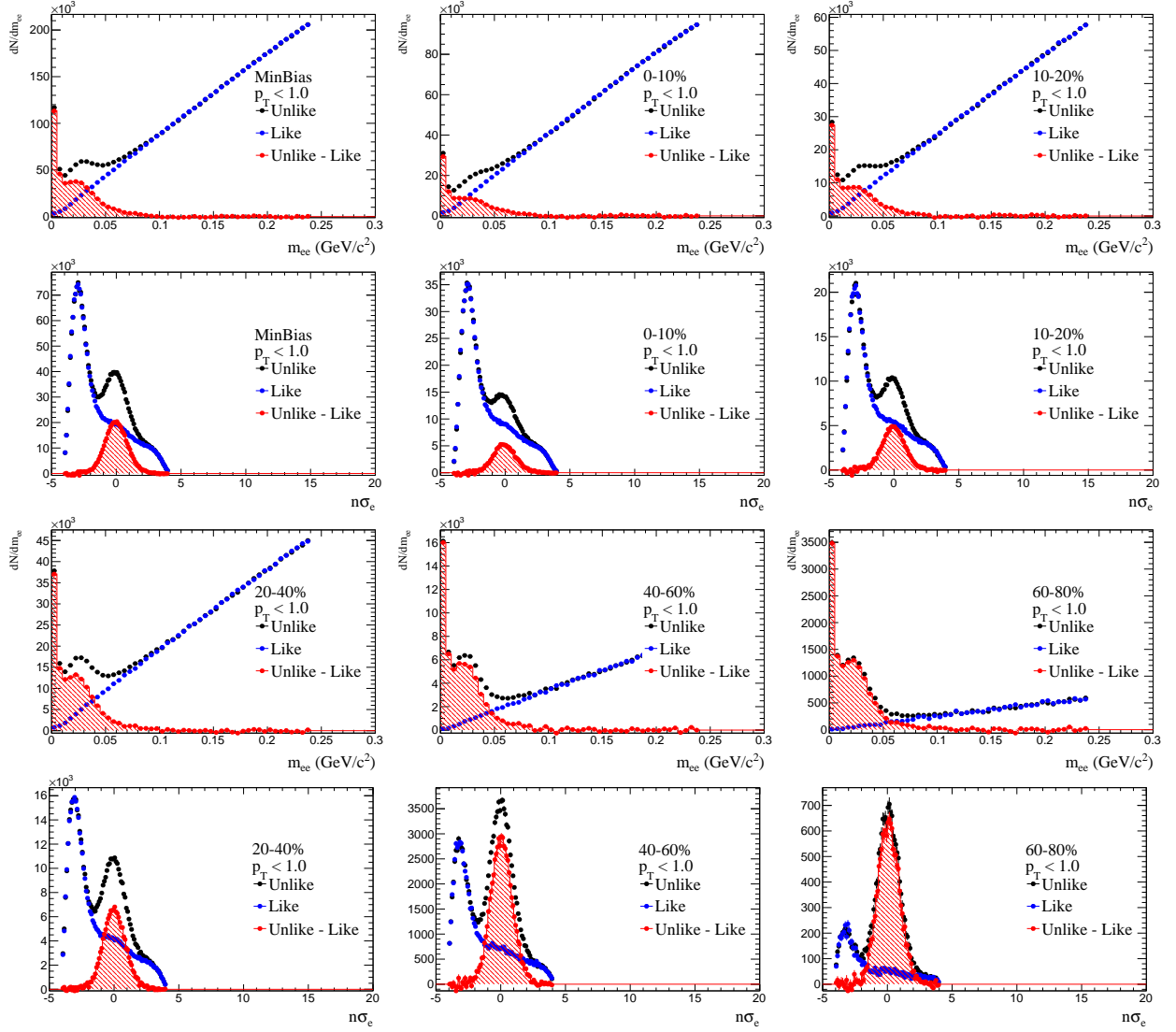


Figure 3.14.: (Color online) Low- p_T photonic-electrons inv. mass dist. in centrality-bins. Also shown for every centrality bin the distribution of the partner track $n\sigma_e$; since no eID cuts are placed on the partner the $n\sigma_e$ distribution serves as another photonic electrons purity check.

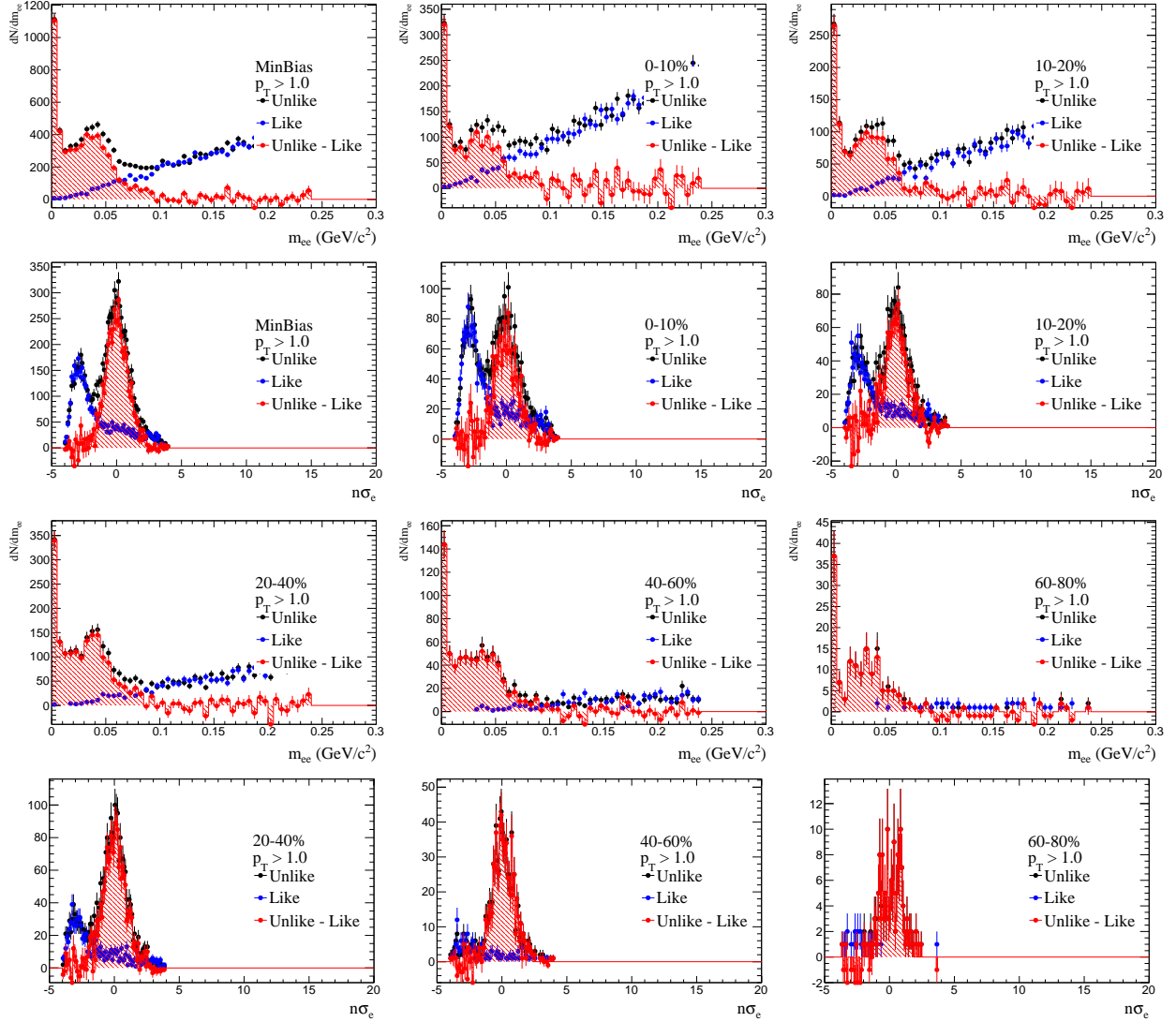


Figure 3.15.: (Color online) High- p_T photonic-electrons inv. mass dist. in centrality-bins. Also shown for every centrality bin the distribution of the partner track $n\sigma_e$; since no eID cuts are placed on the partner the $n\sigma_e$ distribution serves as another photonic electrons purity check.

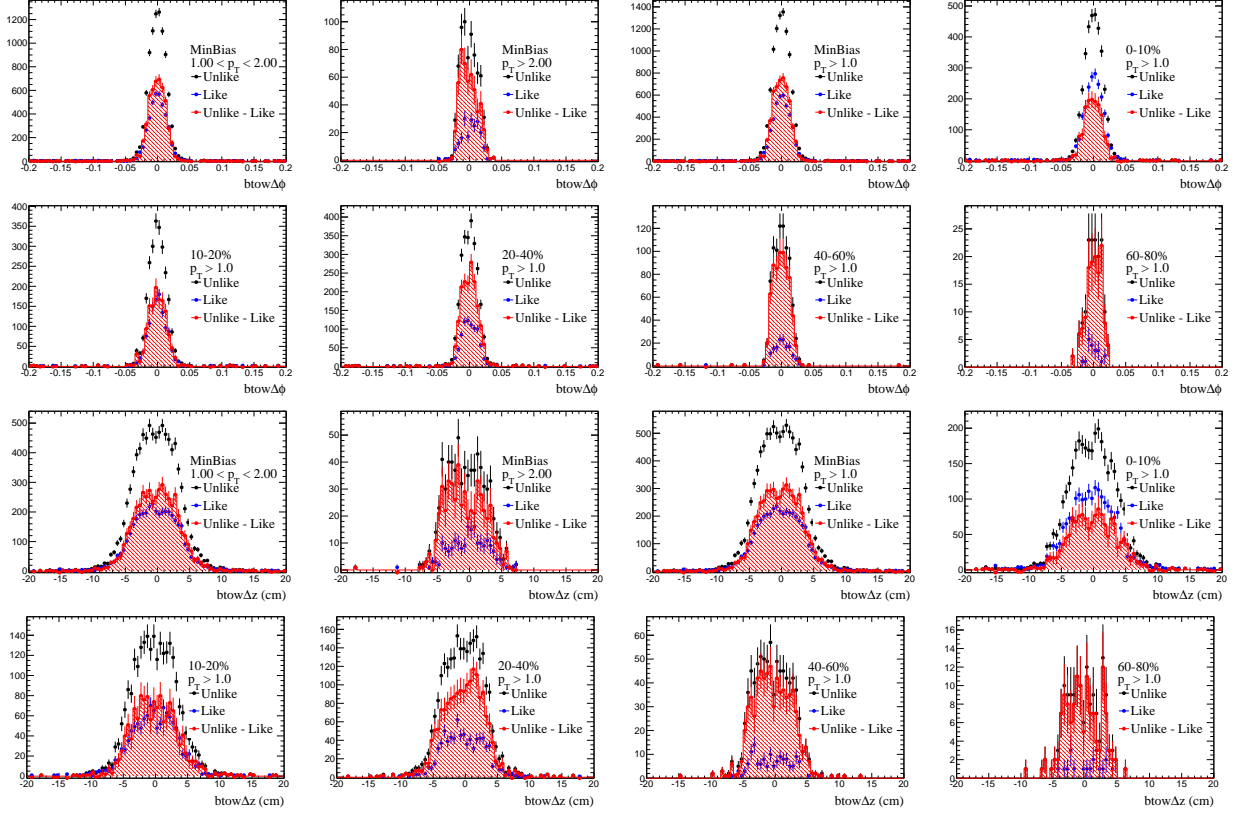


Figure 3.16.: (Color online) (Top two rows) BTOW($\Delta\phi$) distributions after applying all eID cuts except cut on BTOW($\Delta\phi$), the eID cut chosen is $|\text{btow}\Delta\phi| < 0.05$. (Bottom two rows) BTOW(Δz) distributions after applying all eID cuts except cut on BTOW(Δz) itself, the eID chosen is $|\text{btow}\Delta z| < 10$ cm. Two p_T -bins are shown for 0 – 80% centrality and one p_T -bin for all other centralities.

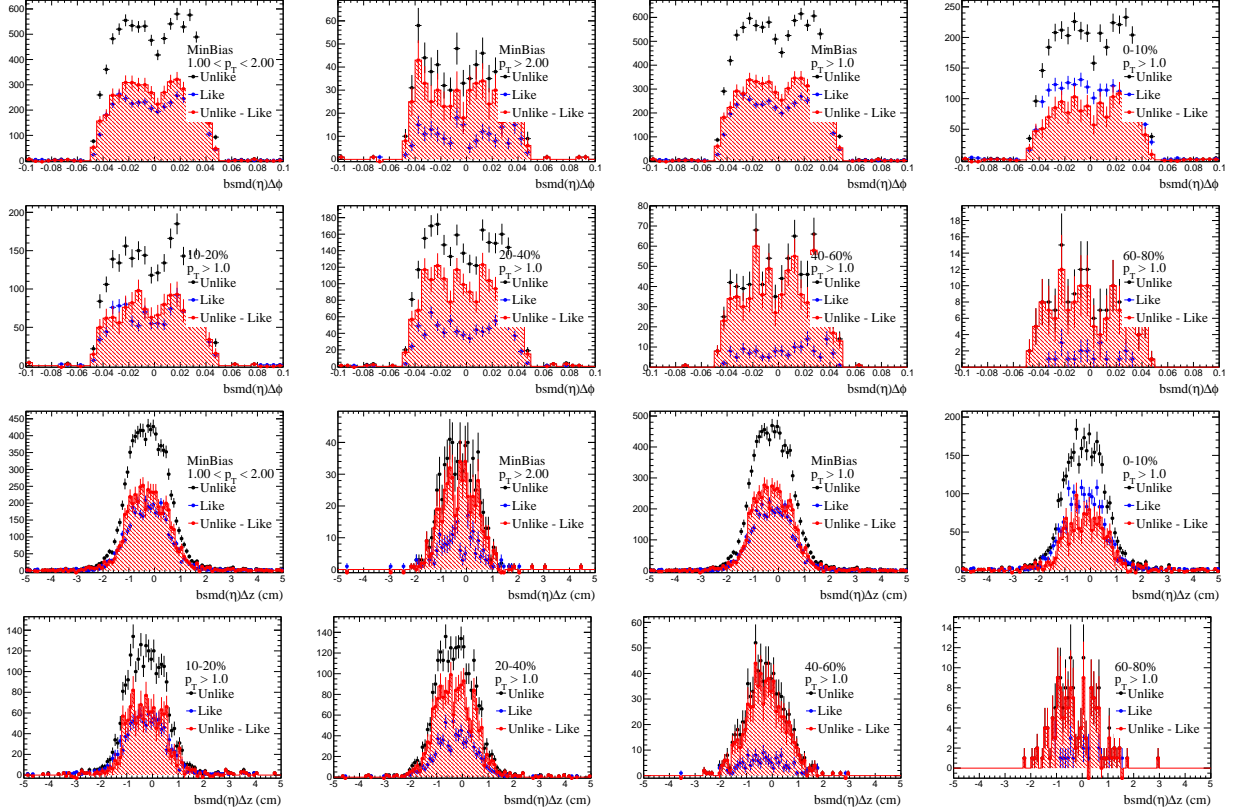


Figure 3.17.: (Color online) (Top two rows) $\text{BSMD}\eta(\Delta\phi)$ distributions after applying all eID cuts except cut on $\text{BSMD}\eta(\Delta\phi)$ itself, the chosen eID cut is $|\text{BSMD}(\eta)\Delta\phi| < 0.06$. (Bottom two rows) $\text{BSMD}\eta(\Delta z)$ distributions after applying all eID cuts except cut on $\text{BSMD}\eta(\Delta z)$ itself, the chosen eID cut is $|\text{BSMD}\eta\Delta z| < 3.0$ cm. Two p_T -bins are shown for 0 – 80% centrality and one p_T -bin for all other centralities.

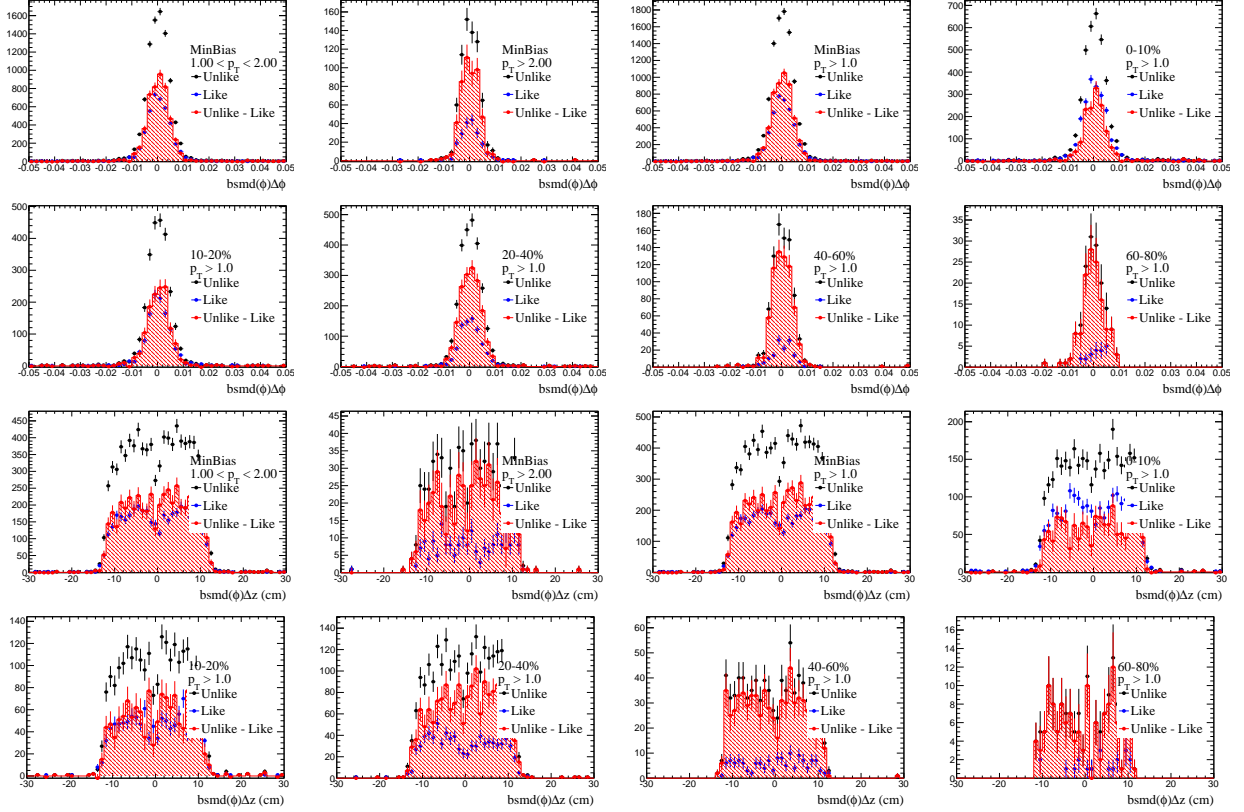


Figure 3.18.: (Color online) (Top two rows) $BSMD\phi(\Delta\phi)$ distributions after applying all eID cuts except cut on $BSMD\phi(\Delta\phi)$ itself, the chosen eID cut is $|bsmd(\phi)\Delta\phi| < 0.0015$. (Bottom two rows) $BSMD\phi(\Delta z)$ distributions after applying all eID cuts except cut on $BSMD\phi(\Delta z)$ itself, the chosen eID cut is $|bsmd\phi\Delta z| < 16.0$ cm. Two p_T -bins are shown for 0 – 80% centrality and one p_T -bin for all other centralities.

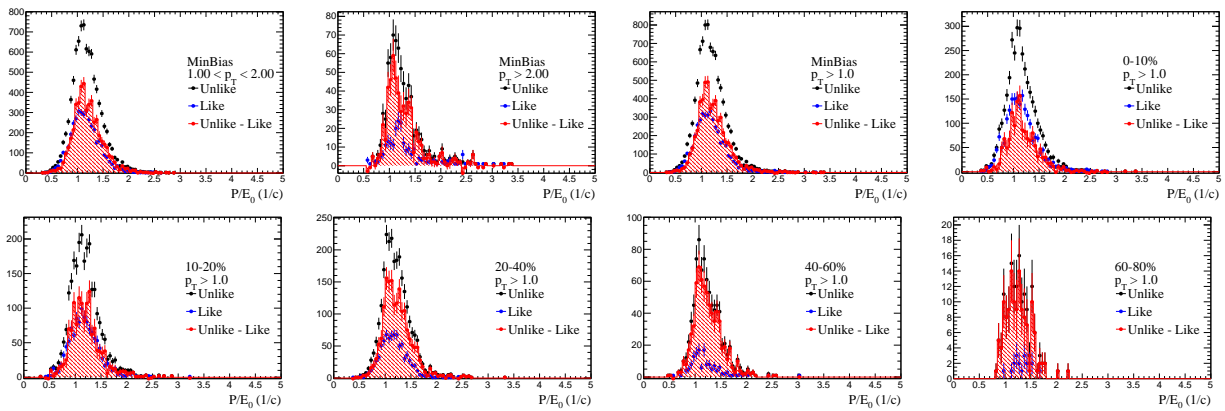


Figure 3.19.: (Color online) p/E_0 distributions after applying all eID cuts except cut on p/E_0 itself, the cut is chosen to be $0.3 < p/E_0 < 2.0$. The distributions clearly peak ~ 1.0 as expected from electrons, the slight shift to higher than 1.0 is because the energy of the highest tower E_0 is used instead of the cluster energy E . Two p_T -bins are shown for 0 – 80% centrality and one p_T -bin for all other centralities.

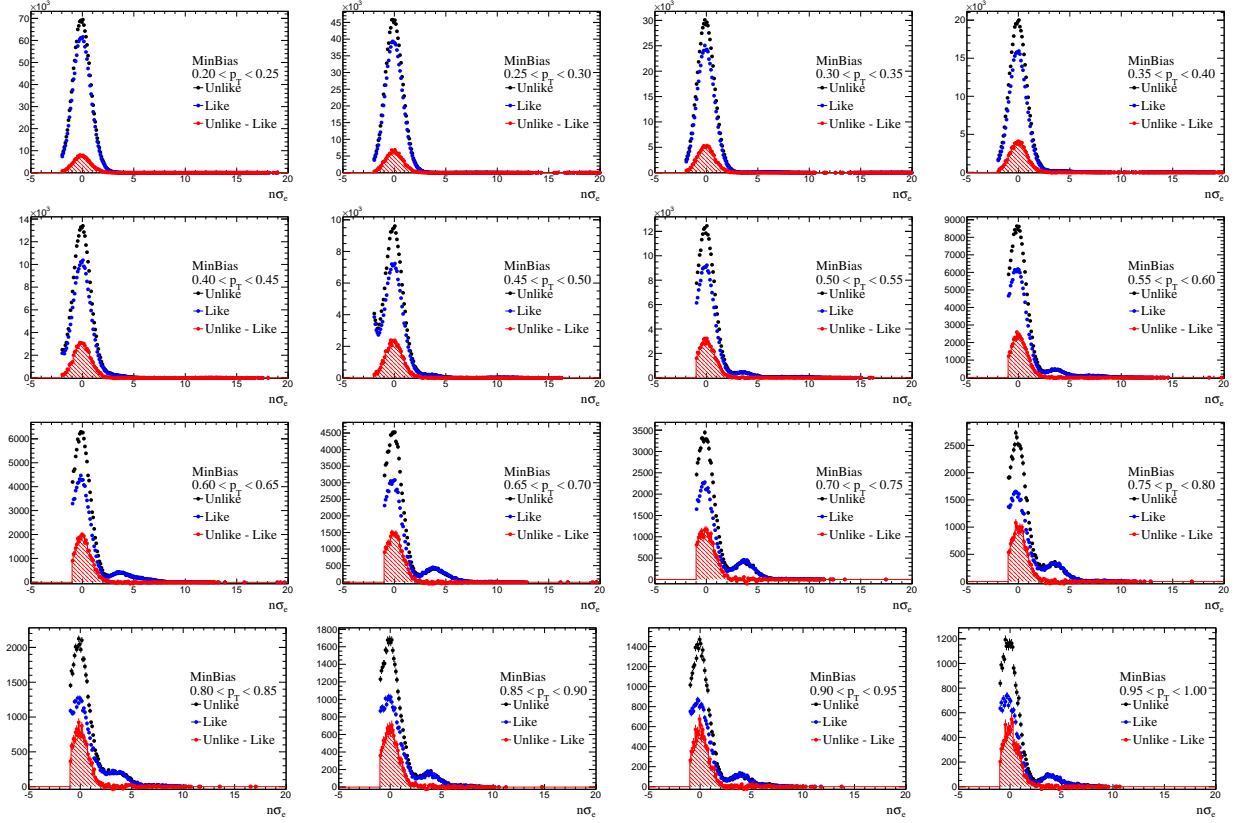


Figure 3.20.: (Color online) Low- p_T $n\sigma_e$ distribution in p_T -bins, the eID cut chosen is $0 < n\sigma_e < 2.0$, due to the approximate symmetry of the $n\sigma_e$ distribution such a cut has a $\sim 50\%$ efficiency, however it ensures a pure photonic electrons sample. The artificial cut which appears on the left shoulder of the distributions is applied in the original data structure production used in this analysis to suppress the size of the files.

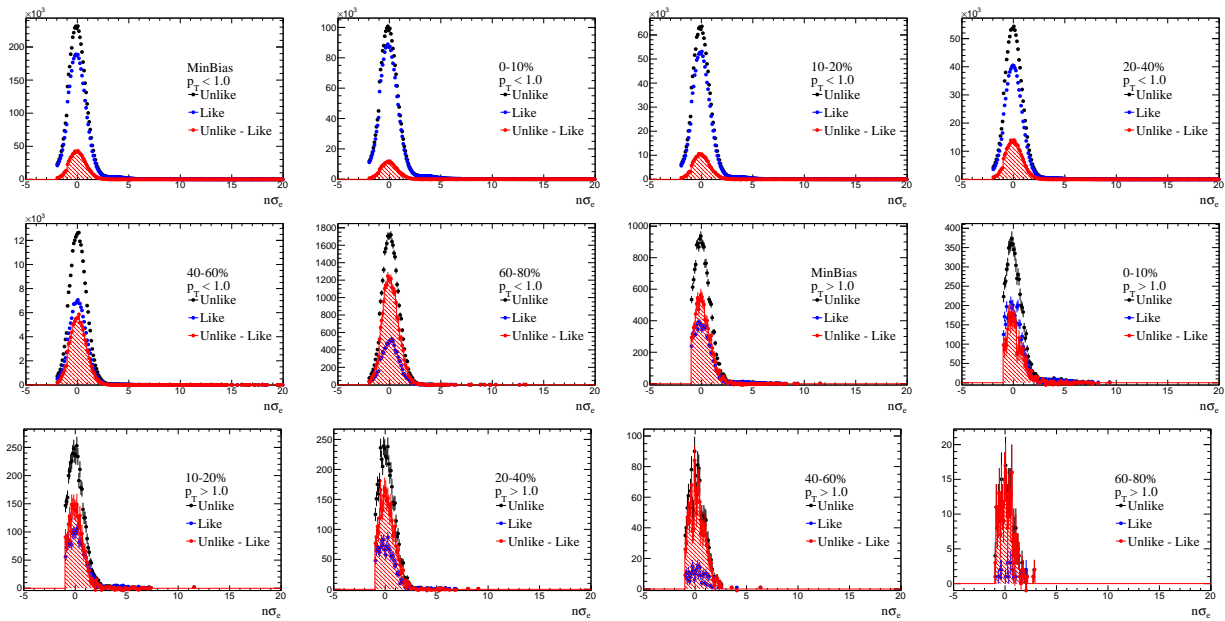


Figure 3.21.: (Color online) High- p_T $n\sigma_e$ distributions in centrality-bins, the eID cut chosen is $0 < n\sigma_e < 3.0$, due to the approximate symmetry of the $n\sigma_e$ distribution such a cut has a $\sim 50\%$ efficiency, however it ensures a pure photonic electrons sample. The artificial cut which appears on the left shoulder of the distributions is applied in the original data structure production used in this analysis to suppress the size of the files.

3.4.2 Electron identification cuts efficiencies

Once electron identification cuts are determined one needs to calculate the efficiencies of these cuts. To calculate the efficiency of a certain cut a pure electrons sample without applying the cut in question is needed. Unfortunately, it is not possible to get pure electrons without applying TOF and BEMC cuts, i.e. with applying $n\sigma_e$ cut only. One trick to get around this issue is to use photonic electrons to calculate the efficiencies with applying tight TOF cuts on the partner. The TOF cuts applied on the partner here are the same ones which were applied for the primary electrons tracks, Table.3.5.

The efficiency in question is calculated as,

$$\epsilon_{cut} = \frac{(\text{electrons with "cut" applied}) \ \&\& \ \text{TOF partner cuts}}{(\text{electrons without "cut"}) \ \&\& \ \text{TOF partner cuts}} \quad (3.4)$$

where “cut” is either BEMC or TOF. A crucial step in this method is to verify the purity of the electrons in the denominator. We do this by examining the invariant mass plots.

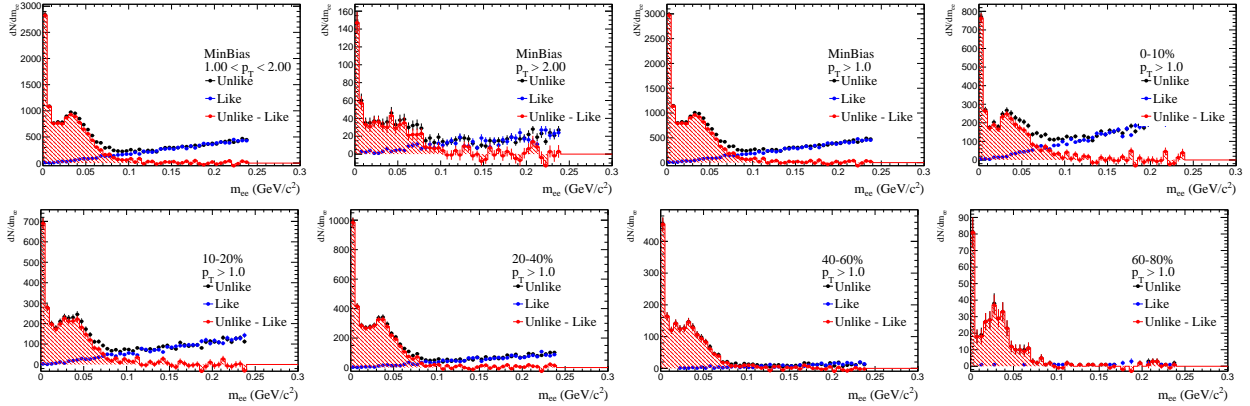


Figure 3.22.: (Color online) Inv. mass distr. w/o BEMC cuts with TOF cuts on partner. The plots clearly show a pure electron sample without BEMC cuts which is necessary to calculate the BEMC efficiency from data.

Fig.3.22 shows the invariant mass plots of photonic electrons with TOF cuts applied on the partner tracks and without BEMC cuts on the primary track. Eq.3.4 is

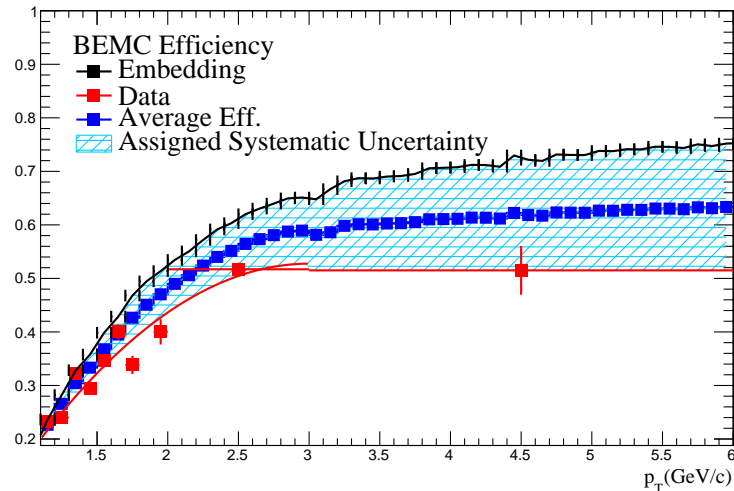


Figure 3.23.: (Color online) BEMC electrons ident. eff. in centrality bins.

used to calculate the efficiency. The red points in Fig.3.23 are the efficiency calculated from this method. The statistical fluctuations are clear in the figure, and for high- p_T it was not possible to break the efficiency to finer p_T -bins for lack of statistics. After carrying an independent study of BEMC efficiency from simulations (from embedding, see 3.5 for more details on embedding, also an extensive comparison between BEMC distributions in data and embedding is available on STAR protected area [73]) it turned out there is a $\sim 20\%$ mismatch in the efficiency between data and embedding. The poor statistics in data made it difficult to investigate the reason behind this mismatch. In this case the average efficiency from embedding and data has been used and the difference has been assigned as a systematic uncertainty, see Fig.3.23. This approach has been taken for non-photonic electrons analyses at all energies from RHIC run year 2010.

Fig.3.24 and Fig.3.25 show the invariant mass distributions of photonic electrons with TOF cuts on the partner tracks and without TOF cuts on the primary track. Again, it is clear in the plots that we can get a pure photonic electrons sample using this method. Eq.3.4 is used to calculate the TOF eID efficiency shown in closed squares in Fig.3.26 left. Generally speaking $\sim 30\%$ of true TPC tracks from the

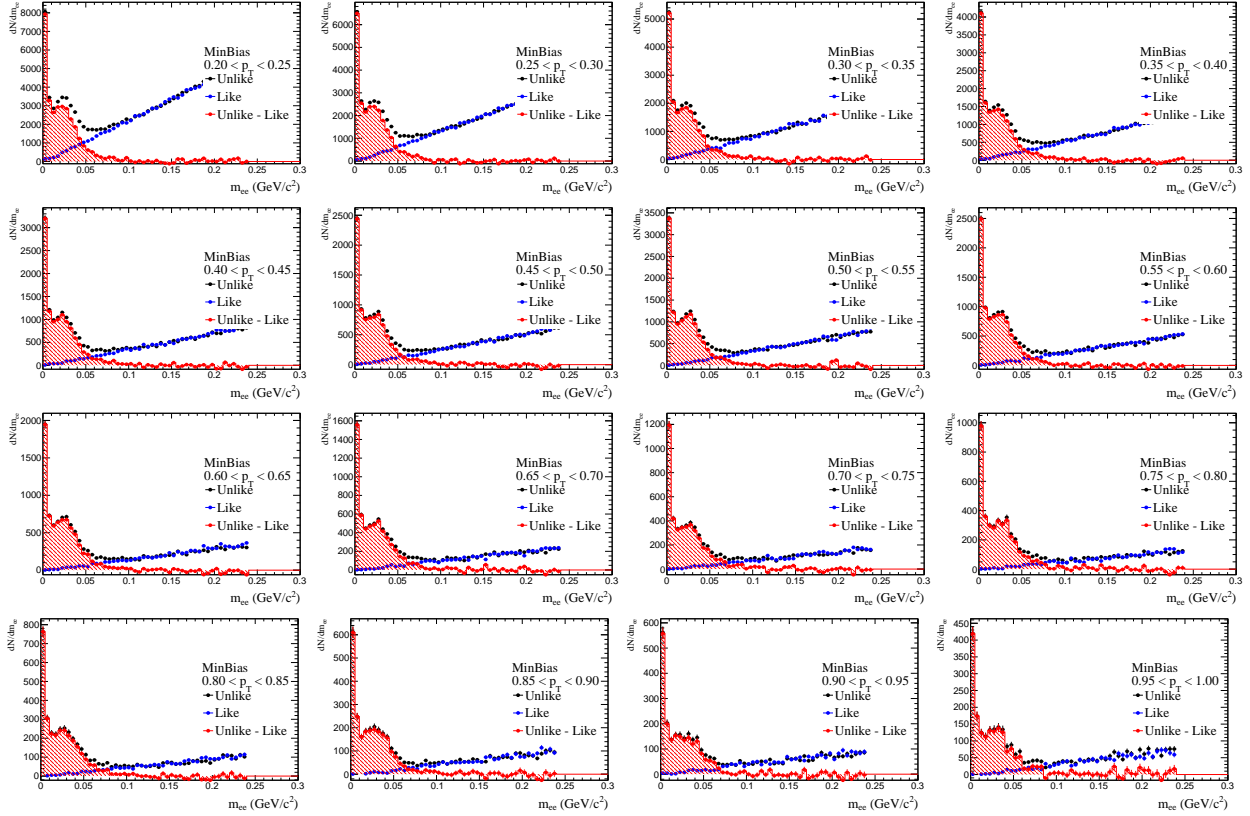


Figure 3.24.: (Color online) Inv. mass dist. w/o TOF cuts with TOF cuts on partner in p_T -bins.

triggered event are not matched to any TOF hits, this is due to TOF acceptance and other TOF hits matching criteria. This so-called TOF-matching efficiency is “almost” the same for all tracks, so hadrons are used to calculate this efficiency as

$$\epsilon_{\text{matching}} = \frac{\beta > 0}{\text{no } \beta \text{ cut}}$$

where β is the track speed from TOF. The cuts listed in Table.3.6 have applied to the denominator and numerator of the TOF-matching efficiency above. Fig.3.26 left plot shows the matching efficiency in closed circles. The right plot in the same figure shows the convolution of TOF matching and eID efficiencies.

Calculating the $n\sigma_e$ eID efficiency from $Au+Au \sqrt{s_{NN}} = 62.4$ GeV data proved to be a formidable task because of the low statistics. In general the $n\sigma_e$ cut efficiency

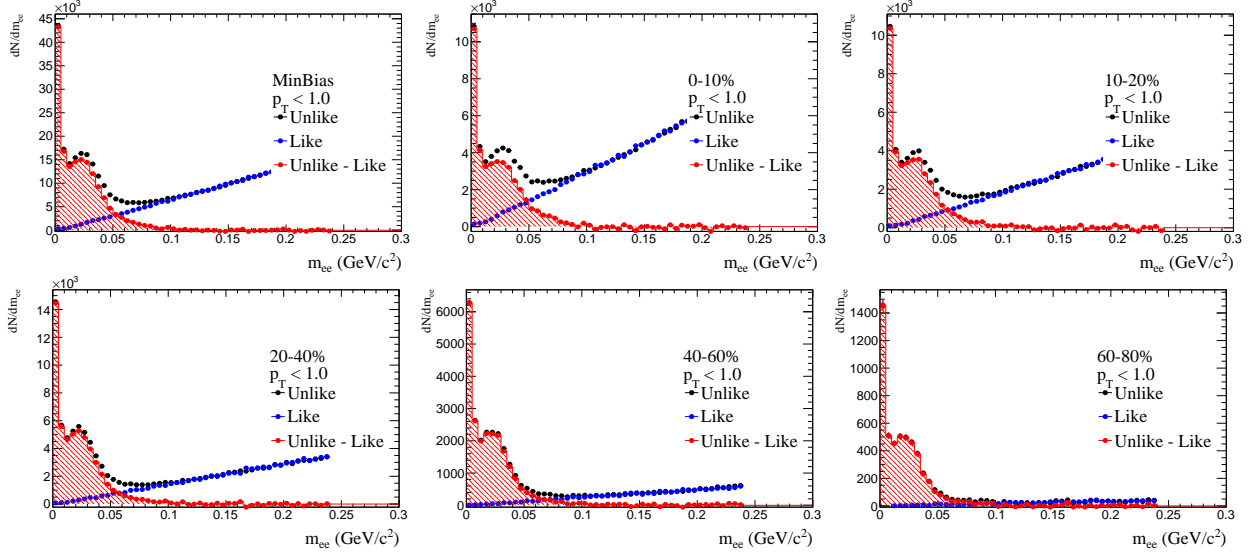


Figure 3.25.: (Color online) Inv. mass dist. w/o TOF cuts with tight partner cuts in centrality bins.

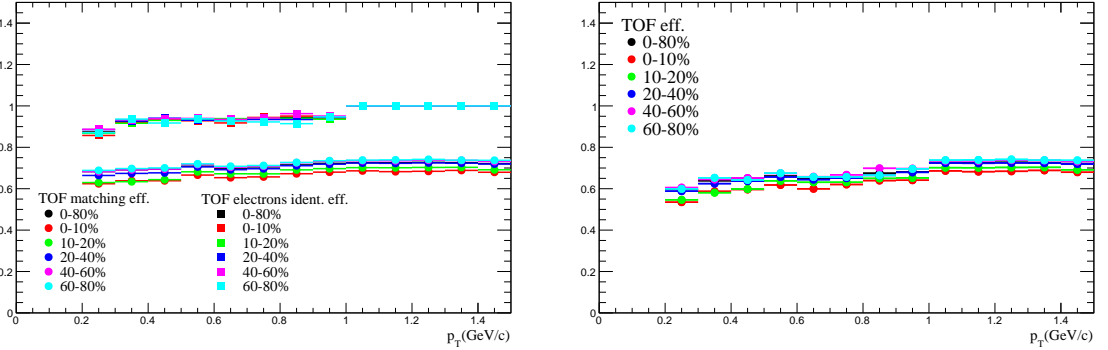
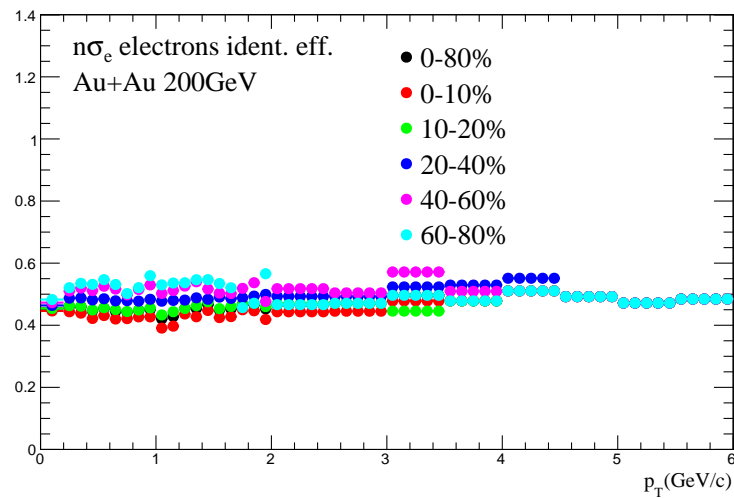


Figure 3.26.: (Color online) (Left) TOF matching and elec. ident. eff. (Right) Total TOF eff.

is calculated from photonic electrons unlike-like $n\sigma_e$ distributions. In this analysis we used the distributions from the $Au+Au \sqrt{s_{NN}} = 200$ GeV data which was collected in the same year and received the same TPC calibrations. While it is true that this efficiency depends on the luminosity (TPC occupancy), the dependence is mild. Fig.3.27 shows the $n\sigma_e$ cut efficiency calculated from $Au+Au \sqrt{s_{NN}} = 200$ GeV data.

Table 3.6: Cuts used for TOF-matching efficiency.

$ V_z < 40.0 \text{ cm} \ \&\& \ V_r < 1.0 \text{ cm}$
$ V_z - V_{vpd} < 4.0 \text{ cm}$
refMult > 7
Primary tracks with nFit > 20 && nFit/nMax > 0.52
gDCA < 1.5 cm
R(1st TPC point) < 73 cm
$ n\sigma_\pi < 1.0$

Figure 3.27.: (Color online) $n\sigma_e$ electrons ident. eff. in centrality bins.

Finally, the TOF, BEMC and $n\sigma_e$ efficiencies are convoluted to get the total eID efficiency shown in Fig.3.28.

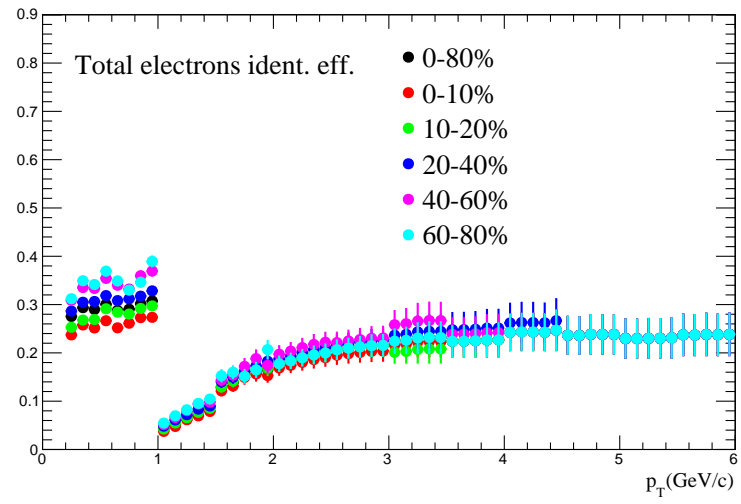


Figure 3.28.: (Color online) Overall electrons ident. eff. in centrality bins.

3.5 Detector acceptance and efficiencies corrections

3.5.1 Single electrons reconstruction efficiency

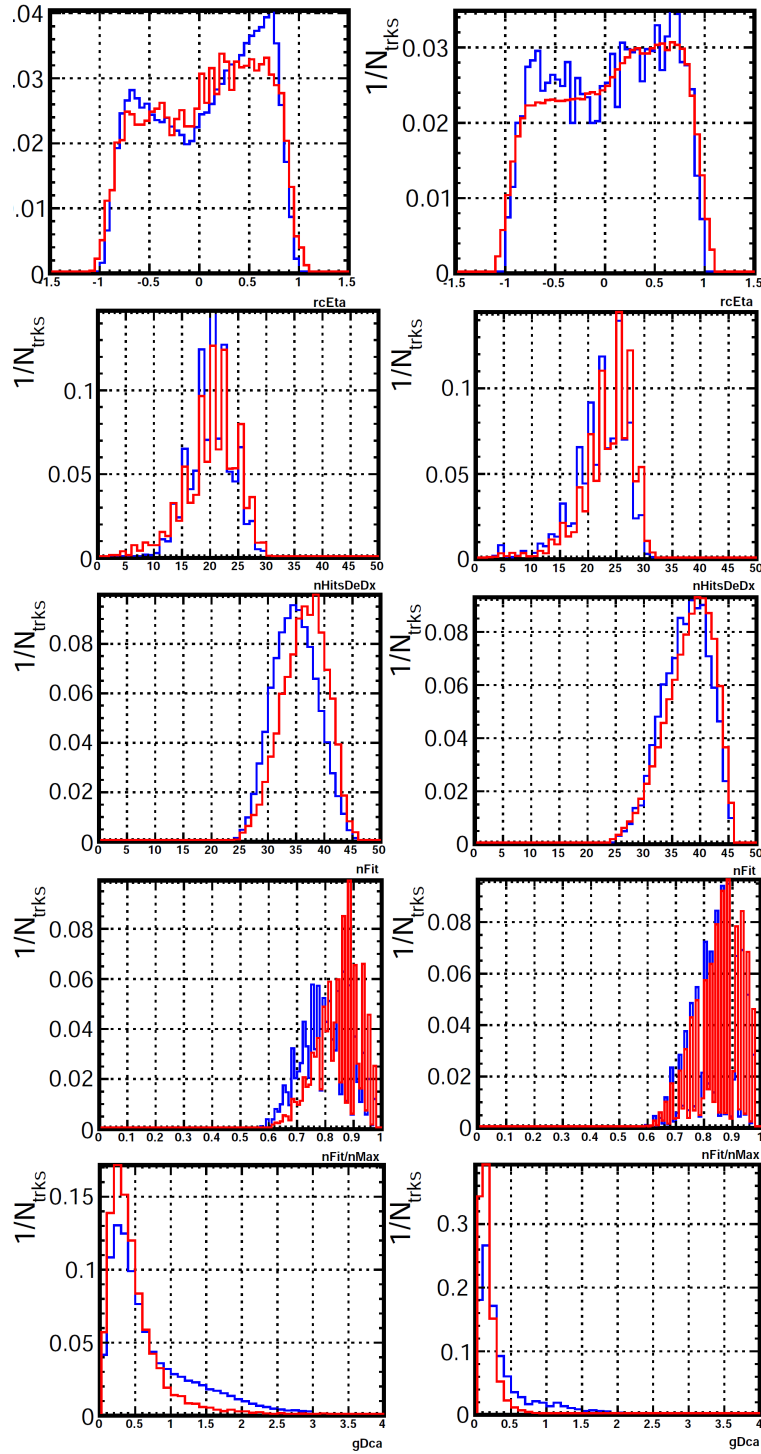


Figure 3.29.: (Color online) Comparison of reconstructed from embedding (red) to photonic electrons from data (blue).

The TPC tracking efficiency is calculated from embedding simulation; Monte-Carlo (MC) tracks pass through a full STAR GEANT [74] simulation chain which includes the full STAR geometry with correct material budget and simulation of the TPC and BEMC detectors response. The simulated data is then embedded in a representative sample of raw data of the same data used for this analysis. The final data goes into the same reconstruction chain and calibration as the ones used for the real data reconstruction. Real pile-up effects are also included in simulation to mimic the real running conditions which significantly affects tracking efficiencies. To make sure the detector response is well simulated an extensive embedding-data comparison quality-assurance (QA) study has been carried out [73]. This QA study has been done in ϕ -, η -, p_T - bins for all centralities and compared directly to the electrons distributions obtained from real data. Fig.3.29 shows a few plots extracted from that study. The QA demonstrated that STAR detector response is very well simulated. In addition to the comparison of tracking distributions between data and embedding, the study also included an extensive comparison of BEMC hit points distributions which were relied on to calculate BEMC efficiency from embedding.

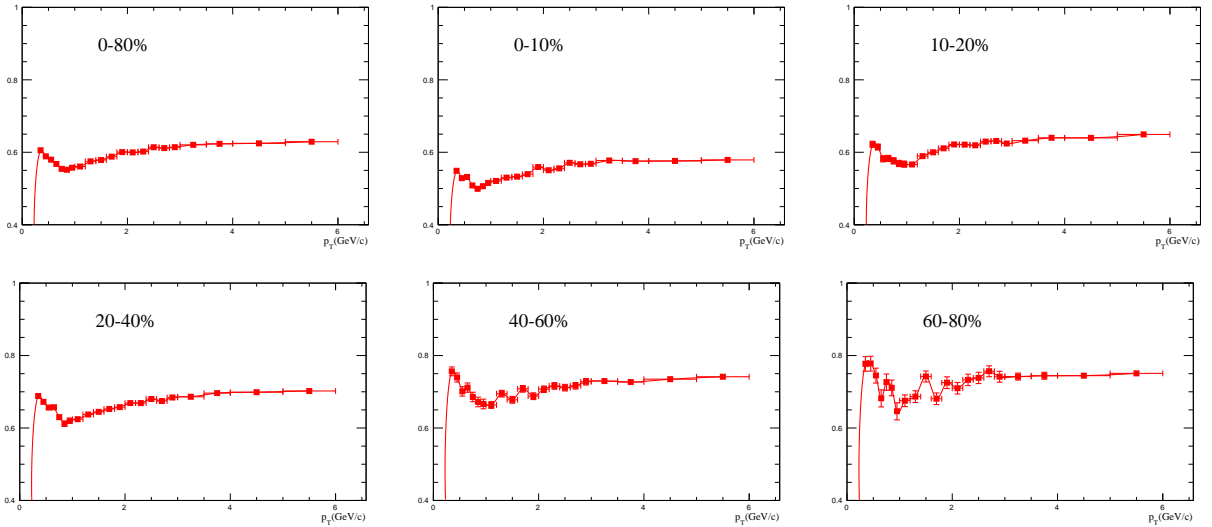


Figure 3.30.: Single track reconstruction efficiency in centrality bins.

The tracking cuts applied in this analysis (nFit,nFit/nMax,gDCA,first TPC point and ndEdx) are intrinsically correlated, for this reason one efficiency is calculated to account for all of them. The efficiency is calculated as the ratio of number of reconstructed MC tracks which pass the same cuts as in the data to the number of embedded tracks, the procedure is done in p_T and centrality bins,

$$\epsilon_{reco}(p_T) = \frac{\text{nFit} > 20.0 \ \&\& \ \text{nFit/nMax} > 0.52 \ \&\& \ |\text{gDCA}| < 1.5 \ \&\& \ \text{R(first TPC)} < 73.0 \ \&\& \ \text{ndEdx} > 15}{\text{Embedded MC tracks}} \quad (3.5)$$

Fig.3.30 shows the result of this efficiency calculation in centrality bins.

3.5.2 Photonic electrons reconstruction efficiency

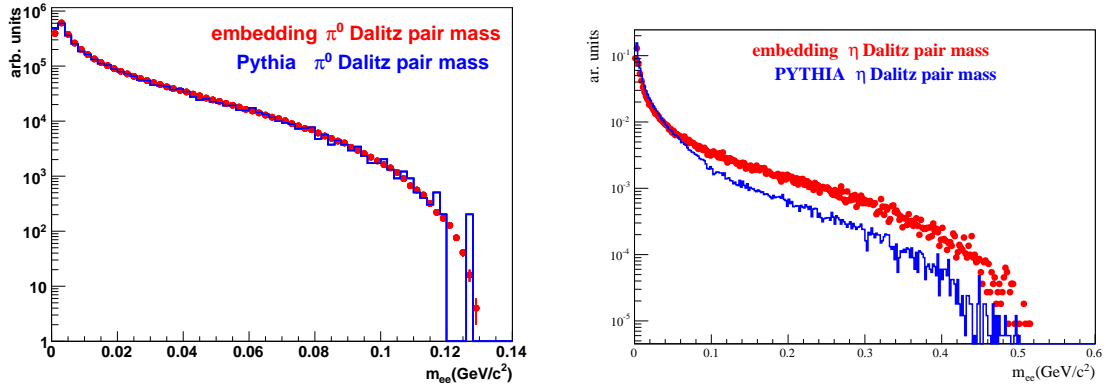


Figure 3.31.: (Color online) A comparison of the mass shape of electron-positron pairs from π^0 and η Dalitz decays from PYTHIA and modified STAR GEANT routines. (Left) PYTHIA and GEANT are in perfect agreement for the π^0 Dalitz decay. (Right) A mismatch is observed between the PYTHIA and the modified GEANT in the case of η Dalitz decay.

Not all photonic electrons are reconstructed using the invariant mass method. To correct for this inefficiency we carry out a full embedding for each of the photonic electrons sources separately. MC particles go into a full STAR GEANT [74] simulation which includes all the detector geometry details, material budget and correct TPC and BEMC detectors response simulation. Then the simulated data is embedded in a representative sample of the real data used for the analysis, the raw data is then

passed into the same reconstruction chain as the real data with the same calibration. We specifically study embedding of γ for photonic conversion, and π^0 and η dalitz decays. Dalitz decay is not correctly treated in vanilla GEANT-3.2 [68]. Therefore, STAR GEANT has been modified to use the correct Kroll-Wada decay formalism [75], with using a recent form factor from [76] for the modification of the decay kinematics by the dynamic electromagnetic structure at the transition vertex. A comparison of the mass shape of the modified GEANT routines used in STAR embedding to that from PYTHIA-6.4 [77] is shown in Fig.3.31. The η -electron-pair mass shape is not the same as we get from PYTHIA, this matter is still under investigation, we are particularly interested in checking how the mass shape changes as we vary the parameters of the form factor within their experimental uncertainty from [76]. Nevertheless, this is not an issue for this analysis since, as will be shown later in this dissertation, η Dalitz decays contribute only 10% of our photonic electrons and the reconstruction efficiency is very similar for conversion and Dalitz decays.

Embedding production has been studied for quality assurance (QA) by carrying out an extensive comparison of the TPC tracking and BEMC response to photonic electrons from real data. The QA has been done in p_T , ϕ , and centrality bins [78].

The Monte-Carlo photonic sources were embedded flat in p_T, ϕ and η . To correct for p_T -shape of the original sources we fit a combined spectra from STAR charged pions [79] and PHENIX neutral pions [80]. STAR data was used for ($0 < p_T < 0.85$) GeV/ c and PHENIX for ($0.9 < p_T < 9.5$) GeV/ c in most centrality bins. The results of the fits are shown in Fig.3.32. The fit function used is

$$\frac{1}{2\pi p_T} \frac{d^2 N}{dp_T d\eta} = A \left(\exp^{-(ap_T + bp_T^2)} + p_T/p_0 \right) \quad (3.6)$$

which is basically a power-law with an exponential to cover the non-perturbative low- p_T region. The fit parameters results are displayed in the figure.

The result fits were used directly to weight the embedded π^0 parents. For η we assume m_T scaling of the π p_T -shape, i.e. the p_T of the fits has been replaced by $\sqrt{p_T^2 + m_\eta^2 - m_{\pi^0}^2}$. To weight the γ parents we use PYTHIA to decay the π^0 and η

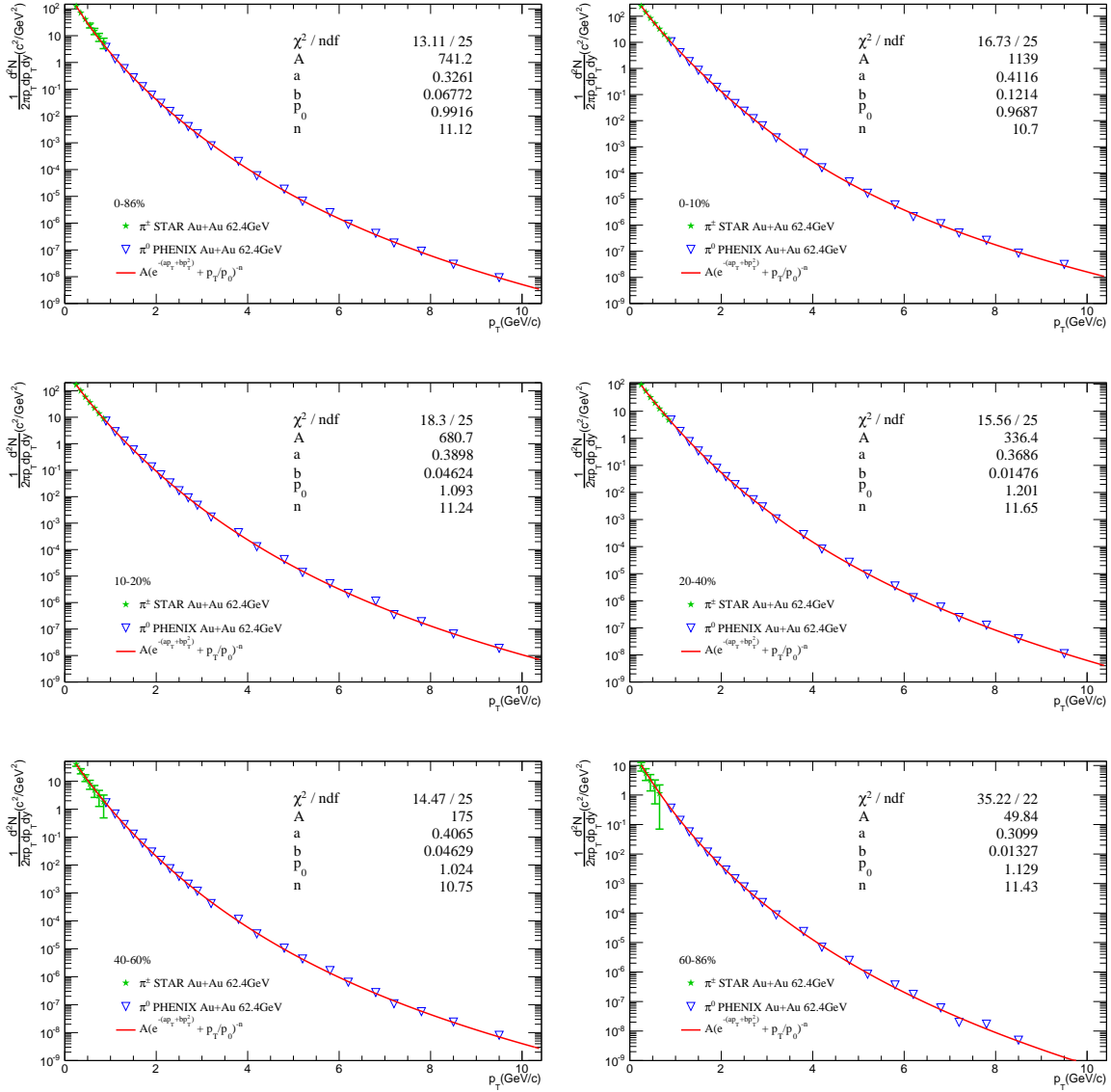


Figure 3.32.: (Color online) Fits to Au+Au pions yields. Data is combined from STAR charged pions measurement [79] and PHENIX neutral pions measurement [80].

distributions to $\gamma\gamma$, and to γe^+e^- and then add the resulting distributions to use as a weight of the p_T -shape. All this procedure has been done in centrality bins.

Photonic electrons efficiency is calculated as the ratio of single electrons which were reconstructed from MC electrons using the invariant mass method to all the reconstructed MC single electrons. Same tracking cuts have been applied to the

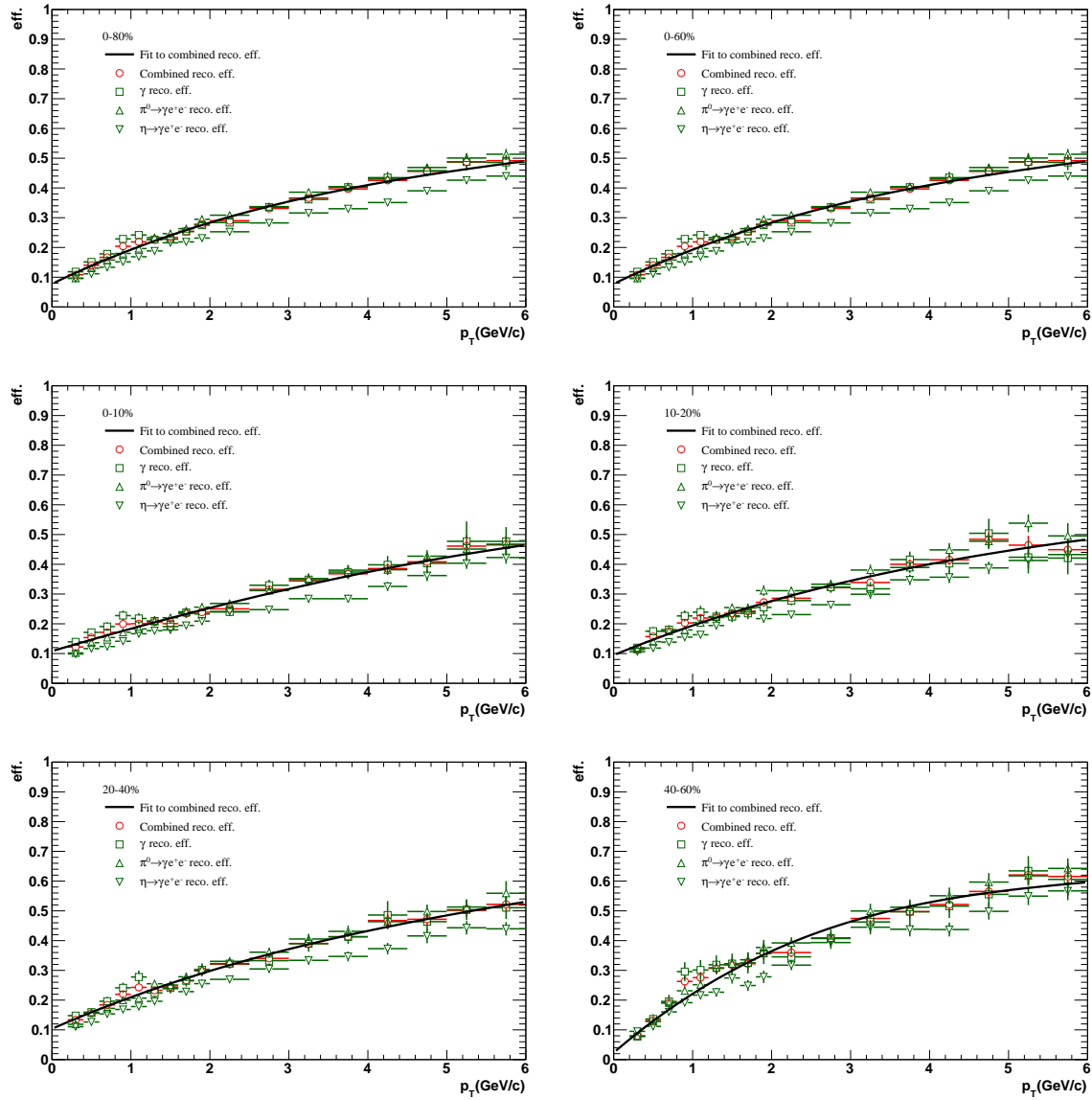


Figure 3.33.: (Color online) Photonic electrons from γ conversion, π^0 and η Dalitz decays reconstruction efficiency.

reconstructed electrons as the ones we used in real data. Fig.3.33 shows the reconstructing efficiency for photonic electrons from the different sources in centrality bins. The total reconstruction efficiency is calculated as

$$\begin{aligned} \epsilon_{pho}(p_T) = & \\ & \frac{N_e^\gamma(p_T)}{N_e^\gamma(p_T) + N_e^{\pi^0}(p_T) + N_e^\eta(p_T)} \cdot \epsilon_\gamma(p_T) + \\ & \frac{N_e^{\pi^0}(p_T)}{N_e^\gamma(p_T) + N_e^{\pi^0}(p_T) + N_e^\eta(p_T)} \cdot \epsilon_{\pi^0}(p_T) + \\ & \frac{N_e^\eta(p_T)}{N_e^\gamma(p_T) + N_e^{\pi^0}(p_T) + N_e^\eta(p_T)} \cdot \epsilon_\eta(p_T) \end{aligned} \quad (3.7)$$

where N_e^γ , $N_e^{\pi^0}$ and N_e^η are respectively the yield of electrons from photon conversion, π^0 and η Dalitz decay; ϵ_γ , ϵ_{π^0} and ϵ_η are the corresponding photonic electron reconstruction efficiencies. As we will show later in the cocktail simulation section, approximately 36% of the photonic electrons are from π^0 Dalitz decay and about 10% are from η Dalitz decay, the rest are from γ conversion. No variation was assumed since the reconstruction efficiencies from the different sources are very similar. The solid black line is a third order polynomial fit which was used as the photonic reconstruction efficiency in the master equation 3.1.

The systematic errors considered for the total reconstruction efficiency are 1) calculated by moving all the points of the total reconstruction efficiency up or down by 1σ then fitting the results. 2) By using the errors from the fits to the pions yields. Both contributions were added in quadrature point by point. Fig.3.34 shows the final reconstruction efficiency with the systematic uncertainty band.

3.6 Electron purity

Purity of the inclusive electrons is calculated from fits of the $n\sigma_e$ distribution of charged tracks after applying all electron identification cuts except the $n\sigma_e$ cut. Constrained 5 Gaussian functions for e^\pm , π^\pm , K^\pm , p^\pm and merged pions are used (some decay pions which are so close to each other are reconstructed as one track, so they have double the pions dE/dx). The mean and width of the electrons Gaussian

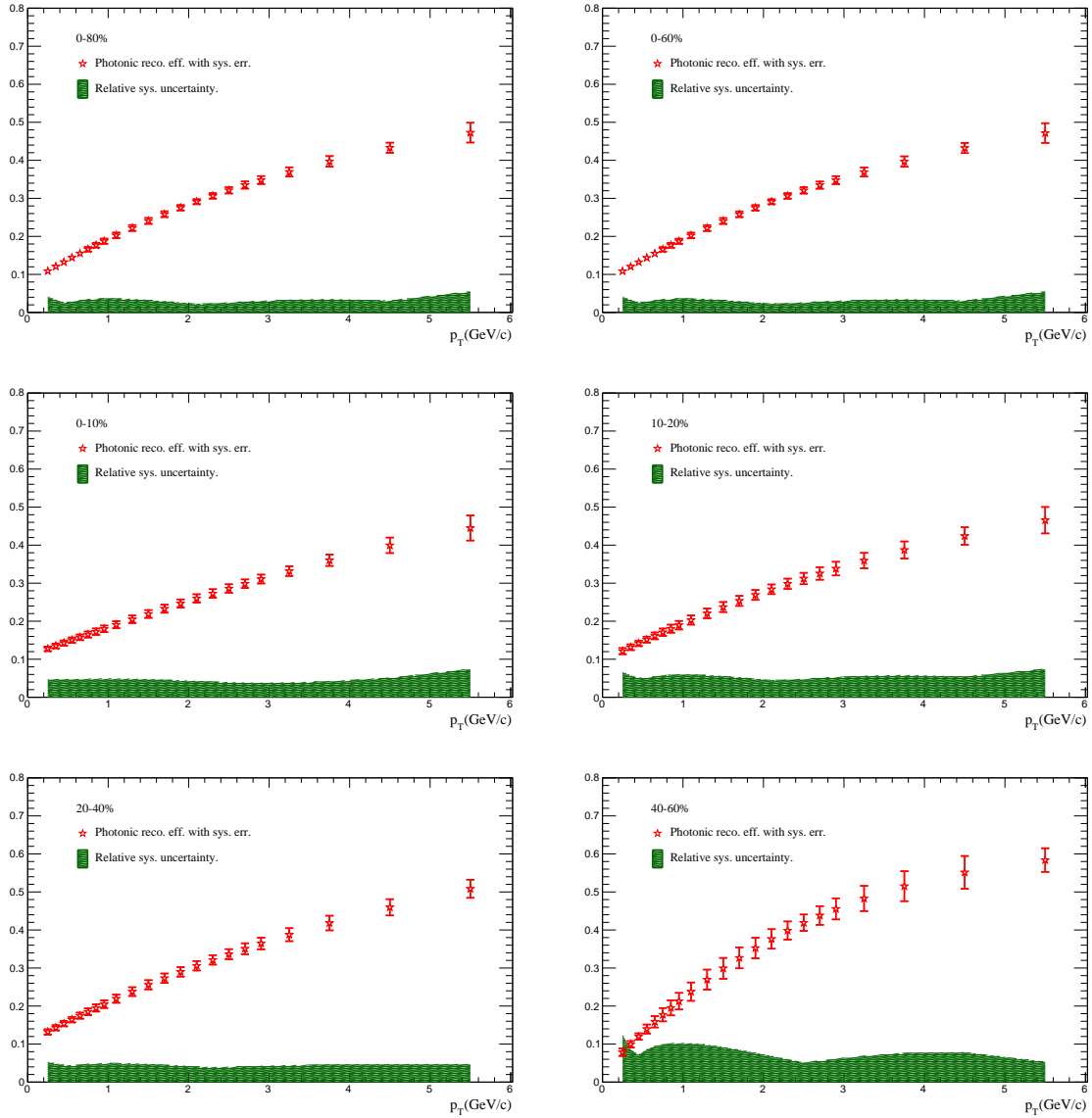


Figure 3.34.: Final photonic electrons reconstruction efficiency shown with the relative systematic uncertainty band.

has been constrained by the mean and width of the pure photonic electrons $n\sigma_e$ distributions from data π^\pm , K^\pm , p^\pm and merged pions are used. The mean and width of the electrons Gaussian has been constrained within $\pm 1\sigma$ of the mean and width of the pure photonic electrons $n\sigma_e$ distributions from data. Constrains on the other hadrons are from the expected normalized TPC energy loss value of the

Bichsel functions [66]. Fig.3.35 shows an example of the fits. This procedure has been repeated in centrality and p_T -bins.

The purity has been calculated as the ratio of the integral of the e^\pm fit to that of the total fit within the $n\sigma_e$ cut used in the data analysis. Fig.3.36 shows the result purity in centrality bins. The shaded band is an excluded region due to the instability of the fits in those p_T -bins; the proton dE/dx band crosses the electrons band in this region which is shown in Fig.2.8.

Systematic errors are the quadratic sum of fits errors and errors from varying the constraints on the fits.

3.7 Photonic electron cocktail

Although we used the invariant mass reconstruction method to subtract photonic electrons in this analysis, we also studied the photonic electrons spectra from cocktail simulation as a cross-check. GEANT [74] simulation of the STAR detector geometry, material budget, TPC and BEMC detectors response has improved significantly in the past couple of years. So now we are able to rely on simulation to study conversion in the STAR detector.

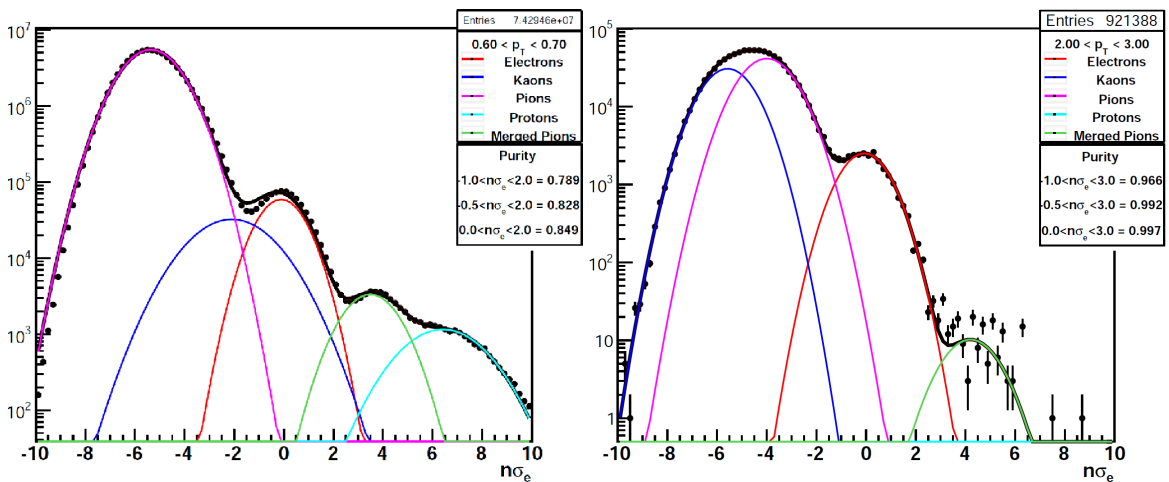


Figure 3.35.: (Color online) Example of purity fits.

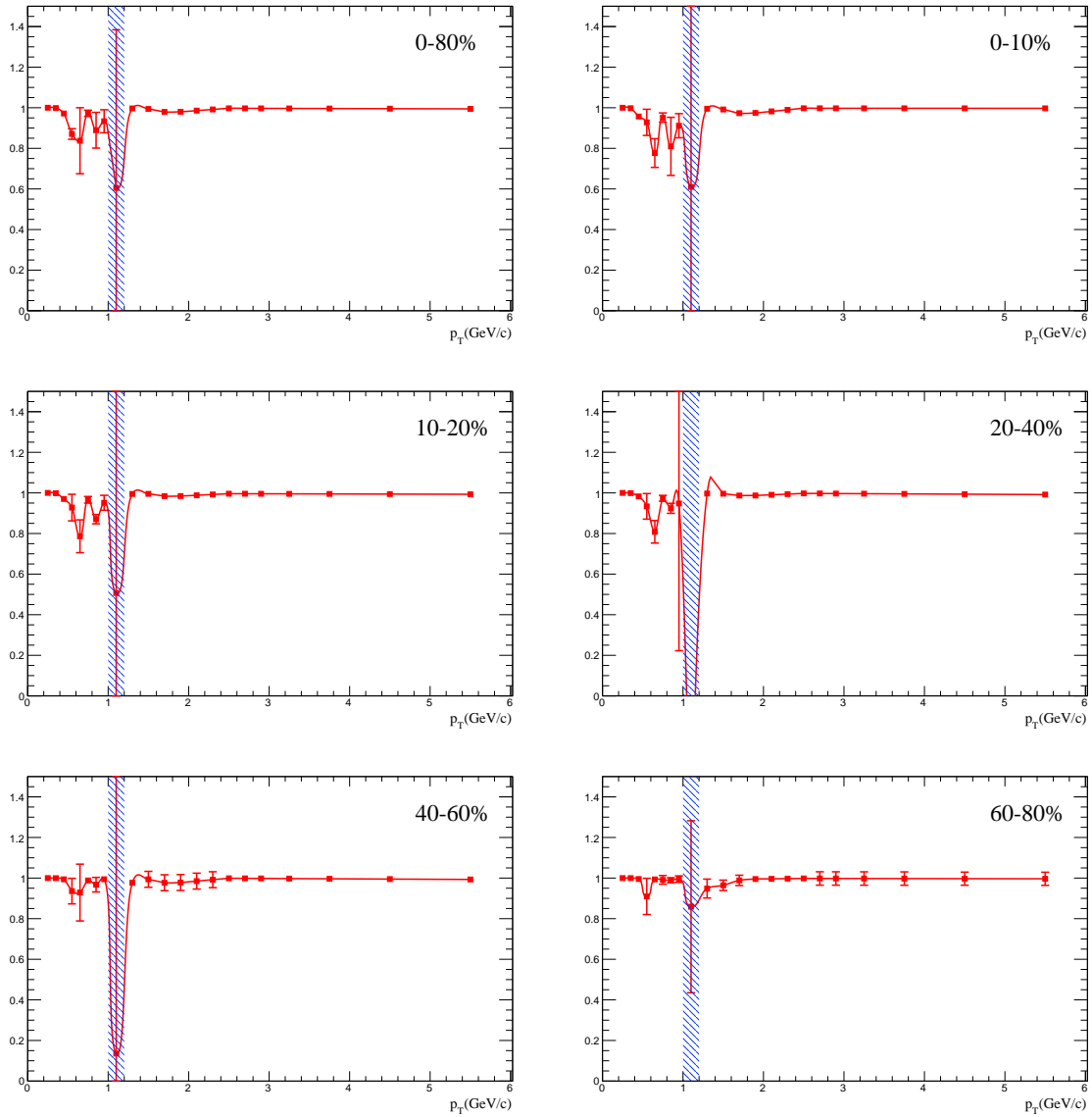


Figure 3.36.: Examples of electron purity. Shaded region is excluded because of proton dE/dx band crossing, see text.

We used the same pions fits of STAR and PHENIX data which were described in the photonic electrons reconstruction efficiency section Fig.3.32.

The procedure for the cocktail simulation is as follows:

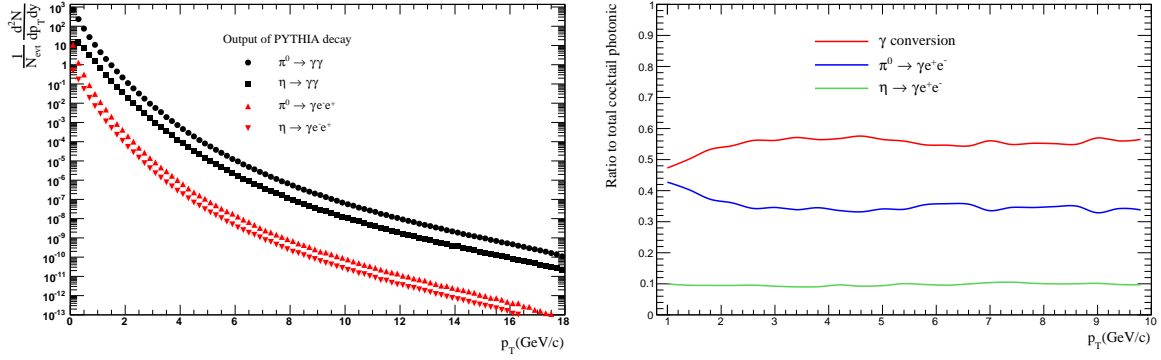


Figure 3.37.: (Color online) (Left) PYTHIA spectra. (Right) Cocktail relative contributions.

1. Input π^0 and m_T -scaled η from fits. No direct γ component in this cocktail simulation.
2. Decay π^0 and η to $e^+e^-\gamma$ in PYTHIA.
3. Decay π^0 and η to $\gamma\gamma$ in PYTHIA.
4. Normalize decayed distributions to dN/dy from integral of π^0 and η fits.
5. Cocktail spectra are calculated as per the following equations:

Dalitz decays:

$$\frac{dN}{dp_T}(p_T) = \frac{dN_{PYTHIA}^{e^\pm}}{dp_T} \times \epsilon_{eID} \times \frac{\text{reco. pairs} + \text{pair cuts} + \text{partner cuts}}{\text{all MC } e^\pm} \quad (3.8)$$

Gamma conversion:

$$\frac{dN}{dp_T}(p_T) = \frac{dN_{PYTHIA}^\gamma}{dp_T} \times \epsilon_{eID} \times \frac{\text{reco. pairs} + \text{pair cuts} + \text{partner cuts}}{\text{all MC } \gamma} \quad (3.9)$$

where ϵ_{eID} is the same electrons identification efficiency calculated from data. The last ratios were calculated from embedding weighted by the parent particle distribution as described in the photonic electron reconstruction efficiency section.

Fig.3.37 (Left) shows the e^\pm and γ distributions from PYTHIA. (Right) shows the relative contribution of conversion electrons and Dalitz decays to the total photonic electrons measured at STAR from the cocktail results.

Fig.3.38 shows cocktail photonic electrons spectra overlaid with the measured photonic electrons. Also shown is the ratio of measured photonic electrons to the cocktail. The error bands are only from varying the fits of pions by $\pm 1\sigma$ and repeating the whole procedure. Uncertainties from electron identification efficiency and embedding analysis were not included. So the error bands are underestimated. Since the cocktail has been done as a cross-check, we do not think these uncertainties are crucial, they are likely to widen the uncertainty band by a maximum of $\sim 50\%$ of the band itself. The cocktail is in general in good agreement with the measured photonic electrons spectra. The rise after $p_T \sim 3 \text{ GeV}/c$ is due to the missing direct- γ component in our cocktail which contributes to high- p_T conversion electrons [50].

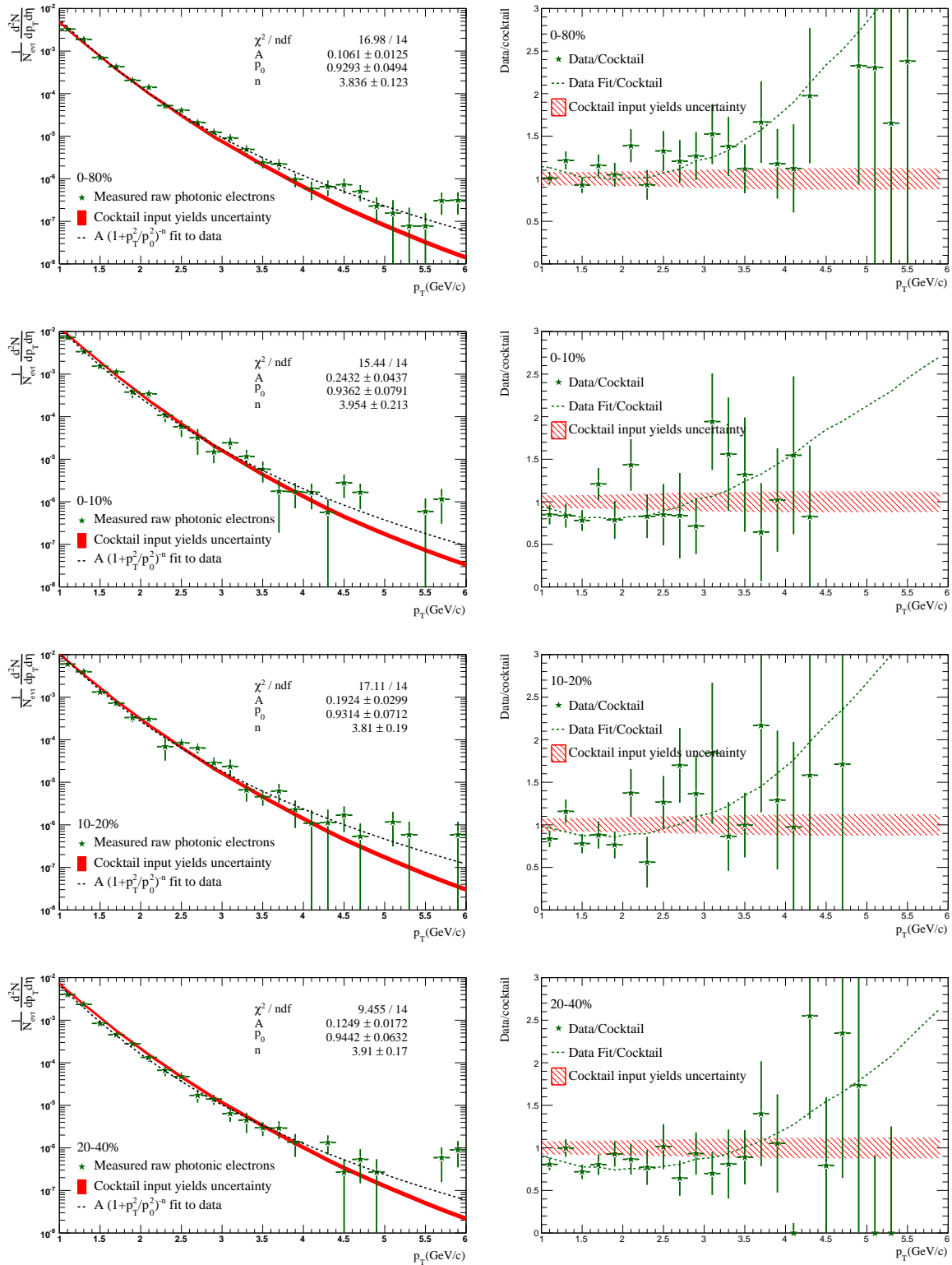


Figure 3.38.: (Color online) Comparison of measured photonic electrons to cocktail yields.

3.8 Spectra and systematic uncertainties

The final non-photonic electron invariant yield is calculated as per the following equation

$$\frac{1}{2\pi p_T} \frac{d^2 N}{dp_T d\eta} = \frac{1}{2\pi p_T \Delta p_T \Delta \eta} \frac{1}{\epsilon_{eID}(p_T) \epsilon_{trk}(p_T)} \left[N_{inc}(p_T) \epsilon_p(p_T) - \frac{N_{pho}(p_T)}{\epsilon_{pho}(p_T)} \right] \quad (3.10)$$

where ϵ_{eID} is electrons identification efficiency, ϵ_{trk} is the total single electrons reconstruction efficiency, ϵ_p is the inclusive electrons purity and ϵ_{pho} is the photonic electrons reconstruction efficiency.

The total systematic uncertainty on the invariant yield is the quadratic sum of the uncertainties of the uncertainties from ϵ_{eID} , ϵ_{trk} , ϵ_p and ϵ_{pho} . Statistical uncertainties are purely from data statistics, i.e. statistical errors from efficiencies and other corrections are added to the systematic errors.

Final spectra and non-photonic to photonic electrons ratio will be presented in chapter 4.

3.9 J/ψ contribution to non-photonic electrons

A major background contribution to the calculated non-photonic electrons comes from $J/\psi \rightarrow e^+e^-$ decays. To estimate this contribution we use the following algorithm:

1. Generate Monte-Carlo J/ψ particles with (p_T, y) sampled from measured or calculated J/ψ $d\sigma/dp_T$ and $d\sigma/dy$.
2. Simulate $J/\psi \rightarrow e^+e^-$ for generated particles using PYTHIA decay routine.
3. Fill η of generated e^\pm in histogram hElectronsEta.
4. Fill p_T of e^\pm generated within the desired $\Delta\eta$ acceptance in histogram hElectronsPt.

The exact normalization recipe depends on which spectra one uses to generate the original J/ψ . In the ideal case when one has both $d\sigma/dp_T$ and $d\sigma/dy$ of J/ψ

1. Integral of J/ψ $d\sigma/dy$ gives σ .
2. Normalize integral of histogram hElectronsEta to 2σ .
3. Integral of hElectronEta in the desired $\Delta\eta$ gives $\Delta\sigma$.
4. Normalize integral of hElectronsPt to $\Delta\sigma$.
5. Divide hElectronsPt by $\Delta\eta$ to get $d\sigma/dp_T d\eta$ of electrons from J/ψ .

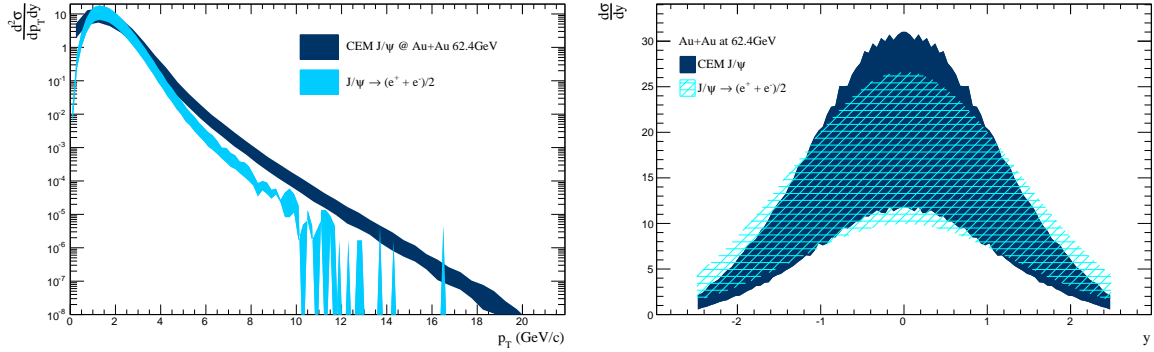


Figure 3.39.: (Left) J/ψ from CEM and electrons from $J/\psi \rightarrow e^+e^-$ PYTHIA decay. (Right) Rapidity distributions.

For non-photonic electron measurement at $\sqrt{s_{NN}} = 200$ GeV a similar algorithm has been applied and J/ψ distributions were taken from PHENIX and STAR measurements [81, 82].

For $\sqrt{s_{NN}} = 62.4$ GeV we use Color Evaporation Model (CEM) calculation [83]. Which has large uncertainties (Fig.3.39). A recent STAR measurement of J/ψ in $Au+Au$ collisions at this energy is limited to $0 < p_T < 4.0$ with four p_T bins only, which makes it very difficult to use this data for this study (Fig.3.40).

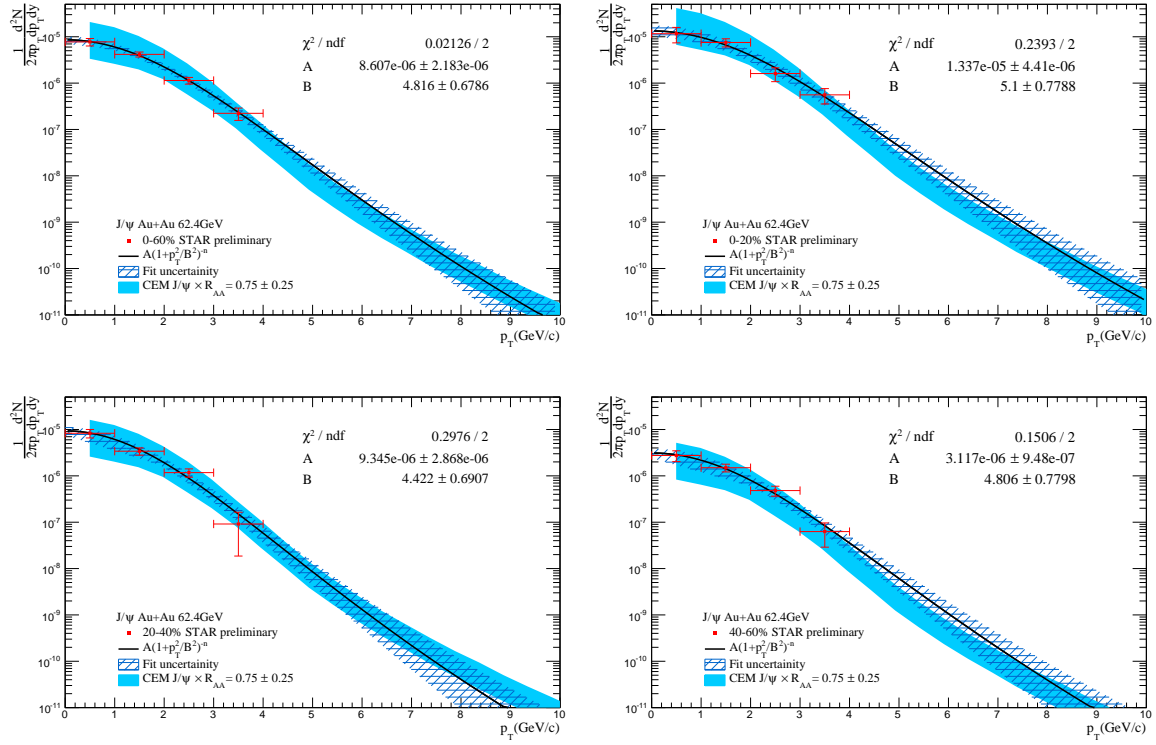


Figure 3.40.: CEM band scaled by N_{bin} and $R_{AA} = 0.75 \pm 0.25$ compared to STAR measurement of J/ψ in $Au+Au$ at $\sqrt{s_{NN}} = 62.4$ GeV [84].

Results using CEM spectra to estimate the J/ψ contribution to non-photonic electron are compared to predictions of non-photonic electrons in $p+p$ in collisions at $\sqrt{s} = 62.4$ GeV are shown in Fig.3.41.

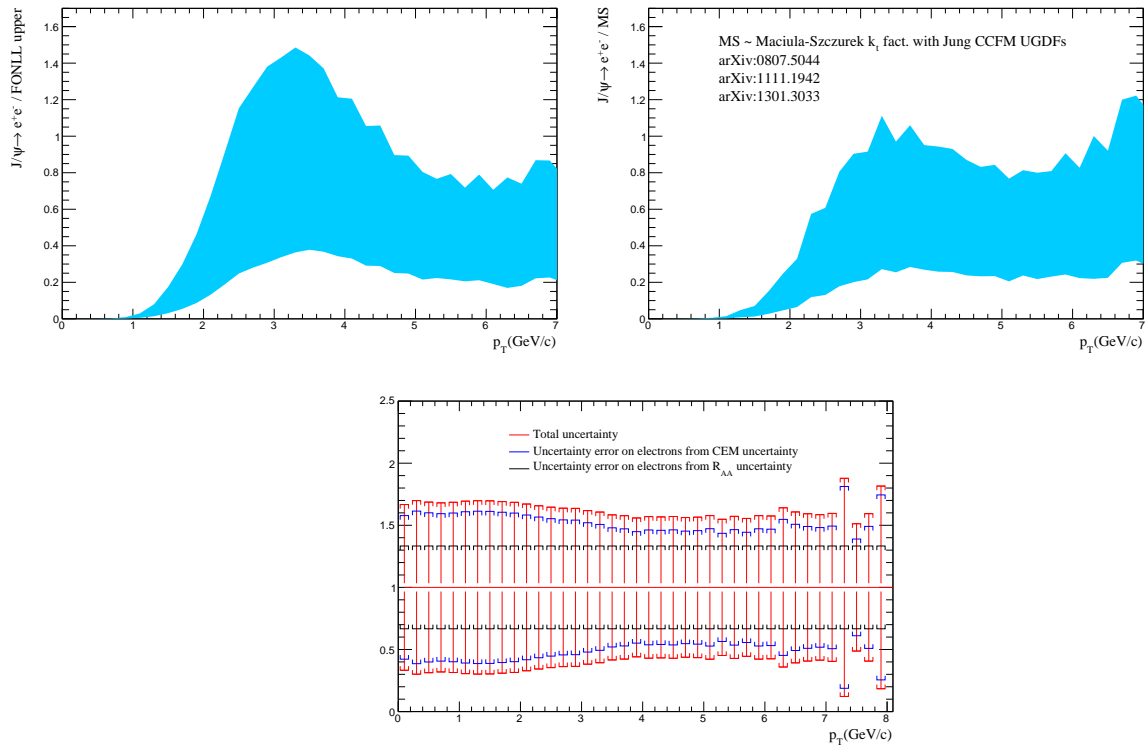


Figure 3.41.: Top two panels, uncertainty band of $J/\psi \rightarrow e^+e^-$ contribution to non-photon electron shown as ratio to $p+p$ theory prediction from FONLL (right) and from k_t factorization (left). Lower plot shows the break down of the uncertainty.

4. RESULTS AND DISCUSSION

4.1 Non-photonic electron spectra and azimuthal anisotropy at $\sqrt{s_{NN}} = 200$ GeV

Fig.4.1 shows the non-photonic to photonic electron ratio in at this center-of-mass collision energy for the top centrality (0–10%) and a peripheral centrality (40–60%).

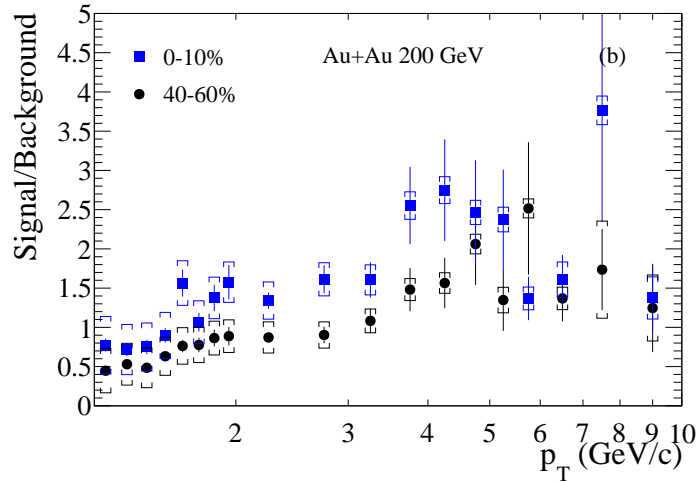


Figure 4.1.: Non-photonic electrons to photonic electrons ratio in $Au+Au$ collisions at $\sqrt{s_{NN}} = 200$ GeV. Error bars are statistical errors, and square brackets are point-by-point systematic uncertainties.

4.1.1 Non-photonic electron spectra and nuclear modification factor

Fig.4.2 shows our new measurement of NPE mid-rapidity differential invariant yield for $p_T = 1.5 - 10$ GeV/ c . The novelty of this measurement lies in the achieved high statistical precision. The large amount of statistics allows differentiating the measurements in five centrality bins, in addition to a 0 – 5% centrality bin from

a central trigger. With such a precision, and guided by the scaled FONLL upper bound, one can qualitatively notice the suppression of the yield in $Au+Au$ collisions compared to $p+p$ collisions despite the large log-scale spanned in the figure.

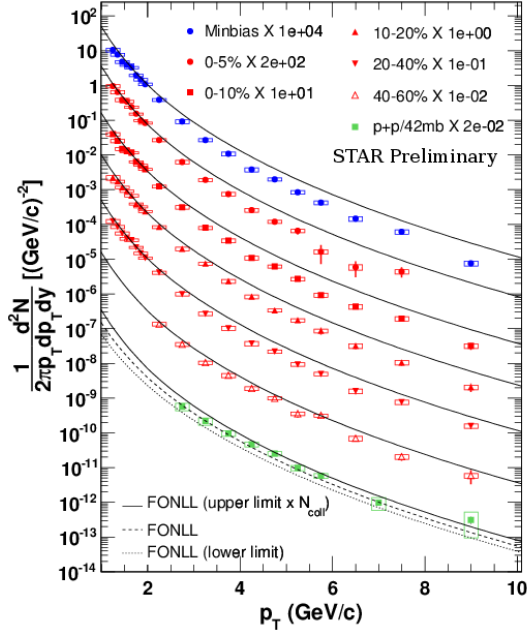


Figure 4.2.: (Color Online) Differential invariant yields vs. p_T of non-photonic electrons in $Au+Au$ at $\sqrt{s_{NN}} = 200$ GeV, and scaled STAR published $p+p$ [68]. Error bars and boxes are statistical and systematic errors, respectively. FONLL predictions are scaled by N_{coll} and shown as curves.

Fig. 4.3 shows the invariant yields over FONLL predictions. The dotted lines delineate the theoretical uncertainty band obtained by independently varying the factorization and normalization scales. Additional uncertainty is obtained by varying charm and bottom masses. The final uncertainty is the quadratic sum of all uncertainties [46]. The quality of the data and quenching of the heavy quark yields in presence of the sQGP are obvious in these plots. At first sight, one might think that it would make more sense to have theoretical predictions for the heavy quarks yield in $Au+Au$ collisions to compare directly to our measurement rather than resorting

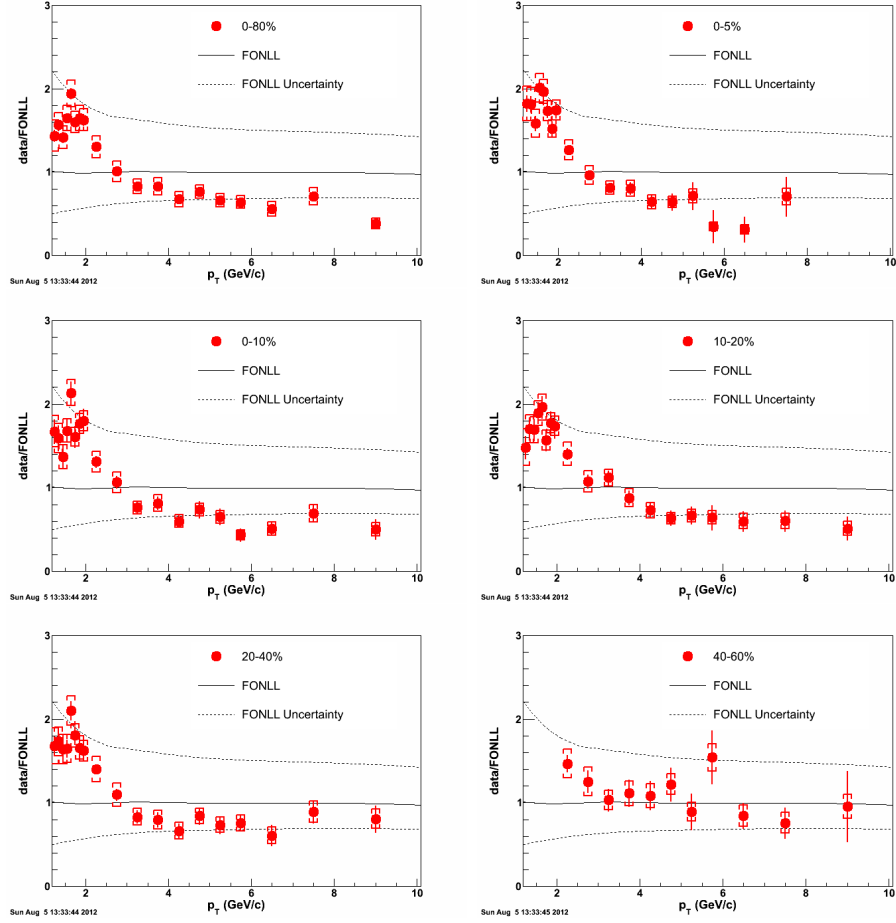


Figure 4.3.: (Color Online) Data over FONLL [46]. Bars and brackets are statistical and systematic errors, respectively.

to a nuclear modification factor, R_{AA} , whose precision is dependent on the quality of the baseline measurement. However, in all theory energy loss models, one first obtains heavy quark production in $p+p$ collisions using any of the different pQCD calculations, then use that as an input to the energy loss model framework. Then finally use the quenched output and the scaled $p+p$ input to calculate R_{AA} . Such schemes take advantage of the fact that most uncertainties of the input $p+p$ spectra are canceled out in the final R_{AA} curve. This renders the idea of comparing the experimental invariant yields directly to theory not readily possible.

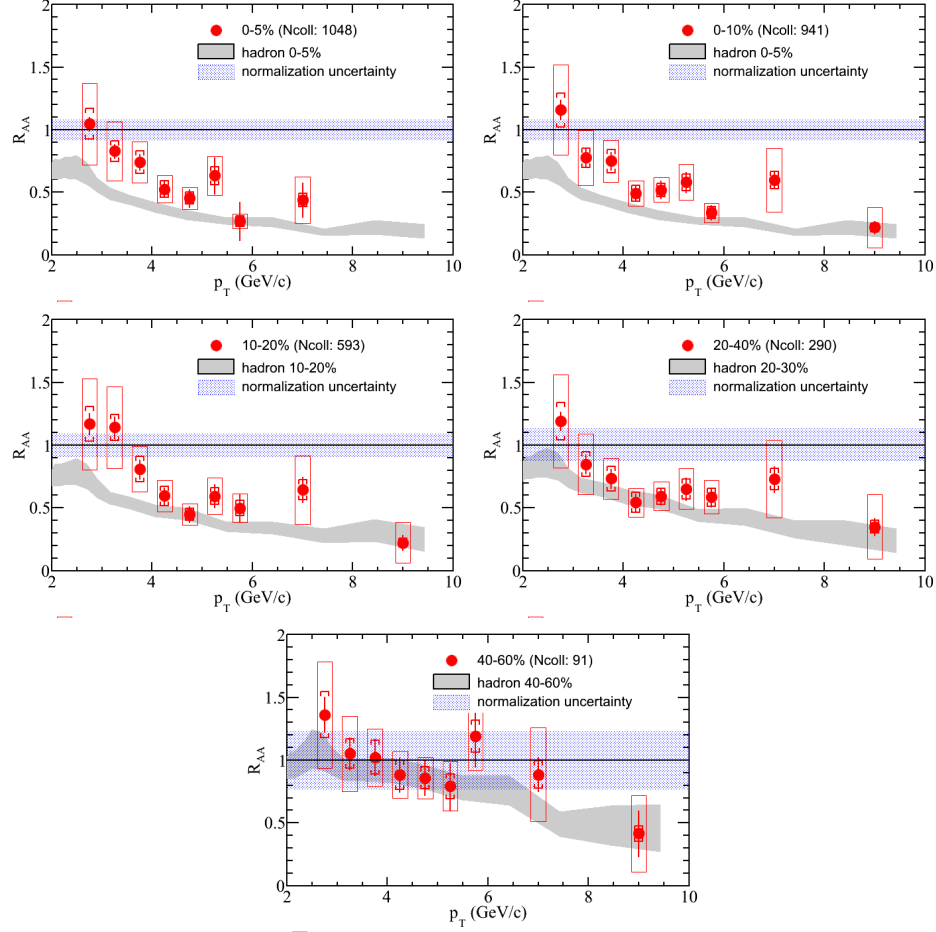


Figure 4.4.: (Color Online) Non-photonic electrons nuclear modification factor in $Au+Au$ collisions at $\sqrt{s_{NN}} = 200$ GeV in different centralities. Bars and brackets are statistical and systematic errors, respectively. Error boxes are the uncertainties from the $p+p$ baseline measurement.

Using STAR published non-photonic electron measurement $p+p$ [68], we calculate R_{AA} in most central (0 – 5%) to semi-peripheral (40 – 60%) centralities shown in Fig.4.4. Also charged hadron R_{AA} for values are plotted for comparison. The large uncertainty from our baseline $p+p$ measurement dominates the current overall uncertainty. Analysis of the large amount of collected high quality data from RHIC runs 2009 and 2012 is needed to improve the baseline precision. Within the current mea-

surement precision, one can see virtually no difference between the charged hadron and heavy quarks suppression in all presented centralities.

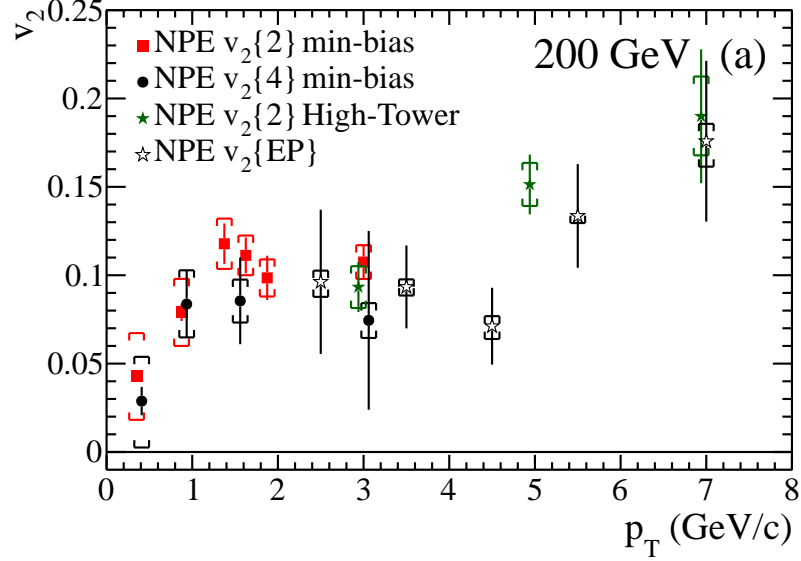


Figure 4.5.: (Color Online) (Left) Non-photonic electrons azimuthal anisotropy, $v_2\{2\}$, $v_2\{4\}$ and $v\{EP\}$ at $\sqrt{s_{NN}} = 200$ GeV. Bars and brackets are statistical and systematic errors, respectively.

4.1.2 Non-photonic electron azimuthal anisotropy

Fig.4.5 shows non-photonic electrons v_2 measurements from 2- and 4- particle correlations and event plane method, represented as $v_2\{2\}$, $v_2\{4\}$ and $v_2\{EP\}$ in $Au+Au$ collisions at $\sqrt{s_{NN}} = 200$ GeV. The $v_2\{EP\}$ is an independent study by Wenqin Xu from UCLA using the same data set at STAR [81], we show it here to show the robustness of the steep increase feature seen in v_2 at high- p_T . The $v_2\{2\}$ and $v_2\{EP\}$ measurements are consistent with each other for $p_T > 3$ GeV/c. While both show a pronounced systematic increase in v_2 towards high p_T , at this point we cannot distinguish whether this rise is due to jet-like correlations unrelated to the reaction plane or due to the path length dependence of partonic energy loss. For p_T

$< 3 \text{ GeV}/c$ we show both $v_2\{2\}$ and $v_2\{4\}$. In $v_2\{4\}$ the non-flow contribution is negligible and the flow fluctuation contribution is negative, hence providing a lower bound on the v_2 of non-photonics electrons. Both v_2 measurements are finite, which might hint at a non-negligible charm-medium interaction at $\sqrt{s_{NN}} = 200 \text{ GeV}$.

4.1.3 Azimuthal anisotropy and nuclear modification factor comparison to models

Fig.4.6 upper panel shows non-photonics electrons R_{AA} in $0 - 10\%$ centrality compared to a collection of models of different energy loss mechanisms. As we see in the Figure, despite its success at describing the suppression of light hadrons [85], gluon radiation alone (line in dashed green) fails to explain the observed large suppression at high p_T . Including elastic collisional energy loss in the DGLV added a further suppression of the yield (line in solid green), but the best agreement between the measurement and radiative + collisional energy loss comes after improving the DGLV model to account for recoiling scattering centers and a running coupling constant. The model is provided by the same DGLV group and dubbed CUJET 1.0 (line in dashed black) [86].

A note is in order here, many recent calculations of radiative and collisional energy loss differ drastically from the earlier calculations. The relative contributions of these two mechanisms is highly debated [89–93]. Including a running coupling constant enhances the contribution of elastic energy loss [89, 90, 93]. Energy loss in a Langevin-equation framework has been studied in [92], where they also incorporated radiative energy loss in the equation, and in their work they find that gluon radiation is significant and should no longer be dismissed on the grounds of the dead-cone effect. It is also not clear if the LPM interference effect is of importance to heavy quarks [91, 93]. Furthermore, radiative energy loss using generalized gluon emission spectrum has been calculated recently in [91] where they conclude that energetic heavy and light quarks radiate gluons similarly and mass suppression of the dead-cone effect

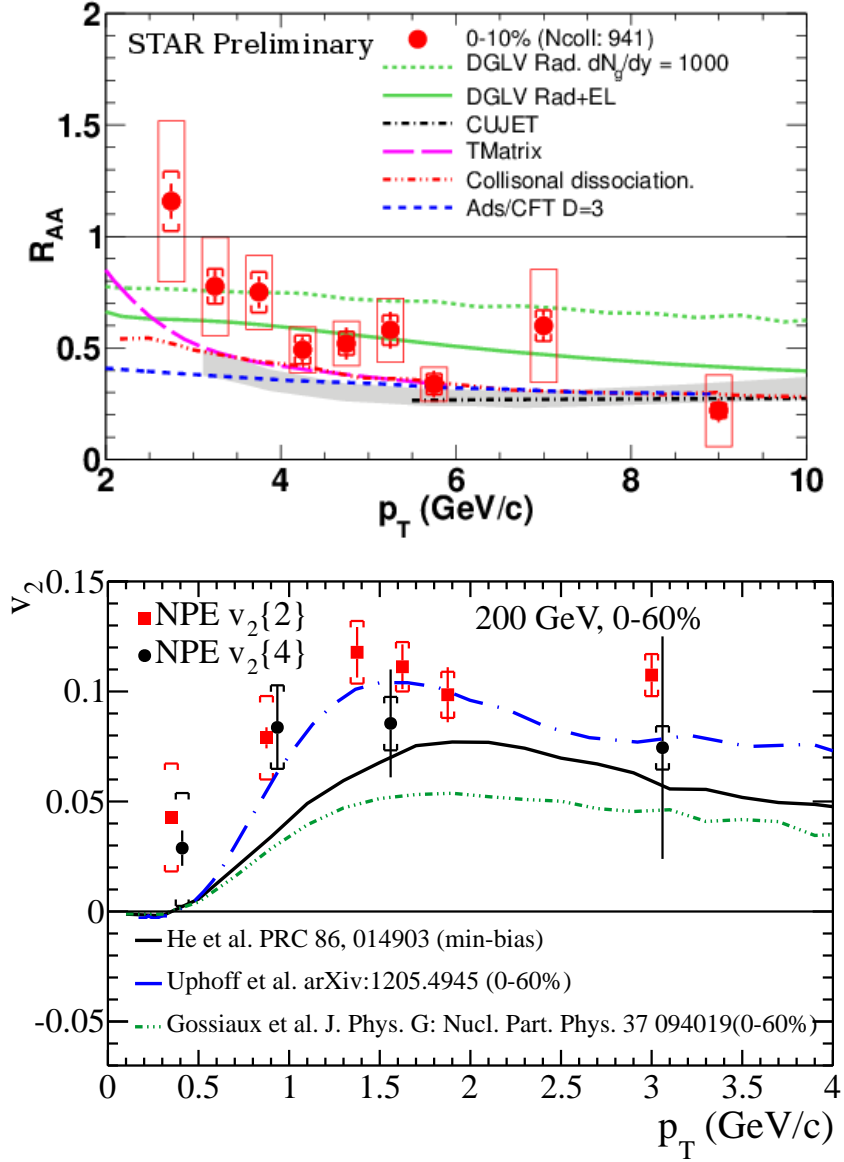


Figure 4.6.: (Color Online) (Top) Non-photonic electrons nuclear modification factor, R_{AA} , at $\sqrt{s_{NN}} = 200$ GeV compared to models [85–88]. Grey band is light hadrons R_{AA} . Error bars and brackets are Au+Au statistical and systematic errors, respectively. Error boxes are the uncertainties from our baseline $p + p$ measurement. (Bottom) Non-photonic electrons azimuthal anisotropy compared to models.

is relevant only when the quark energy is in the same order as the mass. In light of these different theoretical results, it is too early to favor a certain mechanism and conclude which is the correct energy loss mechanism for heavy quarks. More systematic checks and comparisons to differential measurements at the different energies are imperative.

Motivated by lattice QCD calculations of heavy quarks potentials which show that these potentials are strong enough to support heavy quark resonances in the medium at temperatures on the order of $1.5T_c$ (T_c is the critical temperature marking the transition to the QGP phase), Ian Vitev and his group implemented a collisional energy loss model [87]. In this model the energy loss is due to heavy quarks fragmenting into heavy mesons and heavy mesons dissociating into heavy quarks, both processes happening in the medium. It is interesting that in this approach charm and bottom are equally suppressed.

To study the energy loss in the strong coupling limit AdS/CFT correspondence could also be invoked [88]. A unique feature of this approach is that energy loss is proportional to L^3 as opposed to the L^2 dependence obtained when including LPM effect in pQCD calculations, or L dependence when gluon radiation off the heavy quarks is incoherent. Recent high-precision measurement by PHENIX of π^0 suppression in-plane and out-of-plane shows an interesting agreement with AdS/CFT energy loss path length dependence [94]. Curve from AdS/CFT is shown in dashed blue in the Fig.4.6, it does agree with our measurement. However, it over-quenches ALICE D mesons R_{AA} measurement in $Pb+Pb$ collisions at $\sqrt{s_{NN}} = 2.76$ TeV [95].

An improved version of the partonic transport model, BAMPS, is provided by Uphoff et al. [96, 97]. In this model heavy quarks lose energy by collisional energy loss with rest of the medium. To account for radiative energy loss which is not implemented in this model, the heavy quarks scattering cross-section is scaled up by a phenomenological factor, $K = 3.5$. The v_2 curve from this model is shown in a dashed blue line in the lower panel of Fig.4.6. One can see that this model is the closest to our data points. The R_{AA} curve from this model is not shown because

we do not have it at the moment. In Uphoff et al. paper [96] they show a good description of PHENIX R_{AA} non-photonic electrons measurement. In Fig.4.6 lower panel, the dashed green line is from P. Gossiaux group implementation of radiative and collisional energy loss. Despite the models success at accounting for the R_{AA} (not shown), it under-predicts our v_2 data points.

In contrast to the perturbative approach of the radiative, collisional and collisional dissociation energy loss models, TAMU group implement the nonperturbative resonance scattering *T-matrix* interactions model [98, 99]. In this model heavy quark resonances form in the medium at temperatures of $1.5T_c$ and scatter off the light quarks in the medium. While this model is successful at describing the R_{AA} (shown in dashed pink), it misses our $v_2\{2\}$ data points by roughly 2σ (line shown in solid black). However, as is clear from the $v_2\{4\}$ data points, more control over non-flow contributions might provide a better insight on the success of this model.

For a hadronization mechanism of heavy quarks, which are particularly important for v_2 , M.He et al. and P.Gossiaux et al. both utilize a coalescence approach in the shown p_T range. While in Uphoff et al. BAMPS model heavy quarks fragment into mesons. This is indeed interesting; coalescence is expected to give more flow to the mesons due to the contribution of the light quarks they combine with, still Uphoff fragmentation mechanism is in better agreement with our data points. Of course this might be a superficial observation, since we are comparing completely different energy loss models and implementations here. Finally, all models seem to miss our lowest data point, which itself has large systematic error (the error on this point is due to the low signal to background ratio). With the current location of this data point it is in agreement with light hadrons elliptic flow.

4.2 Non-photonic electron spectra and azimuthal anisotropy at $\sqrt{s_{NN}} = 39$ and 62.4 GeV

4.2.1 Non-photonic electron spectra

Fig. 4.7 shows the non-photonic to photonic electron ratio in minimum-bias $Au+Au$ collisions at $\sqrt{s_{NN}} = 62.4$ GeV. The ratio demonstrates the feasibility of a non-photonic electron study at this energy at STAR.

Before we move to comparisons to theory predictions, it is imperative to remind ourselves that $J/\psi \rightarrow e^+e^-$ contributions are not subtracted from our non-photonic electrons results; large uncertainty from CEM calculations and high- p_T measurement of J/ψ is lacking at this energy. J/ψ contributes 15 – 20% of measured non-photonic electrons at $\sqrt{s_{NN}} = 200$ GeV [81], charm cross-section is an order of magnitude lower at $\sqrt{s_{NN}} = 62.4$ GeV, and its decay electron transverse momenta are softer compared to electrons from J/ψ whose mass hardens the spectra of its decay electrons, so we expect a minimum contribution of J/ψ that is the same as at $\sqrt{s_{NN}} = 200$ GeV, if not more.

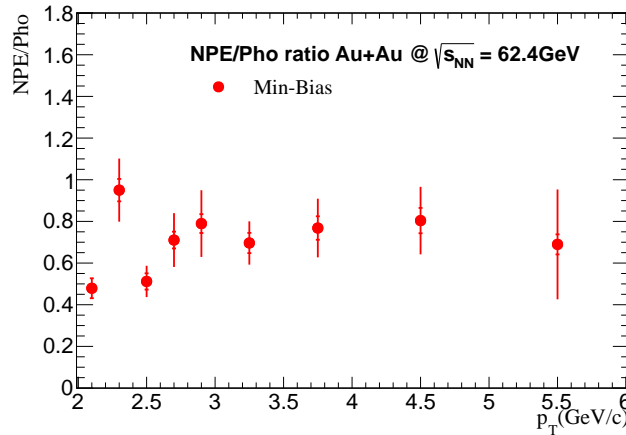


Figure 4.7.: Non-photonic electrons to photonic electrons ratio in 0 – 80% centrality $Au+Au$ collisions at $\sqrt{s_{NN}} = 62.4$ GeV.

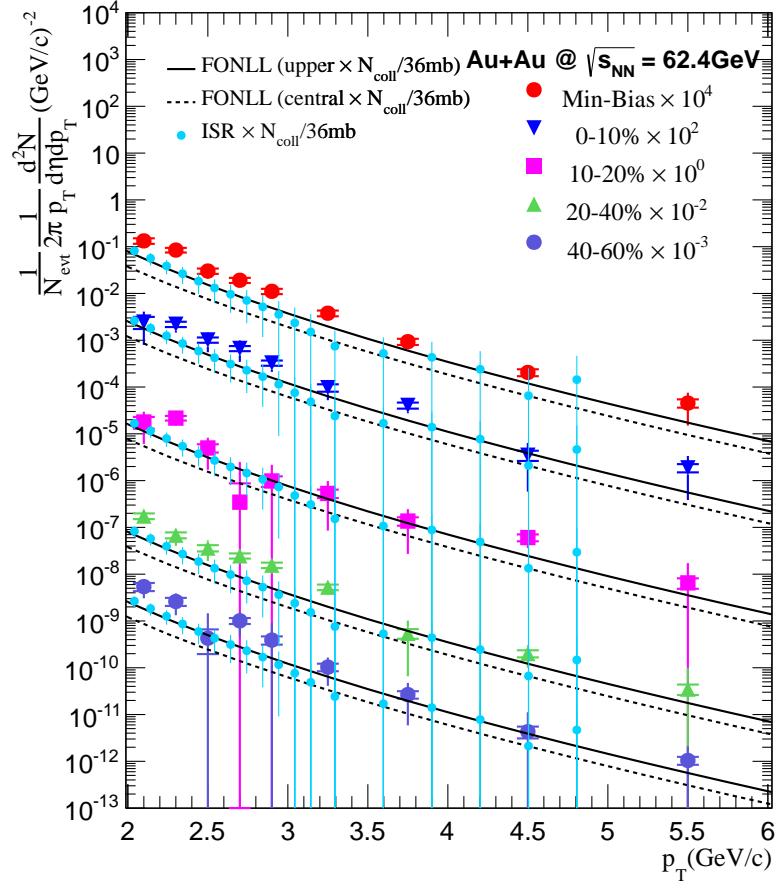


Figure 4.8.: (Color Online) Differential invariant yields vs. p_T of non-photonic electrons in $Au+Au$ collisions at $\sqrt{s_{NN}} = 62.4$ GeV. Bars and brackets are statistical and systematic errors, respectively. Measurement at ISR in $p+p$ collisions at $\sqrt{s_{NN}} = 62.2$ GeV scaled by N_{coll} is also plotted [100]. FONLL predictions are scaled by N_{coll} and shown as curves.

Fig.4.8 shows differential invariant yields together with scaled Fixed-Order-Next-to-Leading-Log (FONLL) calculation prediction [priv. comm.] [46]. While a previous measurement of non-photonic electrons in $p+p$ collisions at $\sqrt{s} = 62.2$ GeV at the Intersecting Storage Rings (ISR), CERN [100], seems to agree with FONLL upper-band as shown in the figure, our measurement is systematically higher than both. Fig.4.10

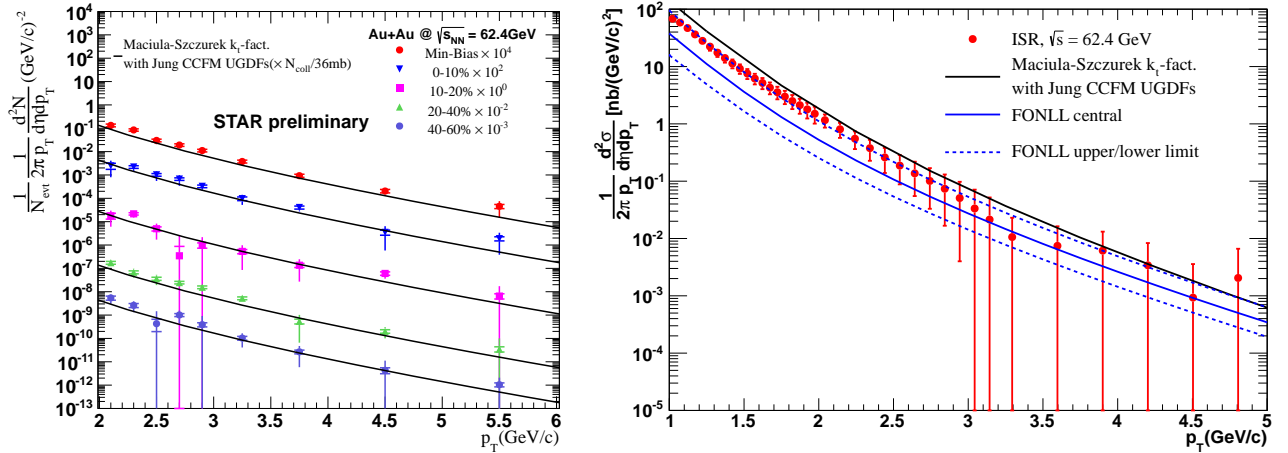


Figure 4.9.: (Color Online) (Left) Differential invariant yields vs. p_T of non-photonic electrons in $Au+Au$ collisions at $\sqrt{s_{NN}} = 62.4$ GeV. Bars and brackets are statistical and systematics errors, respectively. k_t -fact. spectra is scaled by N_{coll} and shown as curves. (Right) Comparison of ISR measurement, FONLL and k_t -fact. predictions for non-photonic electrons invariant cross-section in $p+p$ collisions at $\sqrt{s_{NN}} = 62.4$ GeV.

(Left) compares our minimum-bias measurement to FONLL ratio to the FONLL uncertainty band. We also compare our measurement to another pQCD calculation that uses the k_t -factorization approach [101, 102] which uses Unintegrated Gluon Distribution Functions (UGDFs) from [103]. The gluon emission in this approach is encoded in the UGDFs which also includes higher order contributions. The k_t -factorization approach seems to describe our data better (Fig.4.9 Left), also see its ratio to the minimum-bias measured spectra in Fig.4.10. Fig.4.9 right shows a comparison of ISR measurement, to FONLL and k_t -factorization predictions.

One more effect on our measurement which we hope to understand in the near future is the Cronin enhancement. PHENIX has recently published their measurement of non-photonic electrons in $d+Au$ collisions at $\sqrt{s_{NN}} = 200$ GeV where they see a 20 – 40% enhancement in the region ($2.0 < p_T < 6.0$) GeV/ c compared to the spectra in $p+p$ collisions, this enhancement is likely due to Cronin effect. Cronin

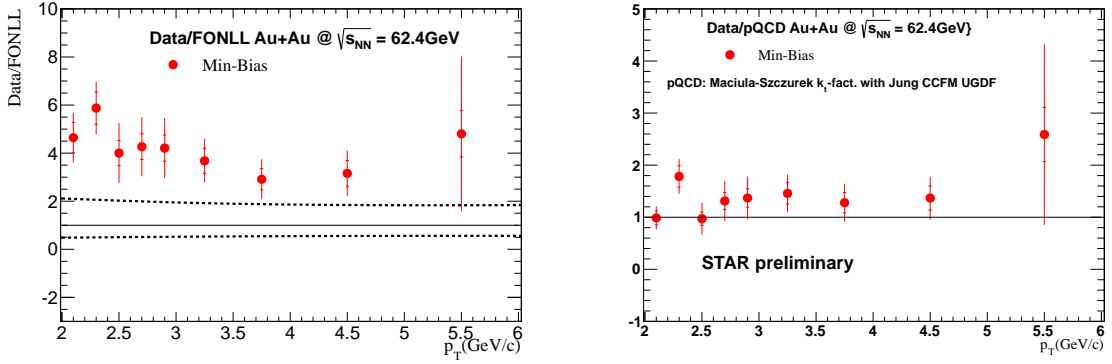


Figure 4.10.: Non-photonic electrons spectra over N_{bin} scaled FONLL prediction compared to FONLL uncertainty band (Left), N_{bin} scaled k_t -factorization prediction (Right).

enhancement is, in general, higher at lower center-of-mass collision energies [43, 104], this is due to the softer p_T spectra at lower energies.

We are currently unable to quantify or infer any clear suppression effects on non-photonic electrons at this center-of-mass energy ($\sqrt{s_{NN}} = 62.4$ GeV).

Fig.4.11 shows the measured inclusive and photonic electron raw spectra in minimum-bias $Au+Au$ collisions at $\sqrt{s_{NN}} = 39$ GeV. Simulations and final corrections are being finalized. The figure shows that the statistics are reasonable to extract the yield in a narrow transverse momentum range ($1.5 < p_T < 3.0$) GeV/ c .

4.3 Non-photonic electron azimuthal anisotropy

Measurement of $v_2\{2\}$ at lower energies shown in Fig.4.12 seem to be consistent within errors with v_2 measured at $\sqrt{s_{NN}} = 200$ GeV for $p_T > 1.0$ GeV/ c . The results for data points at $p_T < 1.0$ GeV/ c seem to hint at a milder charm-medium interaction compared to those at $\sqrt{s_{NN}} = 200$ GeV, but it is difficult to stress the significance of such an observation with the large systematical uncertainties on these data points.

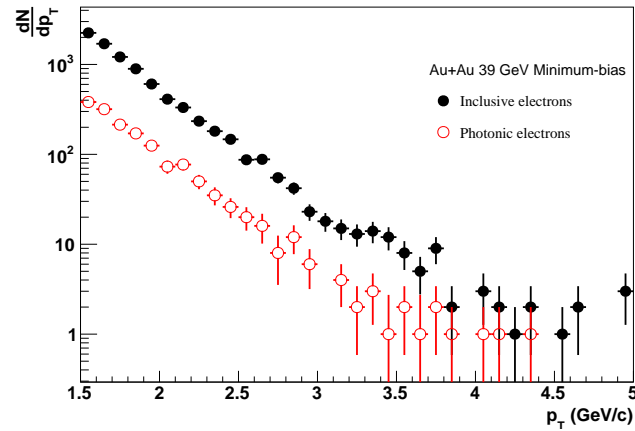


Figure 4.11.: (Color Online) Uncorrected inclusive and photonic electron distributions measured in minimum-bias $Au+Au$ collisions at $\sqrt{s_{NN}} = 39$ GeV.

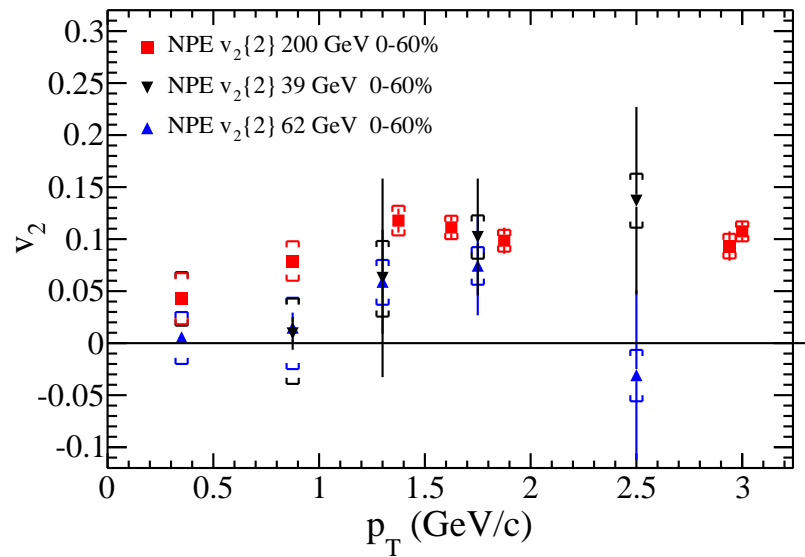


Figure 4.12.: (Color Online) v_2 from two-particle correlations at $\sqrt{s_{NN}} = 39$ and 62.4 GeV compared to $\sqrt{s_{NN}} = 200$ GeV. Bars and brackets are statistical and systematic errors, respectively.

5. SUMMARY

We have presented a measurement of electrons from heavy flavor hadrons decay (non-photonic electrons) in $Au+Au$ collisions at $\sqrt{s_{NN}} = 62.4$ GeV center-of-mass collision energy in STAR experiment. The lack of a reliable $p+p$ baseline prevents us from calculating nuclear modification factor at the moment. Also, uncertainties from the contribution of $J/\psi \rightarrow e^+e^-$ to our measurement are still large due to the lack of high transverse momentum measurement at this energy. Understanding the beam-energy dependence of Cronin enhancement is imperative to interpret the data.

A new measurement of non-photonic electrons in $Au+Au$ at $\sqrt{s_{NN}} = 200$ GeV has been presented, the statistical precision in this measurement is highly improved. This measurement will serve in future efforts to separate bottom and charm energy loss once the latter has been measured using direct topological reconstruction of secondary vertices.

We have also presented a re-calculated nuclear modification factor R_{AA} at $\sqrt{s_{NN}} = 200$ GeV which has been compared to several energy loss models. Improvement of the baseline from $p+p$ will improve the precision of this R_{AA} . Comparison to models rules out the early calculated radiative energy loss models which incorporates mass suppression of gluon radiation (dead-cone) effect. More recent theory calculations of radiative and elastic energy loss have a drastic difference, systematic studies and comparison of the different calculations are imperative to understand the role of the different energy loss mechanisms for heavy-quarks.

Measurement of non-photonic electrons azimuthal anisotropy $\sqrt{s_{NN}} = 200$ GeV is finite at low transverse momentum ($p_T < 1.0$) which indicates a strong charm-medium interaction at this energy. At higher transverse momentum is measurement is finite and has a possible jet-like correlation which manifests itself in a systematic

increase in v_2 . Path length dependence of energy loss might also contribute to this observation.

Measurement of non-photonic electrons azimuthal anisotropy at $\sqrt{s_{NN}} = 39$ and 62.4 GeV is comparable within errors with that at $\sqrt{s_{NN}} = 200$ GeV.

LIST OF REFERENCES

LIST OF REFERENCES

- [1] J. Adams *et al.* (STAR Collaboration), *Nucl. Phys. A* **757**, 102 (2005), [nucl-ex/0501009](#) .
- [2] K. Adcox *et al.* (PHENIX Collaboration), *Nucl. Phys. A* **757**, 184 (2005), [nucl-ex/0410003](#) .
- [3] I. Arsene *et al.* (BRAHMS Collaboration), *Nucl. Phys. A* **757**, 1 (2005), [nucl-ex/0410020](#) .
- [4] B. B. Back *et al.* (PHOBOS Collaboration), *Nucl. Phys. A* **757**, 28 (2005), [nucl-ex/0410022](#) .
- [5] D. J. Gross, *Rev. Mod. Phys.* **77**, 837 (2005).
- [6] M. Gell-Mann, *Phys. Lett.* **8**, 214 (1964).
- [7] G. Zweig, *CERN Reports CERN-TH-401*, 24 (1964).
- [8] G. Zweig, *CERN Reports CERN-TH-412*, 80 (1964).
- [9] W. A. Bardeen, H. Fritzsch, and M. Gell-Mann, preprint (2002), [arXiv:hep-ph/0211388](#) .
- [10] M. Peskin and D. Schroeder, *An Introduction to Quantum Field Theory* (Westview, 1995).
- [11] J. Beringer *et al.* (Particle Data Group), *Phys. Rev. D* **86**, 010001 (2012).
- [12] F. Wilczek, *Phys. Today* **53**, 22 (2000).
- [13] “Millenium prize problems,” .
- [14] R. Gupta, preprint (1998), [arXiv:hep-lat/9807028](#) .
- [15] A. H. Mueller, *Phys. Rep.* **73**, 237 (1981).
- [16] R. J. Fries and C. Nonaka, *Prog. Part. Nucl. Phys.* **66**, 607 (2011), [arXiv:1012.1881](#) .
- [17] S. Brodsky *et al.*, *Ann. Rev. Nucl. Part. Sci.* **62**, 1 (2012), <http://arxiv.org/abs/1302.5684> .
- [18] E. Iancu, preprint (2012), [arXiv:1205.0579](#) .
- [19] M. A. Stephanov, preprint (2006), [arXiv:hep-lat/0701002](#) .
- [20] P. Petreczky, *J. Phys. G: Nucl. Part. Phys.* **39**, 093002 (2012), [arXiv:1203.5320](#) .
- [21] Y. Aoki *et al.*, *Nature* **443**, 675 (2006), [arXiv:hep-lat/0611014](#) .
- [22] A. Bazavov, preprint (2013), [arXiv:1303.6294](#) .
- [23] R. Singh *et al.*, preprint (2013), [arXiv:1304.2969](#) .
- [24] G. Martinez, preprint (2013), [arXiv:1304.1452](#) .
- [25] CMS (CMS Collaboration), preprint (2012), [arXiv:1210.5482](#) .
- [26] CMS (CMS Collaboration), preprint (2013), [arXiv:1305.0609](#) .
- [27] E. Iancu and R. Venugopalan, preprint (2003), [arXiv:hep-ph/0303204](#) .
- [28] P. K. Kovtun, D. T. Son, and A. O. Starinets, *Phys. Rev. Lett.* **94**, 111601 (2005), [arXiv:hep-th/0405231](#) .
- [29] P. Jacobs and X.-N. Wang, *Prog. Part. Nucl. Phys.* **54**, 443 (2005), [arXiv:hep-ph/0405125](#) .

- [30] D. Kharzeev and M. Nardi, *Phys. Lett. B* **507**, 121 (2001), [arXiv:nucl-th/0012025](#) .
- [31] B. I. Abelev *et al.* (STAR Collaboration), *Phys. Rev. C* **81**, 024911 (2010), [arXiv:0909.4131](#) .
- [32] I. G. Bearden *et al.* (BRAHMS Collaboration), *Phys. Rev. Lett.* **93**, 102301 (2004), [arXiv:nucl-ex/0312023](#) .
- [33] A. Andronic *et al.*, *Nucl. Phys. A* **904–905**, 535 (2013), [arXiv:1210.7724](#) .
- [34] B. Müller, *Nucl. Phys. A* **750**, 84 (2005), [nucl-th/0404015](#) .
- [35] C. GALE, S. JEON, and B. SCHENKE, *Internatl. J. Mod. Phys. A* **28**, 1340011 (2013), [arXiv:1301.5893](#) .
- [36] U. W. Heinz and R. Snellings, *Ann. Rev. Nucl. Part. Sci.* **63** (2013), 10.1146/annurev-nucl-102212-170540, [arXiv:1301.2826](#) .
- [37] B. Müller, preprint (2008), [arXiv:0811.2979](#) .
- [38] S. Voloshin and Y. Zhang, *Z. Phys. C* **C70**, 665 (1996), [hep-ph/9407282](#) .
- [39] T. Renk, preprint (2010), [arXiv:1012.0186](#) .
- [40] H. Niemi *et al.*, *Phys. Rev. C* **87**, 054901 (2013), [arXiv:1212.1008](#) .
- [41] B. B. Back *et al.* (PHOBOS Collaboration), *Phys. Rev. Lett.* **91**, 072302 (2003), [arXiv:nucl-ex/0306025](#) .
- [42] J. Adams *et al.* (STAR Collaboration), *Phys. Rev. Lett.* **91**, 072304 (2003), [arXiv:nucl-ex/0306024](#) .
- [43] I. Vitev and M. Gyulassy, *Phys. Rev. Lett.* **89**, 252301 (2002), [arXiv:hep-ph/0209161](#) .
- [44] S. Chatrchyan *et al.* (CMS Collaboration), *Euro. Phys. J. C* **72**, 1 (2012), [arXiv:1202.2554](#) .
- [45] E. Sangaline (for STAR Collaboration), *Nucl. Phys. A* **904–905**, 771 (2013).
- [46] M. Cacciari *et al.*, *Phys. Rev. Lett.* **95**, 122001 (2005), [hep-ph/0502203](#) .
- [47] L. Adamczyk *et al.* (STAR Collaboration), *Phys. Rev. D* **86**, 072013 (2012), [arXiv:1204.4244](#) .
- [48] P. Lévai, B. Müller, and X.-N. Wang, *Phys. Rev. C* **51**, 3326 (1995), [hep-ph/9412352](#) .
- [49] P. Lévai and R. Vogt, *Phys. Rev. C* **56**, 2707 (1997), [hep-ph/9704360](#) .
- [50] A. Adare *et al.* (PHENIX Collaboration), *Phys. Rev. C* **84**, 044905 (2011), [arXiv:1005.1627](#) .
- [51] B. I. Abelev *et al.* (STAR Collaboration), *Phys. Rev. Lett.* **106**, 159902 (2011), [arXiv:nucl-ex/0607012](#) .
- [52] A. D. Frawley, T. Ullrich, and R. Vogt, *Phys. Rep.* **462**, 125 (2008), [arXiv:0806.1013](#) .
- [53] A. Majumder and M. v. Leeuwen, *Prog. Part. Nucl. Phys.* **66**, 41 (2011), [arXiv:1002.2206](#) .
- [54] Y. L. Dokshitzer and D. E. Kharzeev, *Phys. Lett. B* **519**, 199 (2001), [arXiv:hep-ph/0106202](#) .
- [55] L. Adamczyk *et al.* (STAR Collaboration), preprint (2012), [arXiv:1212.3304](#) .
- [56] M. Harrison, T. Ludlam, and S. Ozaki, *Nucl. Inst. & Meth. A* **499**, 235 (2003).
- [57] M. Harrison, S. Peggs, and T. Roser, *Ann. Rev. Nucl. Part. Sci.* **52**, 425 (2002).
- [58] “Rhic run overview,” .
- [59] E. C. Aschenauer *et al.*, preprint (2013), [arXiv:1304.0079](#) .
- [60] A. Accardi *et al.*, preprint (2012), [arXiv:1212.1701](#) .

- [61] K. H. Ackermann *et al.*, *Nucl. Inst. & Meth. A* **499**, 624 (2003).
- [62] M. Anderson *et al.*, *Nucl. Inst. & Meth. A* **499**, 659 (2003), [nucl-ex/0301015](#) .
- [63] M. Beddo *et al.*, *Nucl. Inst. & Meth. A* **499**, 725 (2003).
- [64] “Star TOF proposal,” .
- [65] W. J. Llope, *Nucl. Inst. & Meth. A* **661**, **Supplement 1**, (2012).
- [66] H. Bichsel, *Nucl. Inst. & Meth. A* **562**, 154 (2006).
- [67] S. S. Adler *et al.* (PHENIX Collaboration), *Phys. Rev. Lett.* **94**, 082301 (2005), [nucl-ex/0409028](#) .
- [68] H. Agakishiev *et al.* (STAR Collaboration), *Phys. Rev. D* **83**, 052006 (2011), [arXiv:1102.2611](#) .
- [69] H. Masui and A. Schmah, “Strefmultcorr,” (2011).
- [70] Y. Xu *et al.*, *Nucl. Inst. & Meth. A* **614**, 28 (2010).
- [71] B. I. Abelev *et al.* (STAR Collaboration), *Phys. Rev. C* **81**, 064904 (2010), [arXiv:0912.3838](#) .
- [72] O. Grebenyuk, *Neutral meson production in d+Au and p+p collisions at $\sqrt{s_{NN}} = 200$ GeV in STAR*, Ph.D. thesis, Utrecht University, Netherlands. (2009), [arXiv:0909.3006](#) .
- [73] “Single electrons and positrons embedding PWQ QA,” STAR protected document.
- [74] “GEANT,” ”Simulation software designed to describe the passage of elementary particles through matter.”.
- [75] N. M. Kroll and W. Wada, *Phys. Rev.* **98**, 1355 (1955).
- [76] R. Arnaldi *et al.* (NA60 Collaboration), *Phys. Lett. B* **677**, 260 (2009), [arXiv:0902.2547](#) .
- [77] T. Sjöstrand, S. Mrenna, and P. Skands, *J. High Energy Phys.* **2006**, 026 (2006), [arXiv:hep-ph/0603175](#) .
- [78] “Gamma, pi0 and eta embedding qa.” STAR protected document.
- [79] B. I. Abelev *et al.* (STAR Collaboration), *Phys. Lett. B* **655**, 104 (2007), [arXiv:nucl-ex/0703040](#) .
- [80] A. Adare *et al.* (PHENIX Collaboration), *Phys. Rev. Lett.* **109**, 152301 (2012), [arXiv:1204.1526](#) .
- [81] W. Xu, *Non-Photonic Electron at High Transverse Momentum in Au+Au Collisions and Bottom Quark Production in p+p Collisions at $\sqrt{s_{NN}} = 200$ GeV*, Ph.D. thesis, UC Los Angeles (2012).
- [82] T. Ullrich, “Study of the contribution of j/psi decay electrons to the npe yield measured,” STAR protected document.
- [83] R. E. Nelson, R. Vogt, and A. D. Frawley, *Phys. Rev. C* **87**, 014908 (2013), [arXiv:1210.4610](#) .
- [84] W. Zha (for STAR Collaboration), preprint [WWND 13 proceedings](#) .
- [85] M. Djordjevic and M. Gyulassy, *Nucl. Phys. A* **733**, 265 (2004), [nucl-th/0310076](#) .
- [86] A. Buzzatti and M. Gyulassy, preprint (2012), [arXiv:1207.6020](#) .
- [87] R. Sharma, I. Vitev, and B.-W. Zhang, *Phys. Rev. C* **80**, 054902 (2009), [arXiv:0904.0032](#) .
- [88] W. A. Horowitz, *Probing the Frontiers of QCD*, Ph.D. thesis (2010), [arXiv:1011.4316](#) .
- [89] A. Peshier, *Phys. Rev. Lett.* **97**, 212301 (2006), [arXiv:hep-ph/0605294](#) .

- [90] A. Peshier, *Phys. Rev. C* **75**, 034906 (2007), [arXiv:hep-ph/0607299](#) .
- [91] R. Abir *et al.*, preprint (2012), [arXiv:1203.5221](#) .
- [92] S. Cao *et al.*, *Nucl. Phys. A* **904–905**, 653 (2013), [arXiv:1209.5410](#) .
- [93] P. B. Gossiaux, J. Aichelin, T. Gousset, and V. Guiho, *J. Phys. G: Nucl. Part. Phys.* **37**, 094019 (2010), [arXiv:1001.4166](#) .
- [94] A. Adare *et al.*, preprint (2012), [arXiv:1208.2254](#) .
- [95] W. A. Horowitz, preprint (2011), [arXiv:1108.5876](#) .
- [96] J. Uphoff, O. Fochler, Z. Xu, and C. Greiner, *Phys. Lett. B* **717**, 430 (2012), [arXiv:1205.4945](#) .
- [97] J. Uphoff, O. Fochler, Z. Xu, and C. Greiner, preprint (2012), [arXiv:1212.0358](#) .
- [98] H. van Hees, M. Mannarelli, V. Greco, and R. Rapp, *Phys. Rev. Lett.* **100**, 192301 (2008), [arXiv:0709.2884](#) .
- [99] M. He, R. J. Fries, and R. Rapp, *Phys. Rev. C* **86**, 014903 (2012), [arXiv:1106.6006](#) .
- [100] M. Basile *et al.*, *Il Nuovo Cimento A* **65**, 421 (1981).
- [101] M. Luszczak, R. Maciula, and A. Szczurek, *Phys. Rev. D* **79**, 034009 (2009), [arXiv:0807.5044](#) .
- [102] R. Maciula and A. Szczurek, *Phys. Rev. D* **87**, 094022 (2013), [arXiv:1301.3033](#) .
- [103] H. Jung, M. Kraemer, A. V. Lipatov, and N. P. Zotov, *Phys. Rev. D* **85**, 034035 (2012), [arXiv:1111.1942](#) .
- [104] R. Vogt, *Interntl. J. Mod. Phys. E* **12**, 211 (2003), [hep-ph/0111271](#)

VITA

VITA

Mustafa Khalid Mustafa finished his Bachelors in Physics from the *University of Jordan*, Amman, Jordan in year 2008. Mustafa started his research work in the area of Mathematical Physics. He worked on a variety of mathematical problems in Solid State Physics and Atomic and Molecular Physics. After spending a year as a physics laboratory instructor at the *Middle East Technical University - North Cyprus Campus*, he joined *Purdue University* graduate school in year 2009. In year 2010, Mustafa joined STAR experiment at the *Relativistic Heavy-Ion Collider*, Brookhaven National Lab. Upton, NY. Mustafa worked on several projects in STAR experiment, including the analysis work presented in this dissertation.